Magnetic arch electrodeless plasma thruster experimental investigation

by

Célian Boyé

A dissertation submitted in partial fulfillment of the requirements for the degree of Doctor of Philosophy in

Aerospace Engineering

Universidad Carlos III de Madrid

Advisor(s):

Mario Merino
Jaume Navarro-Cavallé

Tutor:

Mario Merino

November 2025

À ma famille.

Illustration by Matteo Ripoli.

Je n'ai pas dit que c'était intelligent, mais c'est comme ça que ça s'est passé.

— Raphël Désirée

The proper function of man is to live, not to exist. I shall not waste my days in trying to prolong them. I shall use my time.

— Jack London

Acknowledgements

Je ne suis que la somme des rencontres et des expériences que j'ai pu faire durant toutes ces années. Je tiens donc à remercier toute personne que j'ai pu cotoyer à court ou à moyen terme, quelle que soit la nature de notre relation.

I would like to thank and express my gratitude to both of my supervisors, Mario and Jaume. These years have been more than intense from many regards, yet you have been supportive of my decisions through all the challenges I have faced. We had our fights, disagreements and troubles, but they are insignificant facing the accomplishment we have made through this project. Thank you Mario for remaining so calm in front of my stubborness during our long meetings and the opportunity you have given me to join such a project. Thank you Jaume for your time, your impressive patience and the long hours we spent in the laboratory and in your office. I would also like to thank Eduardo and Pablo for leading the EP2 research group.

Profondément, je tiens à remercier Stéphane Mazzoufre. Lors de la dernière année de l'IPSA, tous mes plans de carrière ont été bousculés par une simple introduction à la propulsion électrique. Tu as été à l'origine d'une passion qui m'a mené jusqu'à l'écriture de cette thèse. Alors merci pour toutes ces discussions, pour ton support infaillible et ton amitié. Merci aussi à Anica Lekic, pour ton soutien et tes mots justes au fil de toutes ces années.

Thanks to the original ZARATHUSTRA team. Diego, you have helped me even before reaching Madrid and I will never be able to thank you enough and pay you back for what you have done for me. Maddaloni, your tantrums in the office and your incontrolable laughs have lighted up every day of this thesis. Ripoli, I found in you a brother to my soul, thank you for all the moments I have shared with you, as well as the ones coming. Guys, thank you all for the joy you have brought to me, for making me laugh when I was at my lowest and for taking care of me so much. Tatiana, merci de ce que tu m'as apporté et de ce que tu m'as appris sur moi-même. I would also like to thank the EP2 group postdocs, PhD and master students for their support, their help and the good times spent all together.

Un immense merci à l'équipe du CRNS d'Orléans pour m'avoir accueilli durant les derniers mois de cette thèse. Etienne, Clémence, Alexis, Kevin, Fabiano, Alfredo, Vincent, vous avez rendu ces mois plus qu'exceptionnels. Merci aussi à Ulysse Weller et Laurent Garrigues pour m'avoir inclu dans l'organisation de l'IEPC 2024, que d'expériences magnifiques et de moments marquants.

Thank you Tommi, Vitto and Eu to allow my journey to continue in the elec-

tric propulsion field. Thank you Luca, Fabrizio, Bruno, Elia, Leonardo, Edoardo, Bhavya, Celina, Thomas and Pedro for making me feel so integrated and happy everyday. So much to say in such a short time, I hope to contribute always more to this amazing team.

Thank you Professor Wonho Choe for our never-ending talks in Orléans. Your wisdom, your words and your help to enlarge my vision and my horizons. I hope our paths cross many times again.

Merci à Raphaël, Antoine, Tania, Hugo, Rémy, Jonathan, Romain et Alexandre pour avoir été à mes côtés depuis le début de l'IPSA. Votre amitié sincère et votre soutien m'a permis de traverser toutes les épreuves. Merci particulièrement à Raphaël et Antoine pour avoir été mes frères durant toutes ces années, je ne serai pas l'ombre de la personne que je suis maintenant sans vous.

Merci aux Bret-Morel pour tous les bons moments passés, que ça soit à Oytier ou en Guadeloupe. Marie, merci de toujours trouvé du temps pour moi et de rendre ma vie plus jolie à chacune de nos rencontres. Merci à Mathilde pour m'avoir permis de passer de longs moments dans le calme d'un pré avec Urbania du Cresp et Pony, et m'avoir reconnecté avec le calme des chevaux. Merci à la Fédération Française d'Équitation pour tous les bons moments sur le parc équestre fédéral et l'accés priviligié au GOF. Grazie di tutto cuore alla famiglia Ripoli, presso la quale è stata scritta gran parte di questa tesi. Il vostro amore resterà per sempre nel mio cuore. Merci à toutes les personnes qui m'ont accompagné durant une partie de cette thèse, et plus particulièrement Roma pour toutes ces années passées à tes côtés. Merci aussi à Xavier, Emeric, Matthieu, Loïc, Yoann, Maxime, Romain et tous les autres pour toutes ces soirées passées avec vous, votre impact dans ce travail est considérable. Merci aux Bambanes pour m'avoir intégré d'une si belle manière dans votre groupe extrêmement soudé. Grazie Marzia, Mattia e Giovanni per la vostra gentilezza.

Je dédis cette thèse à ma famille. Vous m'avez tout donné et bien plus encore, et je vous dois tout. Votre soutien infaillible, vos mots, votre présence éternelle, vos rires infinis et votre amour m'ont guidé depuis ma naissance vers la personne que je suis. Vous m'avez vu autant heureux qu'au plus bas, autant pleurer de rire autour d'un repas à propos de sujets dont vous avez le secret qu'à la recherche calme de champignons dans des forêts couvertes de l'aube des montagnes des Pyrénées, et bien d'autres expériences qui ne seraient que trop longues à citer. Maman, je peine à trouver les mots pour te remercier de ton amour et de ta présence. Ces dernières années ont vu de nombreuses épreuves que tu m'as aidé à traverser, sans jugement et toujours avec compréhension. Papi, Mamie, vous m'avez inculqué toutes les valeurs que je suis fier de porter aujourd'hui. Vous m'avez élevé et rendu le plus heureux des petit-fils durant toutes ces années, et je vous dédis encore plus particulièrement ce travail. Pouvoir vous rendre fier est le plus bel honneur que je puisse espérer dans

cette vie. Phillipe, Séverine, Alexandre, Frank, Corrine, Maé, Evan, Théa, Héloïse, vous m'avez apporté tant de bonheur et de soutien que je me dois de vous remercier avec le plus grand amour. Je vous aime tous d'un amour inconsidéré.

Finalement, je tiens à remercier ma plus belle rencontre. Alexia, en moins de deux ans tu as bouleversé ma vie. Ton soutien dans l'écriture de cette thèse est incommensurable, au même titre que ta compréhension et ta patience. Tu as toujours su trouver les mots pour remonter un moral souvent trop bas et tu as été mon phare quand mon esprit se perdait trop loin. Notre famille a déjà commencé à se construire avec Kurie et Kraft, mais je sais au fond de moi que ce n'est que le début d'une aventure infinie qui nous ménera aux quatre coins du monde.

Published and submitted content

Journal papers:

- **Boyé C.**, Navarro-Cavallé J. and Merino M., "Ion current and energy in the magnetic arch of a cluster of two ECR plasma sources". Journal of Electric Propulsion. 2025, February 25; 4,10. Doi: 10.1007/s44205-025-00100-w. Wholly included in Chapter 4, the material from this source included in this thesis is not singled out with typographic means and references.

- **Boyé C.**, Navarro-Cavallé J., Merino M., A. Lecervoisier and S. Mazzoufre, "Ion velocity determination and populations sorting in a cluster of ECR sources". In preparation. Partially included in Chapter 5, the material from this source included in this thesis is not singled out with typographic means and references.

Conference papers:

- **Boyé C.**, Navarro-Cavallé J. and Merino M., "Preliminary analysis of the magnetic arch plasma expansion in a cluster of two ECR plasma thrusters". In 10th EUCASS—9th CEAS. July 2023, Lausanne, Switzerland. Partially included through Chapters 3 to 4, the material from this source included in this thesis is not singled out with typographic means and references.

- **Boyé C.**, Navarro-Cavallé J. and Merino M., Lecervoisier A., Mazouffre S., "Determining ion velocity in the interconnected plume of a cluster of two ECRTs using 2D LIF". In 38th International Electric Propulsion Conference (IEPC-2024). June 2024, Toulouse, France. Partially included in Chapter 5, the material from this source included in this thesis is not singled out with typographic means and references.

Datasets:

- **Boyé C.**, Navarro-Cavallé J. and Merino M., "Data from: Ion current and energy in the magnetic arch of a cluster of two ECR plasma sources". Zenodo. 2024, October 24. Doi: https://doi.org/10.5281/zenodo.13987138. Partially included in Chapter 4, the material from this source included in this thesis is not singled out with typographic means and references.

- **Boyé C.**, Mazouffre S., Navarro-Cavallé J. and Merino M., "Data from: 2D LIF of Ion Dynamics in a Magnetic Arch and Single-Source ECR Thrusters". Zenodo. 2025, September 23. Doi: https://doi.org/10.5281/zenodo.17186385. Partially included in Chapter 5, the material from this source included in this thesis is not singled out with typographic means and references.

Other research merits

- Merino M., Navarro-Cavallé J., **Boyé C.**, Jiménez P., Inchingolo M., Zhou J., Ahedo E., "Radiofrequency plasma heating for electrodeless space thruster applications". In IMPI's 56^{th} Annual Microwave Power Symposium. June 14-17, 2022, Savannah, USA.

- Merino M., García-Lahuerta D., **Boyé C.**, Ahedo E., "Preliminary model of the plasma expansion in a magnetic arch thruster (and overview of the first prototype)". In 37^{th} International Electric Propulsion Conference. June 19-23, 2022, Boston, USA.

- Merino M., Navarro-Cavallé J., Fajardo-Pena P., Inchingolo M., Jiménez P., Zhou J., García-Lahuerta D., **Boyé C.**, Maddaloni D., Terragni F., Ahedo E., "Electrodeless plasma thrusters and magnetized plasma expansions for space propulsion". In APS Annual Gaseous Electronics Meeting Abstracts 2022 (pp. EM2-007). October 3-7, 2022, Sendai, Japan.

- **Boyé C.**, Navarro-Cavallé J., Merino M., "First characterisation of a dual ECR thruster". In PLASMATECH 2023. April 26-28, 2023, Lisbon, Portugal.

- Merino M., Maddaloni D., **Boyé C.**, García-Lahuerta D., Ripoli M., Bayón B., Jiménez P., Terragni F., Navarro-Cavallé J., Fajardo-Pena P., Ahedo E., "ERC-ZARATHUSTRA: advances in electrodeless plasma thruster modeling, experiments, and data-driven analysis". In EPIC Workshop 2023. May 9-12, 2023, Naples, Italy.

- Jiménez P., Merino M., **Boyé C.**, García-Lahuerta D., Navarro-Cavallé J., Ahedo E., "Experiments and simulations of a magnetic arch plasma expansion for space propulsion". In 50^{th} IEEE International Conference on Plasma Science (ICOPS). May 21-25, 2023, Santa Fe, USA.

Abstract

The present thesis is dedicated to the experimental analysis and characterization of novel Electrodeless Plasma Thrusters (EPTs) operating under Electron Cyclotron Resonance (ECR), with a particular focus on the Magnetic Arch (MA) topologies. The primary objective of this work has been to investigate and better understand the plasma dynamics, plume expansion, and ion acceleration mechanisms inherent to clustered ECR thrusters and MA devices. To achieve this goal, the work has been articulated around the design, development, and commissioning of three prototypes, supported by plasma diagnostics, notably Langmuir Probes (LPs), Retarding Potential Analyser (RPA), Faraday Cups (FCs), and 2D Laser-Induced Fluorescence (LIF) spectroscopy.

Electric Propulsion (EP) systems have become an essential technology for modern in-space propulsion, offering high exhaust velocities and propellant efficiency compared to conventional chemical propulsion. Within the realm of EP, EPTs eliminate the need for grids or electrodes in direct contact with the plasma, thus mitigating lifetime-limiting erosion phenomena. Among EPTs, Electron Cyclotron Resonance Thrusters (ECRTs) constitute a subclass in which plasma production and heating are achieved through the resonant interaction between injected microwaves and electrons gyrating around magnetic field lines at the ECR condition. This mechanism allows efficient electron heating, leading to ionization of neutral gas. The ECR heating mechanism relies on tuning the microwave frequency and magnetic field to match the ECR frequency, enabling energy transfer to the electrons and thus sustaining ionization. Once generated, the plasma is guided, confined, and partially accelerated through divergent magnetic topologies such as magnetic nozzles or MAs. The electrodeless nature of ECRTs brings multiple advantages, including the absence of neutralizers, the potential for extended lifetime, reduced erosion, and increased flexibility in propellant choice. Nevertheless, these devices face challenges such as lower thrust efficiencies, high plume divergence, and complex plasma transport mechanisms still not fully understood. The use of MA-like topologies also aims to counter the ions loss to the sources rear-plate, to lower the torque between the geomagnetic and the thrust magnetic field by using a near-zero net dipole and to enable thrust vectoring.

A first set of experiments was conducted using a dual-source cluster configuration of two independent ECR sources, as shown in Chapter 4. Using retarding potential analysers and Faraday cups, the ion flux, most probable ion energies, and plume divergence were mapped for single and dual-source operation modes. The

effect of magnetic configuration, microwave power, and mass flow rate on ion energy distribution functions was analysed, providing valuable insight into the merging dynamics of clustered plumes and the MA's role in guiding ions. It was observed that the dual-source configuration introduced broader plume divergences, complex azimuthal asymmetries, and non-trivial energy distributions dependent on cluster topology.

The Electron Cyclotron Resonance Cluster 2 (ECRC2) setup was designed to overcome some of the limitations observed in the ECRC1. This second prototype is presented through Chapter 5. The ECRC2 improved gas injection systems and reduced the thermal stress on electromagnetic coils by using permanent magnets. Two extensive experimental campaigns followed, employing both electrostatic probes to characterize the plasma density, electron temperature, plasma potential, floating potential and 2D LIF spectroscopy to characterize the in-plane ion velocity vector fields in the plume. The 2D LIF measurements allowed differentiation between two ion populations and revealed the non-trivial ion flow structures. Comparisons between single-source and cluster operations indicated that clustering modifies ion trajectories and energy distributions, confirming the significant impact of magnetic field topology on plasma expansion mechanisms.

Finally, Chapter 6 presents the Magnetic Arch Thruster (MAT), which was developed to evaluate a more compact C-shaped MA configuration. Despite encountering technical limitations during the initial tests, these experiments provided important feedback on power coupling stability, thermal management, and transmission line durability. These results complement the plasma physics investigations by addressing practical engineering aspects necessary for future prototypes development.

The thesis concludes that MA-based ECR thrusters offer promising pathways for advanced electrodeless plasma propulsion, with clustering strategies introducing both opportunities and additional complexities. The experimental evidence supports the crucial role of magnetic topology in shaping plasma expansion and ion acceleration. The interplay between magnetic field configuration, microwave coupling, and gas injection critically determines thruster plume divergence and operational stability. Furthermore, the use of non-invasive diagnostics such as LIF has proven essential to unravel the complex ion velocity distribution functions and two-population behaviours arising in clustered ECR systems.

In summary, this thesis provides an experimental foundation for understanding the plasma behaviour in clustered ECR-based electrodeless thrusters operating under MA topologies. The results contribute both to fundamental plasma physics knowledge and to the applied development of future scalable and efficient electric propulsion systems for in-space applications.

Resumen

La presente tesis está dedicada al análisis experimental y a la caracterización de Electrodeless Plasma Thrusters (EPTs) que operan mediante Electron Cyclotron Resonance (ECR), con un enfoque particular en topologías de Magnetic Arch (MA). El objetivo principal de este trabajo ha sido investigar y comprender en mayor profundidad la dinámica del plasma, la expansión de la pluma y los mecanismos de aceleración iónica inherentes a configuraciones agrupadas de propulsores ECR y dispositivos MA. Para alcanzar este propósito, el trabajo se ha articulado en torno al diseño, desarrollo y puesta en marcha de tres prototipos, apoyados por un conjunto de diagnósticos de plasma, entre los que destacan las Langmuir Probes (LPs), el Retarding Potential Analyser (RPA), las Faraday Cups (FCs) y la espectroscopía de Laser Induced Fluorescence (2D LIF).

Los sistemas de propulsión eléctrica (Electric Propulsion, EP) se han consolidado como una tecnología esencial para la propulsión espacial moderna, al ofrecer altas velocidades de escape y una mayor eficiencia en el consumo de propelente en comparación con la propulsión química convencional. Dentro del campo de la EP, los EPTs eliminan la necesidad de rejillas o electrodos en contacto directo con el plasma, mitigando así los fenómenos de erosión que limitan la vida útil de los dispositivos tradicionales. Entre los EPTs, Electron Cyclotron Resonance Thrusters (ECRTs) constituyen una subclase donde la producción y el calentamiento del plasma se logran mediante la interacción resonante entre microondas inyectadas y electrones que giran alrededor de las líneas de campo magnético bajo la condición ECR. Este mecanismo permite un calentamiento eficiente de los electrones, facilitando la ionización del gas neutro y la posterior aceleración del plasma. La técnica de calentamiento ECR depende de ajustar la frecuencia de las microondas para que coincida con la frecuencia de resonancia ciclotrónica de los electrones, posibilitando así la transferencia de energía y el sostenimiento de la ionización. Una vez generado, el plasma es guiado, confinado y parcialmente acelerado mediante topologías magnéticas divergentes, tales como toberas magnéticas o arcos magnéticos.

La naturaleza sin electrodos de los ECRTs ofrece múltiples ventajas, entre las que se incluyen la ausencia de neutralizadores, la posibilidad de una vida operativa prolongada, la reducción de la erosión y una mayor flexibilidad en la elección del propelente. No obstante, estos dispositivos aún enfrentan desafíos significativos, como bajas eficiencias de empuje relativamente, alta divergencia de la pluma y complejos mecanismos de transporte del plasma haun no han sido comprendidos completamente. Además, el uso de topologías tipo MA busca contrarrestar la pérdida de

iones hacia la placa posterior de las fuentes, reducir el par de fuerzas generado entre el campo geomagnético y el campo magnético del propulsor al operar con un dipolo neto nulo, y permitir el control vectorial del empuje.

El primer conjunto de experimentos se realizó utilizando una configuración de doble fuente (cluster) compuesta por dos fuentes ECR independientes, como se detalla en el Capítulo 4. Mediante el uso de analizadores de potencial retardado y FCs, se midió el flujo iónico, las energías iónicas más probables y la divergencia de la pluma tanto en modos de operación de una sola fuente como en configuración de doble fuente. Se analizó el efecto de la configuración magnética, la potencia de microondas y el caudal de masa sobre las funciones de distribución de energía iónica, proporcionando valiosa información sobre la dinámica de acoplamiento de plumas agrupadas y el papel del MA en la guía de los iones. Se observó que la configuración de doble fuente introdujo mayores divergencias de la pluma, asimetrías azimutales complejas y distribuciones energéticas no triviales dependientes de la topología del cluster.

El segundo prototipo, denominado Electron Cyclotron Resonance Cluster 2, (ECRC2), fue diseñado para superar algunas de las limitaciones observadas en el primer sistema (ECRC1). Esta configuración se presenta en el Capítulo 5. El ECRC2 incorporó mejoras en los sistemas de inyección de gas y redujo el estrés térmico sobre las bobinas electromagnéticas mediante el uso de imanes permanentes. Se llevaron a cabo dos extensas campañas experimentales, empleando tanto sondas electrostáticas para caracterizar la densidad de plasma, la temperatura electrónica y el potencial de plasma, como espectroscopía LIF bidimensional para obtener los campos vectoriales de velocidad iónica en el plano de la pluma. Las medidas de LIF 2D permitieron diferenciar dos poblaciones iónicas y revelaron estructuras complejas en el flujo de iones. Las comparaciones entre los modos de operación de fuente única y cluster indicaron que el agrupamiento modifica significativamente las trayectorias iónicas y las distribuciones energéticas, confirmando el impacto decisivo de la topología del campo magnético sobre los mecanismos de expansión del plasma.

Finalmente, el Capítulo 6 presenta el desarrollo del Magnetic Arch Thruster (MAT), concebido para evaluar una configuración más compacta de arco magnético en forma de "C". Aunque se encontraron limitaciones técnicas durante los ensayos iniciales, estos experimentos aportaron información relevante sobre la estabilidad del acoplamiento de potencia, la gestión térmica y la durabilidad de las líneas de transmisión. Estos resultados complementan los estudios físicos del plasma al abordar aspectos ingenieriles fundamentales para el desarrollo de futuros prototipos.

La tesis concluye que los propulsores ECR basados en arcos magnéticos ofrecen una vía prometedora para la propulsión eléctrica sin electrodos, con estrategias de agrupamiento que introducen tanto oportunidades como complejidades adicionales. La evidencia experimental respalda el papel fundamental de la topología magnética

en la expansión del plasma y la aceleración iónica. La interacción entre la configuración del campo magnético, el acoplamiento de microondas y la inyección de gas determina críticamente la divergencia de la pluma del propulsor y su estabilidad operacional. Además, el uso de diagnósticos no invasivos como la LIF ha demostrado ser esencial para desentrañar las funciones complejas de distribución de velocidades iónicas y los comportamientos de doble población que emergen en sistemas ECR agrupados.

En resumen, esta tesis aporta una base experimental para la comprensión del comportamiento del plasma en propulsores sin electrodos basados en ECR que operan bajo topologías de arco magnético. Los resultados contribuyen tanto al conocimiento fundamental de la física del plasma como al desarrollo aplicado de futuros sistemas de propulsión eléctrica escalables y eficientes para aplicaciones espaciales.

Résumé

La présente thèse est consacrée à l'analyse expérimentale et à la caractérisation de nouveaux propulseurs plasma sans électrodes (EPTs) fonctionnant selon le principe de la résonance cyclotronique des électrons (ECR), avec un accent particulier sur les topologies d'arche magnétique. L'objectif principal de la thèse est d'étudier et de d'obtenir une meilleure compréhension la dynamique du plasma, l'expansion du faisceau plasma et les mécanismes d'accélération des ions propres aux propulseurs ECR en cluster et aux dispositifs utilisant une arche magnétique. Pour atteindre cet objectif, le travail s'est articulé autour de la conception, du développement et du test de trois prototypes, soutenus par un ensemble de diagnostics plasma, notamment des sondes de Langmuir (LP), un analyseur de potentiel retardé (RPA), des coupes de Faraday (FC), ainsi qu'une spectroscopie de fluorescence induite par laser bidimensionnelle (2D LIF).

Les systèmes de propulsion électrique (EP) se sont imposés comme une technologie clé pour la propulsion spatiale moderne, en offrant des vitesses d'éjection élevées et une meilleure efficacité de consommation de propergol par rapport à la propulsion chimique conventionnelle. Dans le domaine de la PE, les EPTs permettent d'éliminer l'usage de grilles ou d'électrodes en contact direct avec le plasma, réduisant ainsi les phénomènes d'érosion qui limitent la durée de vie des systèmes classiques. Parmi les EPTs, les propulseurs à résonance cyclotronique des électrons (Electron Cyclotron Resonance Thrusters, ECRTs) forment une sous-catégorie dans laquelle la production et le chauffage du plasma sont réalisés par l'interaction résonante entre les micro-ondes injectées et les électrons en rotation autour des lignes de champ magnétique selon la condition de résonance ECR. Ce mécanisme permet un chauffage efficace des électrons, conduisant à l'ionisation du gaz neutre et à l'accélération subséquente du plasma.

Le chauffage ECR repose sur l'ajustement de la fréquence des micro-ondes pour qu'elle coïncide avec la fréquence cyclotronique des électrons, assurant ainsi un transfert d'énergie optimal et le maintien de l'ionisation. Une fois formé, le plasma est guidé, confiné et partiellement accéléré par des topologies magnétiques divergentes, telles que les tuyères magnétiques ou les arches magnétiques.

L'absence d'électrodes immergées confère aux ECRTs de multiples avantages : suppression des besoins en neutraliseurs, prolongation de la durée de vie, réduction de l'érosion et flexibilité accrue dans le choix du propergol. Néanmoins, ces dispositifs rencontrent encore certaines limitations telles qu'une efficacité de poussée relativement faible, une divergence importante et des mécanismes de transport plasma

complexes, qui demeurent partiellement incompris. Par ailleurs, l'utilisation de topologies de type arche magnétique vise également à limiter la perte d'ions vers la plaque arrière des sources, à réduire le couple généré entre le champ magnétique géomagnétique et celui du propulseur grâce à un dipôle net quasi nul, et à permettre le contrôle vectoriel de la poussée.

Une première série d'expériences a été réalisée à l'aide d'une configuration bi-source (cluster) constituée de deux sources ECR indépendantes et nommée ECRC1, comme décrit au Chapitre 4. à l'aide du RPA, le flux ionique, les énergies ioniques les plus probables ainsi que la divergence ont été cartographiés pour les modes de fonctionnement mono-source et bi-source. L'impact de la configuration magnétique, de la puissance micro-onde et du débit massique sur les fonctions de distribution d'énergie ionique a été étudié, offrant un éclairage précieux sur la dynamique de fusion des plumes groupées et sur le rôle de l'arche magnétique dans le guidage ionique. Il a été observé que la configuration bi-source induit une divergence de plume plus importante, des asymétries azimutales complexes et des distributions énergétiques non triviales, dépendant de la topologie du cluster.

Le second prototype, dénommé Electron Cyclotron Resonance Cluster 2 (ECRC2), a été conçu afin de surmonter certaines des limitations identifiées sur le premier système (ECRC1). Cette configuration est présentée au Chapitre 5. Le ECRC2 a introduit des améliorations sur le système d'injection de gaz et a réduit le stress thermique sur les bobines électromagnétiques grâce à l'emploi d'aimants permanents. Deux campagnes expérimentales approfondies ont été menées, combinant des sondes électrostatiques — pour caractériser la densité de plasma, la température électronique et le potentiel plasma et le potentiel flottant — et la spectroscopie LIF 2D pour cartographier les champs vectoriels de vitesses ioniques dans la plume. Les mesures LIF 2D ont permis de distinguer deux populations ioniques et de mettre en évidence des structures complexes dans leur flux. Les comparaisons entre les configurations mono-source et cluster ont montré que le clustering modifie sensiblement les trajectoires et les distributions énergétiques des ions, confirmant l'impact déterminant de la topologie magnétique sur les mécanismes d'expansion plasma.

Enfin, le Chapitre 6 présente le développement du Magnetic Arch Thruster (MAT), conçu pour évaluer une configuration d'arche magnétique en « C » plus compacte. Malgré certaines limitations techniques rencontrées lors des essais initiaux, ces expériences ont fourni des retours importants concernant la stabilité du couplage de puissance, la gestion thermique et la durabilité des lignes de transmission. Ces résultats viennent compléter les investigations plasma en abordant des aspects d'ingénierie cruciaux pour le développement de prototypes ultérieurs.

La thèse conclut que les ECRTs à base d'arche magnétique constituent une voie prometteuse pour la PE sans électrodes, les stratégies de regroupement ouvrant à la fois des perspectives et des défis supplémentaires. Les résultats expérimentaux

confirment le rôle central de la topologie magnétique dans l'expansion du plasma et l'accélération ionique. L'interaction entre la configuration du champ magnétique, le couplage micro-onde et l'injection de gaz détermine de manière critique la divergence de la plume et la stabilité opérationnelle du propulseur. Par ailleurs, l'emploi de diagnostics non-invasifs tels que la LIF s'est avéré essentiel pour démêler les fonctions complexes de distribution de vitesses ioniques et les comportements à deux populations qui apparaissent dans les systèmes ECR groupés.

En résumé, cette thèse fournit une base expérimentale pour la compréhension du comportement plasma dans les EPTs basés sur l'ECR opérant sous des topologies d'arche magnétique. Les résultats apportent à la fois une contribution à la physique fondamentale du plasma et au développement appliqué de futurs systèmes de PE évolutifs et efficaces pour les applications spatiales.

Contents

List of Figures

List of Tables

Acronyms

AR Aspect Ratio

BS Beam Splitter

C2W Coaxial-to-Waveguide adapter

CC Continuous Coil

CEX Charge Exchange Collision

CT Coaxial Termination

ECR Electron Cyclotron Resonance

ECRC1 Electron Cyclotron Resonance Cluster 1

ECRC2 Electron Cyclotron Resonance Cluster 2

ECRT Electron Cyclotron Resonance Thruster

EEDF Electron Energy Distribution Function

EP Electric Propulsion

EPT Electrodeless Plasma Thruster

FC Faraday Cup

GIE Gridded Ion Engine

HET Hall Effect Thruster

HPH High Power Helicon

HPT Helicon Plasma Thruster

HSE High SEnsitivity probe

HWHM Half Width at Half Maximum

IC Ionisation Chamber

IEDF Ion Energy Distribution Function

IL Insertion Loss

IVDF Ion Velocity Distribution Function

LIF Laser Induced Fluorescence

LP Langmuir Probe

MA Magnetic Arch

MAT Magnetic Arch Thruster

MF Magnetic Field

MFL Magnetic Field Line

MN Magnetic Nozzle

MP Main Population

MW Micro Wave

MWG Micro Wave Generator

OF Optical Fiber

PC Principal Coil

PIC Particle-In-Cell

RA Right Angle connector

RPA Retarding Potential Analyser

SP Secondary Population

TL Transmission Line

VNA Virtual Network Analyser

Nomenclature

α	Angle of measurement, deg
β_n	Complex propagation constant, m$^-$1
χ	Dimensionless Hall parameter
$\Delta\nu$	Doppler shift, Hz
$\dot{m}$	Mass flow rate, sccm
$\dot{m}_{Xe,total}$	Total Xenon mass flow rate, sccm
γ	Polytropic coefficient
$\hat{\Omega}_{i0}$	Dimensionless magnetisation parameter
λ	Wavelength, m
λ_D	Debye length, m
$\mathbf{F}$	External forces, N
$\mathbf{k}$	Laser beam wave vector, rad.m^{-1}
$\mathbf{v}$	Velocity vector, km.s^{-1}
ν	Laser frequency, Hz
ν_0	Studied transition unshifted frequency, Hz
ω_{ce}	Electron cyclotron resonant angular frequency, rad.s^{-1}
ϕ	Plasma potential, V
ρ	Electrical resistivity, Ω.m
σ	Standard deviation
θ_n	Electrical length
$\tilde{u}_i$	Ion in-plane velocity, km.s^{-1}
A	Normalised Gaussian amplitude
A_{CS}	Coil cross-sectional area, m^2
B	Magnetic field magnitude, G
B_{ECR}	ECR magnetic field, 875 G
c	Speed of light in a vacuum, 299792458 m.s^{-1}
e	Single electron charge, $1.6e-19$ C
E_i	Ion most probable energy, eV

f	Frequency, Hz
F_m	Magnetic thrust, N
F_p	Pressure thrust, N
g_0	Standard gravitational acceleration, $9.80665\,\mathrm{m.s^{-2}}$
I	Current, A
I_e	Electron current, A
I_{sp}	Specific impulse, s
j	Ion current density, $\mathrm{A.m^{-2}}$
l	Length of the coil copper wire, m
m_0	Initial mass, kg
m_e	Electron mass, $0.911e-30\,\mathrm{kg}$
m_f	Final mass, kg
m_i	Ion mass, for Xenon mass is $131 \times 1.67e-27\,\mathrm{kg}$
m_p	Propellant mass, kg
m_{dry}	Empty rocket mass, kg
n_e	Electron density, $\mathrm{m^{-3}}$
n_i	Ion density, $\mathrm{m^{-3}}$
$P_{MW,total}$	Total microwave power, W
P_{MW}	Microwave power, W
R	Electrical resistance, Ω
S	Scattering matrix
T	Temperature, K
T_e	Electron temperature, eV
T_i	Ion temperature, eV
u_{xi}	Ion velocity in the x-direction, $\mathrm{km.s^{-1}}$
u_{zi}	Ion velocity in the z-direction, $\mathrm{km.s^{-1}}$
V	Voltage, V
V^+	Incident voltage wave, V
V^-	Reflected voltage wave, V
v_0	Initial velocity, $\mathrm{km.s^{-1}}$
v_e	Exhaust velocity, $\mathrm{km.s^{-1}}$
V_f	Floating potential, V
v_k	Velocity parallel to $\mathbf{k}$, $\mathrm{km.s^{-1}}$
v_p	Phase velocity, $\mathrm{km.s^{-1}}$

Chapter 1

Introduction

1.1 In-space propulsion

Egyptians imagined spiritual journeys and afterlives connected to celestial realms from the 27th century BCE. Since this representation of air and space, a never-ending trip has taken place, from the first successful powered flight of the Wright brothers in 1903 to the launch of the first artificial satellite, Sputnik 1, in 1957—not forgetting the launch of the first French satellite, Astérix, in 1965. Hardly half a century was necessary to transcend from the skies to the stars, to evolve from airplanes to rockets, from rockets to space shuttles and the continuous human presence in space, and from this continuous presence to interplanetary exploration. Mankind has progressed in spirit and technology to deepen the understanding of our Universe, in a never-ending story.

This tremendous progress has led to the complete colonization of Earth's orbits. The ever-growing space industry—filled with international agencies, major companies, and startups—has fulfilled the needs of our modern society by launching over 10,000 satellites. Private companies are developing their own rockets, adding 6,000 satellites since 2019. The improvements realized in the space propulsion field significantly ameliorated their flexibility, weight, and lifetime. EP (Electric Propulsion), which has been used since NASA's SERT-1 mission in 1964 (five years prior to the first step of the Moon), represents the most significant step in the field of space propulsion. The more efficient use of propellant allowed higher payload masses and an extension of the operational lifetime of spacecraft while allowing long-term manoeuvring and fitting the new space regulations on deorbiting. There is a constant need to improve EP, and this thesis represents only a gravel of an infinite road paved by thousands of minds, constantly elevating towards the stars.

1.2 Ideal rocket equation

EP is usually viewed as a competitor to chemical propulsion. However, they should be seen as complementary. Indeed, they offer different approaches to the same problem. The acceleration of chemical propulsion results in the conversion of energy

from chemical to kinetic. However, EP uses externally stored energy to accelerate the propellant. EP provides greater exhaust velocity for a given manoeuvre with lower propellant consumption. However, EP provides low thrust levels, which limits its use to in-space propulsion only.

Without a medium to carry on propulsion, an object must rely on the acceleration of a stored propellant to generate thrust. A rocket with a propellant mass m_p and velocity $\mathbf{v}$, facing external forces $\mathbf{F}$, is considered. As the propellant mass constantly decreases, this equation can be written as a function of the propellant mass flow rate $\dot{m}_p$. Hence, the effective exhaust velocity of the propellant relative to the rocket $\mathbf{v}_e$ is considered. Conservation of momentum dictates the following equation:

$$\mathbf{F} = m\frac{d\mathbf{v}}{dt} = \dot{m}\mathbf{v}_e = \dot{m}I_{sp}g_0 \tag{1.1}$$

The propellant exhaust velocity can be expressed in terms of specific impulse I_{sp} as the effective exhaust velocity normalized with the gravity constant g_0. Considering an ideal situation by neglecting external forces (such as frictional forces or gravity), Equation 1.1 can be integrated in time to determine the variation in the rocket speed to perform a manoeuvrer in space—between an initial velocity $\mathbf{v}_0$ and mass m_0 to a final velocity $\mathbf{v}_f$ and mass m_f:

$$\Delta\mathbf{v} = \mathbf{v}_f - \mathbf{v}_0 = I_{sp}\, g_0 \ln\left(\frac{m_0}{m_f}\right) = \mathbf{v}_e \ln\left(1 + \frac{m_p}{m_f}\right) \tag{1.2}$$

m_p refers to the mass of propellant consumed during the manoeuvrer, where m_{dry} depicts the rocket mass without propellant: $m_0 = m_p + m_{dry}$. The exhaust velocity is considered constant through the manoeuvrer. Equation 1.2 is referenced as the Tsiolkovsky equation[1]. A significant gain in velocity can be reached by matching the propellant mass to the dry mass or by reaching high exhaust velocity—i.e. high I_{sp}. The first option directly implies a reduction of the rocket dry mass and, therefore, a limited payload mass. Moreover, increasing the exhaust velocity allows to reduce the amount of propellant consumed for a given change in velocity. This trade-off can be better understood by expressing the propellant mass as a function of the change in velocity and the exhaust velocity using Equation 1.2:

$$m_p = m_0\left[1 - \exp\left(\frac{-\Delta v}{v_e}\right)\right] \tag{1.3}$$

Considering a defined $\Delta\mathbf{v}$ for a given mission, the exhaust velocity would need to be greater than the gain in velocity to reduce the propellant consumption of the manoeuvrer. A great exhaust velocity implies the possibility of carrying a larger payload and reduces the propellant consumption and cost through more extended missions. The chemical propulsion reaches its limits through this problem, with a limited exhaust velocity (i.e. $\mathbf{v}_e < 5500\,\mathrm{m/s}$[1]) and specific impulse (i.e. $I_{sp} <$

500 s[2]). On the other hand, EP allows for higher exhaust velocities, as the energy source is separated from the propellant. EP uses solar energy collected by the spacecraft's solar arrays to ionise and accelerate propellants. Due to the limitations in terms of size and efficiency of solar arrays and the meagre mass flow rates, the thrust lies in the order of mN to N for high-power electric propulsive systems.

1.3 Electric propulsion overview

EP can be summarized to the use of external electric energy to achieve high exhaust propellant speed. Depending on the way the electric energy is used to produce and accelerate the plasma, three main categories can be defined[3].

- **Electrothermal propulsion** (*resistojets*, *arcjets*): electric power heats the propellant inside a chamber, increasing its pressure. The thermal energy of the hot neutral propellant or the plasma is converted to kinetic energy due to the expansion through a nozzle.
- **Electrostatic propulsion** (*gridded ion thrusters*): plasma is accelerated and expelled using electric fields.
- **Electromagnetic propulsion** (*Hall effect thrusters*, *MPD thrusters*, *pulsed inductive thrusters*): both the ionization and the acceleration are enabled by a combination of electric and magnetic forces.

1.3.1 Hall effect thrusters and gridded ion engines

The HETs (Hall Effect Thrusters) and GIEs (Gridded Ion Engines) represent the most used technology in use for in-space EP[4]–[6]. In particular, the HETs operate by establishing axial electric and radial MF (Magnetic Field) setup in a ring-shaped discharge chamber, where an anode sits at one end. At the same time, a hollow cathode is positioned externally. The MF hinders the motion of the electrons generated by the cathode toward the anode within an axial electric field, efficiently ionizing the propellant gas introduced into the chamber[7]–[9]. The ions created this way are then accelerated by the electric field, producing the necessary thrust. Most of the electron current (around 80%[10]) emitted by the cathode travels downstream to balance the ion beam, while the rest flows toward the anode, keeping the plasma active. The MF is designed to contain electron movement without affecting the paths of ions, concentrating the electric potential drop near the chamber's exit to enhance thrust efficiency. With efficiencies from 40% to 60% and specific impulses near 1500 seconds[6], [11], HETs can scale up to high-power outputs, making them adaptable to applications requiring tens of kilowatts.

Gridded ion engines (GIEs)[10] achieve controlled thrust by splitting the ionization and acceleration processes, allowing for precise adjustments to speed and thrust levels. In these engines, gas is injected into a chamber where electrons from a cathode collide with the gas molecules, creating ions. To enhance this process, either MFs or high-frequency waves are often used, which improves ion production and reduces wear on the chamber. Once ionized, the ions move through a grid system, usually with two or three grids. The first grid focuses the ions and blocks any unwanted particles, while the second grid provides the acceleration needed to propel them out of the engine. An optional third grid can be used to decrease ion energy and reduce long-term wear on the engine. After passing through the grids, electrons from an external source neutralize the ion beam, resulting in a steady, balanced exhaust flow that generates thrust. GIEs are known for their efficiency and fine control, making them especially valuable for long-duration space missions where steady propulsion is critical.

These thrusters present many limitations and inherent problems that limit their use and performance[10]. To begin with, the use of electrodes induces a strong constraint on the power scaling. HETs present conflicting scaling laws for the geometry, power, MF and mass flow rates when the GIEs require larger frontal area to increase their thrust. Moreover, they both present narrow operating ranges that reduce their flexibility. As the electrodes are exposed to the plasma, they endure constant high-energy particle bombardment that causes erosion and are unfit for the use of alternative reactive propellants. Finally, both require the use of a complex neutralizer acting as a critical subsystem and the use of very pure Xenon to avoid the contamination of the electron emitting inserts.

1.3.2 Electrodeless plasma thrusters

EPTs (Electrodeless Plasma Thrusters) are being investigated in order to address the need of challenging limitations of classic HETs and GIEs. EPTs devices group various technologies. However HPTs (Helicon Plasma Thrusters) and ECRTs (Electron Cyclotron Resonance Thrusters) remain the main elements of this section of EP. They differentiate upon the frequency of the electromagnetic wave in use to perform ionisation: from the *MHz* range for the HPTs to the *GHz* range for the ECRTs. In particular for ECRTs, electrons are heated when the MW (Micro Wave) time varying electric field matches its frequency with the gyration of the electrons at the cyclotron resonant frequency given by: $\omega_{ce} = eB/m_e$. Part of the MW power is lost through recombination and excitation losses. Once plasma is generated by collisions in between the electrons and the neutral atoms, both types usually go through a MN (Magnetic Nozzle). It confines, accelerates and carries out the plasma, generating thrust using kinetic energy from the remaining part of the coupled MW power.

Their current-free plume allows the absence of lifetime limiting grids or neutralis-

ers, in addition to the possible use of alternative propellants in place of expensive high-purity Xenon. Not only EPTs bring more flexibility and simplicity, they open a whole new range of geometries to be explored as a mean to improve space propulsion. The absence of electrodes immersed directly in contact with the plasma for both ionisation or acceleration reduces the inconvenient erosion issues seen in classic propulsion systems. The MN itself also reduces the erosion seen by the thruster—in particular its IC (Ionisation Chamber)—by magnetically shielding the walls when confining the plasma. Besides, the plasma confinement also reduces the particle losses at the walls, hence improving EPTs performances. As cited before, EPTs plasma plume are current-free, offering an advantage not only in terms of flexibility and simplicity, but also in the choice of propellant and the high lifetime of the system. Regardless of the previously mentioned advantages, EPTs still carry cons facing the classic propulsion systems. Indeed, their thrust efficiency and I_{sp} remain lower than the ones of HETs or GIEs. Even though the MN confines and guides the plasma, EPTs plume also remains more divergent. EPTs are still under active research and several aspects of their physics are not well understood, in particular upon the plasma heating and transport. Moreover, inherent limitations and flaws in current cylindrical thruster designs need to be addressed in order to progress within the EPTs development. The latter constitutes a strong motivation in this thesis.

1.4 ECR state of the art

1.4.1 Historical background

ECRTs have been studied and developed since the '60s by three main entities: General Electric Company, funded by the Lewis Research Centre, the NASA group from the Lewis Research Centre, and the University of Tokyo. These entities have paved the way for the development of ECRTs, improving their thrust and efficiency while reducing their size and mass.

In the framework of the Cyclops program, the General Electric Company performed numerous experiments on several ECRTs, varying their gas injection arrangements, waveguide designs, MW frequencies, and IC materials. The power range even increased to several kW. In 1964, Miller et al.[12] presented both simulation and experimental results upon a 2.45 GHz—320 W ECRT operating with Argon. Up to 80-90% of the incident MW power was deposited in the plasma. This efficiency could have placed this first prototype in the efficiency range of contemporary HETs or GIEs. A corrected thrust efficiency in the $10-20\%$ range has been determined and presented by Crimi et al.[13]. However, many conclusions have been drawn from this first ECRT prototype. A slightly divergent beam has been observed and it has been observed that particle trajectories can cross the flux line. Moreover,

the ion trajectory is independent of the dipole moment and its mass. Interestingly, it has been determined that the electron trajectories are converted from transverse to longitudinal. However, as Crimi et al.[13] have brought to light, electrons lose their thermal energy in the IC prior to plasma expansion and acceleration. This phenomenon prevents optimal acceleration performances in ECRTs. Even though it has first been linked to line radiation caused by inelastic collisions between electrons and atoms, this phenomenon occurs due to the plasma diffusion to the walls across the MFLs (Magnetic Field Lines).

In addition, the experiments performed by Kosmahl in 1967 through the NASA / General Eletric framework [14] underlined the importance of wave polarization, as well as the background pressure effects. This work presents both the estimation of the thruster's performances and the experimental data. The thruster consists of a circular waveguide consistent with a frequency of 8.35 GHz, associated with an average power of 1 kW. Radial gas injection is performed with a mass flow rate of 1 mg/s, with both Xenon and Argon. Both FCs (Faraday Cups) and LPs (Langmuir Probes) have been used; however, it appears that the expected performances could not be reached. The conclusions lean towards high background pressure (5×10^{-5} torr), as a colisionless plasma had been considered in the performances estimations. Moreover, it appears that the forward wave polarization was not as circular as intended.

Caltech scientists —such as Sercel, Kaufman and Goodwin—performed multiple studies on ECRTs during the '80s. Following Kosmahl's work, their first prototype consists of an Argon-fed ECRT with an inner diameter of 12.8 cm. They vary the mass flow rate from 1 to 10 sccm, with an incident MW of 2.12 GHz[15]. Electron temperature measurements were performed with a LP when an emissive probe probed the plasma potential. They highlighted the repercussions of vacuum chamber pressure on electron temperature and plasma potential. Indeed, a sevenfold decrease can be observed in the plasma potential fall by increasing the pressure by an order of magnitude. Moreover, increasing the chamber pressure raises the background neutral density, resulting in a decrease in electron temperature. Sercel[16] deepened the development of ECRTs at Caltech during his Ph.D. thesis. His work is characterized by comparing simulations performed by a 1D model and experimental data. Plasma characteristics have been measured by LPs (electron temperature and density, ion density, floating and plasma potential), RPAs (Retarding Potential Analysers) (IEDF (Ion Energy Distribution Function)) and diamagnetic loops (plasma magnetization). The experimental efficiencies proved to be lower than the ones obtained through simulation—except for the utilisation efficiency being estimated and measured at 90%. The divergence efficiency lies around 50% when estimated at 95%, and the thrust efficiency drops to 2% in front of the 40% estimation. It should be noted that the reflected power has not been measured and was only assumed to equal 70%. Considering a better coupling of the forwarded wave with the plasma, it is possible to consider higher efficiencies. Kaufman and Goodwin

continued to investigate the ECRT, in particular, on the effect of the background pressure on the performances and the plasma characteristics. As demonstrated in previous and future works, the energy efficiency—linked to the ion energy, thus to the electron temperature—strongly decreases when the pressure increases. These conclusions stopped the development and research associated with the ECRT in Caltech.

Studies conducted at the University of Tokyo and presented by Nagatomo et al.[17] focused on understanding the acceleration mechanism occurring in ECRT. The probing of the MW field strength in the IC, of the electrostatic potential in the plume through LPs and of thrust were performed on an Argon-fed 2.45 GHz—400 W ECRT. The mass flow rate varies from 0.05 to 0.25 mg/s. The discharge is initiated from a Tungsten cathode, and the solenoid generating the magnetic topology is decoupled from the thruster. Ions reached up to 80 eV when the thrust was between 1 and 1.5 mN. The maximum thrust efficiency has been determined at 8%, with an utilization efficiency of up to 90%. However, experiments were performed with a mean pressure of 10^{-4} mbar. Hence, the aforementioned results warrant careful consideration. In fact, utilization efficiencies greater than 100% had been computed for some operations points. Nevertheless, this work highlights the importance of the MW injecting location. As the R wave can propagate without cutoffs, the MW should be injected above the ECR to achieve higher plasma densities.

Other researchs of interest have been achieved by various research groups. Hooper et al.[18] developed an ECRT based on whistler wave propagation in a 1 m quartz tube, characterized by Stallard et al.[19], [20]. Kammash[21]–[23] focused on the "Gas Dynamic Mirror", expanding the plasma in a magnetic mirror before it reaches a MN.

1.4.2 Recent advances

Since the 2000s, various institutions, research teams and companies have contributed to the development of ECR sources and thrusters. To begin with, the company Reisz Engineers developed an ECRT[24]. The tests described in the aforementioned work were performed in the NASA Marshall Space Flight Center, with a conceptual design shown in Figure 1.1. Argon has been used as a propellant, with a mass flow rate range from 10 sccm to 100 sccm. Two MW sources have been used: a magnetron at 2.45 GHz and a klystron at 10 GHz. An average power of 2 kW has been used with the magnetron. Various magnetic topologies have been tested using 6 coils with different wirings and currents, following the magnetic bottle scheme. Through LIF (Laser Induced Fluorescence) and MW interferometer measurements, an electron density in the 10^{11} cm^{-3} has been probed along with an ion velocity range from 2 km/s to 5 km/s for the fastest Ar^{+} population. These operation points correspond to an I_{sp} of 2000 s to 3000 s.

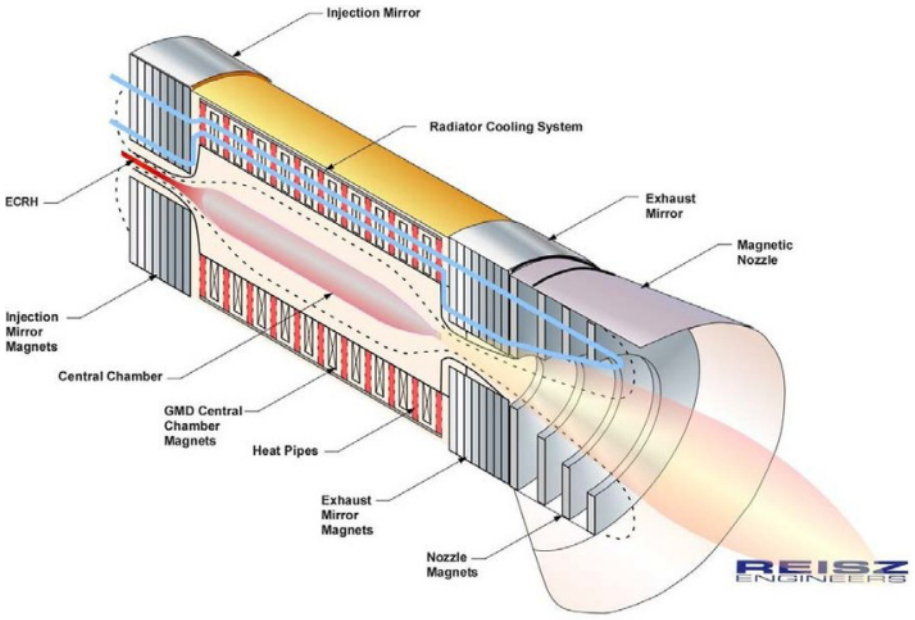

Figure 1.1: Conceptual drawing of an ECR-GDM thruster. Courtesy of Reisz Engineers[22], [24].

The Japanese Aerospace Exploration Agency (JAXA) developed a gridded ECR GIE thruster to equip the Hayabusa mission, with the objective of reaching the Itokawa asteroid, as shown in Figure 1.2. This thruster combines an ECR ion source stage generating the plasma and a set of grids accelerating the latter. Finally, an ECR-powered cathode was used to neutralize the beam coming out of the grids. ECR-powered cathodes represent a good alternative to classic hollow cathodes, providing both lifetime and reliability improvements[25], [26]. However, they are usually designed for a lower current range. This thruster cannot be considered as electrodeless as the grids are immersed in the plasma. Still, investigations and researches[27]–[29] performed through its development deepened ECRT knowledge. A 4.2 GHz MW is brought through waveguides to the ionizationc chamber. The latter is surrounded in a rail-like configuration by magnets generating a sufficient MF to enable the ECR reaction—with $B_{ECR} = 0.15$ T. The magnetic topology associated with the aforementioned configuration enlarges the resonance surface in the IC, while protecting the walls of the IC by screening them magnetically. The success of the Hayabusa mission motivated the JAXA to launch a second mission, Hayabusa II, this time aiming at the Ryugu asteroid. The thruster used in this mission results from an improvement of the first mission's one[30]. These two missions, to the best of the author's knowledge, include the only ECR-type thrusters ever reaching space to date. However, these thrusters are GIEs-like and it is safe to assume that no electrodeless ECRT has reached space yet.

Since 2005, ONERA has developed several ECRT prototypes and has led experimental research through a variety of experiments. A collaboration with Elwing Corp. initiated the research on ECR sources. This collaboration has been followed

Figure 1.2: Hayabusa asteroid explorer executing the powered flight in deep space[31].

by the internal development of a first ECRT lead by Larigaldie[32], presented in Figure 1.3. This first prototype differed from the ECRT norm by its coaxial MW configuration. The use of coaxial elements in the transmission line on the thruster side helps to reduce the size of the latter in opposition with the classic waveguide elements—obviously depending on the working frequency. French[33] and US[34] patents had been issued to secure the technology developed along this prototype, even though this prototype had not been characterized. Arguably, the presence of a coaxial core in the IC implies that this thruster not strictly an EPT device.

An extensive work on the development of new ECRT prototypes has begun in 2012[35], resulting from a collaboration between ONERA and Astrium—currently known as Airbus Defence and Space. The prototypes have the common ground of using a MW at 2.45 GHz with tens of watts. They differ in geometry, gas type and injection and magnetic topologies[36], [37]. This improvement results from the modification of the magnetic topology to purely divergent. Moreover, several gas injection strategies have been explored following the change in magnetic topology. When the gas is injected axially through the rear-plate, it crosses the resonance surface parallel to the latter due to the diverging MF.

The ion energy reached up to 220 eV for Argon and 350 eV for Xenon in the aforementioned prototypes. Several conclusions were drawn from these researches. A decrease in the mass flow rate increases the thruster floating potential and the ion energy in the beam. Moreover, the total current density increases along with the MW power. Finally, Xenon has been determined to be more efficient than Argon, with a thruster utilisation efficiency 40% higher—due to its lower ionization energy and its higher mass. Using a mass flow rate of 0.2 mg/s and a MW power of 50 W, a 500 μN thrust has been estimated for Argon and 850 μN for Xenon.

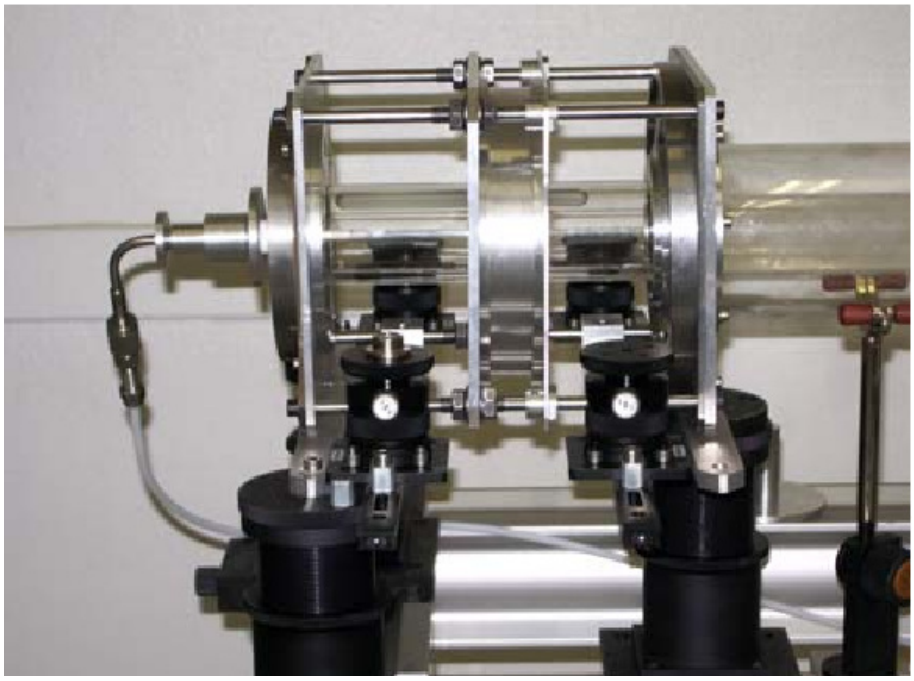

Figure 1.3: ONERA first high power EPT prototype. The propellant injection system appears on the right. MW applicators have been removed. The glass tube on the right is a small vacuum vessel[32].

In 2015, a new ECRT prototype has been developped and tested within the ONERA facilities[39]–[42]. In order to relieve the thermal stress induced by the use of electromagnets, this prototype relies on the use of permanent magnets. It was concluded that reducing the distance between the ECR surface and the gas injection increased the ion current. Moreover, increasing the IC diameter from 13 mm to 27.5 mm leads to a higher electron temperature, hence to a higher utilization efficiency—due to the plasma extraction to wall surface ratio. The prototype proved to be optimal with 0.1 mg/s of Xenon with a MW power of 30 W, with a total efficiency measured at 16% with indirect measurements and 11% with thrust measurements. Finally, the ion energy to electron temperature ratio has proven to be constant regardless of the mass flow rate, for a given magnetic topology.

A certain progress was made by Petershmitt et al.[43] by comparing the MW coupling method between coaxial (i.e. with a CT (Coaxial Termination) inserted in the plasma) and waveguide. The latter showed a lower total efficiency at 1% with 1 sccm of Xenon and 25 W of MW power at 2.45 GHz ; against 5% for the coaxial configuration. Hot electrons, generated at the boundaries of the CT, are believed to be responsible for this efficiency difference. Finally, Desangles et al.[44] improved the ECRA ECRT prototype, as seen in Figure 1.6. This thruster has been tested within the JUMBO facility of the Justus Liebieg University, Germany. Compared to the ONERA facility, a pressure of 1×10^{-7} mbar could be maintained with 2 sccm xenon against 4×10^{-6} mbar. Using such a low pressure allowed to measure a thrust up to

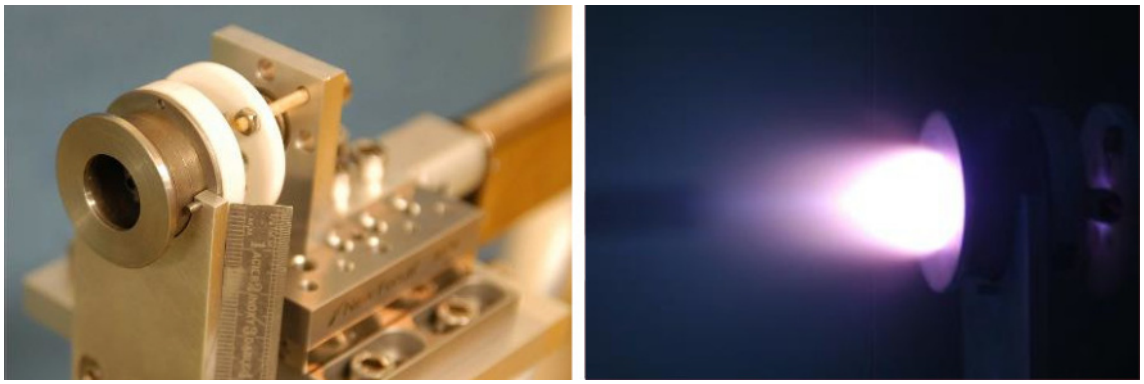

Figure 1.4: ECRA-EVO-0 ECR plasma thruster prototype of ONERA[38].

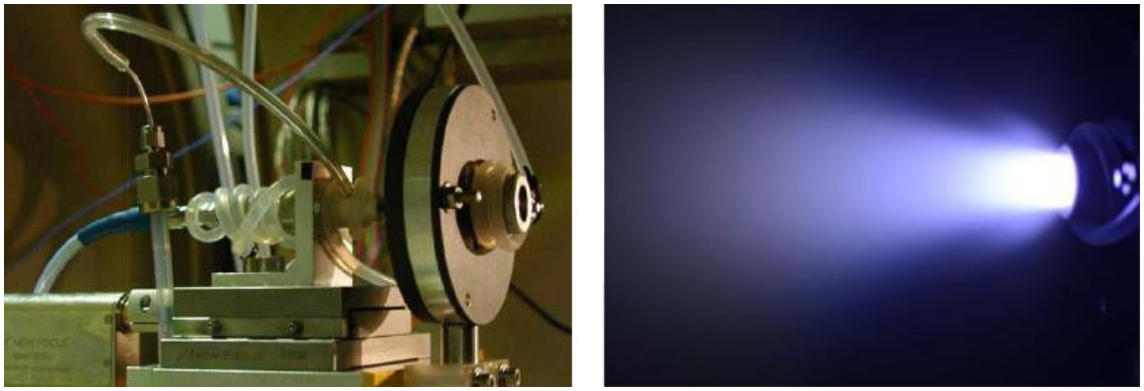

Figure 1.5: ECRA-EVO-2 ECR plasma thruster prototype of ONERA[38].

1.7 times higher than the one measured in the ONERA facility. Indeed, the losses in electron energy were reduced by lowering their collision rate with the neutral background. The final total thrust effeciency was estimated at 50% with both 30 W and 200 W of MW power. Nevertheless, the immersion of a CT within the plasma directly induces erosion, limiting the lifetime and the conservation of the thruster performances in time. The presence of a CT makes the EPT nature of this ECRT questionable, as for the Hayabusa missions.

Other institutions of interest have investigated ECRTs, such as the Plasmadynamics and Electric Propulsion Laboratory (PEPL) in Michigan University, USA. Studies lead by Wachs and Jorns[45], [46] focused on the background pressure effects with a pressure raise from 1×10^{-6} mbar to 6×10^{-5} mbar thanks to the direct injection of Xenon in the vacuum chamber. They confirmed the importance of measuring plasma properties and thrust with the lowest pressure possible. In addition, they investigated the use of a secondary MW frequency to improve the thruster performances. However, this study could not find a relevant advantage on adding a second ECR. Other noticeable advances have been accomplished by the Washington University with the use of water in an ECRT[47]–[49].

Finally, the UC3M EP2 group has investigated ECRTs. Inchingolo et al.[50]–[54] focused on a 5.8 GHz waveguide ECRT with an internal diameter of 36 mm and a

Figure 1.6: Picture of a 30 W ECRA thruster[44].

maximum MW power of 400 W. The thruster injection could be switched from a single to a double injection type, with a maximum Xenon mass flow rate above the expected range (> 40 sccm). The MF generated by electromagnets showed a minor impact on the MW reflection. The latter peaked at 50% for the lowest and highest mass flow rates. The use of FCs evaluated the asymmetry induced by the injection type. The single-point injection produced a strong asymmetry when the double-point injection allowed a symmetric plume to be obtained. The divergence has been determined to be comprised between 35deg and 55deg and inversely proportional to the increase in energy per particle. The maximum utilization efficiency has been measured at 70% with 1 sccm of Xenon and 300 W of MW power. The thrust efficiency has been measured indirectly at 2%.

1.5 Magnetic topologies of interest

Electrodeless plasma thrusters rely on externally applied magnetic fields to guide and accelerate the plasma. Two magnetic configurations are of particular interest in this work: the MN and the MA (Magnetic Arch). Both rely on the conversion of electron thermal energy into directed ion kinetic energy through ambipolar fields, but they differ in their topology and potential advantages.

The MN has been extensively studied as a divergent magnetic structure that efficiently channels plasma expansion and has been applied in several thruster concepts. The MA, by contrast, is a more recent configuration producing a near-dipolar field in which magnetic lines bend and reconnect on the opposite side of the source. It has been proposed to mitigate issues such as rear-plate ion losses, torque induced by the geomagnetic field, and to enable thrust vectoring. A detailed description of these two topologies, including their working principles, numerical simulations, and relevant experimental studies, is presented in Chapter 2.

1.6 Thesis motivation and objectives

The studies made upon ECRTs in the recent years justify the progressive interest in the development of alternatives to classic HETs or GIEs. Thanks to the absence of electrodes immersed in the plasma, a variety of gases can be consider as propellants. Moreover, the available power range allows to adapt these thrusters to different kinds of missions. The latest and impressive progress realized in ONERA[39]–[44] allows to consider ECRTs as major actors in the space propulsion field. Despite aiming to focus the plasma beam, MNs fail to reach low plume divergence such as in classic HETs or GIEs. In addition, the magnetic topology formed in MN-based EPTs forms a strong dipole moment interacting with the ambient MF, specifically the geomagnetic field. This moment produces a torque on a spacecraft. Moreover, the magnetic lines intersect the material walls in the rear part of the IC, guiding the plasma flow in that direction. Hence, up to 50% of the ions created in the IC recombine at the rear-all[55]. Half of the coupled power is thus lost, constituting a major limitation for the ECRTs.

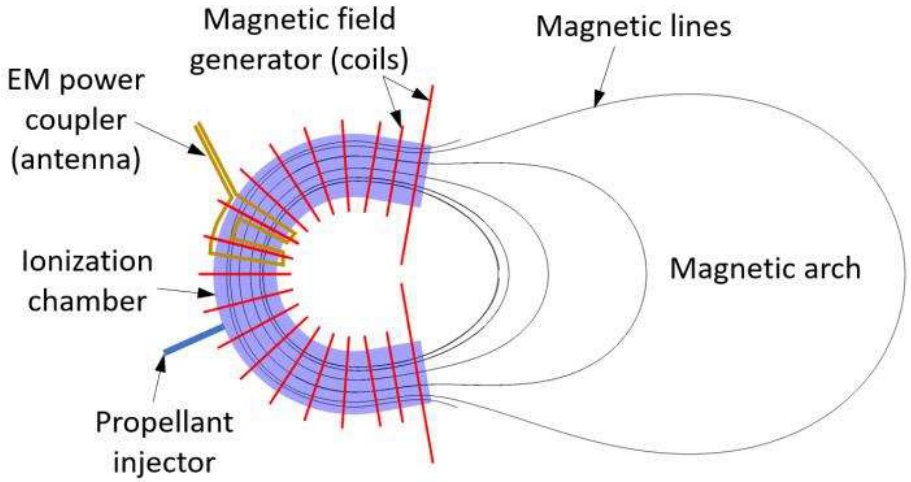

Figure 1.7: Sketch of the MA-EPT[56].

In 2018, Merino proposed a patent that defines a C-shaped thruster[56] associated with a MA, as shown in Figure 1.7. This new topology solves the problematic cited before. A neutral propellant gas is injected into the C-shaped thruster chamber and is ionized by the applied electro-magnetic fields. The MFLs guide the plasma to the two exhausts of the C-shape thruster, while shielding the walls and enabling the propagation and absorption of the electromagnetic waves. Plasma expansion occurs at the C-shaped thruster exhausts, marking the beginning of the MA. The plasma acceleration takes place in the body of the MA, and the plasma-induced MF deforms and stretches the latter downstream when the applied MF becomes weaker, enabling plasma ejection and generating thrust. The MA can be considered as two independent MNs with opposite polarities, hence the plasma expansion in the MA also appears when combining two cylindrical ECR sources with opposed polarity.

This new magnetic topology presents a near-zero net dipole, thus lowering the aforementioned magnetic torque felt by the spacecraft. Not only would this magnetic topology narrow the pros of classic EPTs, but it would also enable thrust vectoring without moving parts by acting on each MWG (Micro Wave Generator). Moreover, it could ease the integration of the thruster in a satellite/spacecraft, improve its performance, and reduce the amount of propellant to take onboard.

The development and characterization of such a new class of plasma thrusters is fundamental to pushing the frontiers of space propulsion. However, it is still unknown whether the mechanisms involved in the electromagnetic heating and the transport of the plasma are identical in a closed-line geometry as classic. Similarly, the concept of the MA for plasma acceleration, where the plasma-induced MF plays a central role, is completely new in the context of EP, and is considered here for the first time.

The primary objective of the thesis is to assess if a plasma jet can be extracted from a MA. Then, the plasma properties, as well as the thrusters characterisation and the ion acceleration analysis are explored. In the first place, two prototypes of two ECR-sources have been developed to answer this question, followed by the preliminary development of a C-shaped thruster. These milestones allow to follow a consistent path through the PhD, in order to answer the problematic of the viability, characteristics, and performances of the successive prototypes. For each prototype, the following steps were followed mainly with an experimental approach: design, assembly, test and characterization of the prototype ; achieve thruster ignition and assess operation points of interest ; measure plasma properties through different diagnostics such as ion current, ion most probable energy, ion and electron densities, etc... ; modify the prototype to reach the most viable MA prototype possible.

The development of the MA prototypes have mainly been conducted within the facilities of the EP2 laboratory in the UC3M University. This includes the use of the vacuum facility and existing electrostatic probes such as LPs, FCs, RPA and thermocouples. The probes are mounted on a robotic arm to obtain a 2D map of the plasma properties[57]. Finally, 2D LIF measurements have been performed on the second MA prototype at the CNRS-ICARE Laboratory, Orléans, France, through an international research stay.

1.7 Thesis outline

The rest of the present manuscript is organized as follows:

- **Chapter 2** presents the working principle of the MN and the MA through both simulations and experimental studies.
- **Chapter 3** focuses on the characterisation of the experimental apparatus used

through the different prototypes developped in the thesis frame.

– **Chapter 4** presents the development and the characterization of the first MA prototype using a pair of coaxial electron cyclotron resonance sources with opposing magnetic polarities. RPA measurents were performed for 2 different magnetic topologies in a single source configuration and 3 for the dual-sources. This chapter represents a transcription of a peer-reviewed journal paper "Ion current and energy in the MA of a cluster of two ECR plasma sources"[58] published in the Journal of Electric Propulsion, 2025, February 25; 4,10. Doi: 10.1007/s44205-025-00100-w.

– **Chapter 5** focuses on the second MA prototype. A first experimental campaign has been performed in the UC3M facilities with electrostatic probes such as FCs, LPs and RPA to determine the thruster optimal operating points. A 2D LIF experimental campaign has been executed in the CNRS-ICARE Laboratory in Orléans, France. Parts of the contents of this chapter have been presented at the International Electric Propulsion Conference 2024 with an oral presentation and related conference manuscript[59]. A journal paper based on this chapter is under preparation.

– **Chapter 6** presents the development, the assembly and the testing of the first MAT (Magnetic Arch Thruster) with a C-shape IC.

– **Chapter 7** gathers the results and contributions brought by this thesis and sets the ground for a number of future lines of work.

Chapter 2

Magnetic nozzle and magnetic arch

2.1 Magnetic nozzle

A MN (Magnetic Nozzle) consists of a MF (Magnetic Field) externally applied to a plasma to expand and guide it in vacuum. Figure 2.1 shows a schematic view of a MN. As mentioned in Section 1, MN is used in a variety of thrusters, with numerous pros and cons. When subjected to a sufficiently strong MF, electrons exhibit well-defined magnetization, orbiting around MFLs (Magnetic Field Lines) while drifting azimuthally due to the ExB drift. In contrast, heavier ions tend to be only partially magnetized or, in some cases, remain totally unmagnetized. The electron population is characterized by a high temperature, whereas ions are generally assumed to be cold. Because of their much higher mobility, electrons tend to move faster along theMN than ions. This charge separation induces an ambipolar electric field that slows down electrons and accelerates ions, ensuring that both species propagate downstream together while preserving quasi-neutrality of the plasma. This potential converts the electron thermal energy into ion kinetic energy. Among the electrons gyrating around MFLs, only the ones with enough energy can escape the potential well to neutralize the plasma beam far downstream, giving a current-free plume. Because of the radial confinement imposed by the MN, the lateral diffusion of electrons is significantly restricted. This constraint facilitates efficient conversion of plasma internal energy into a well-collimated high-energy ion beam.

In a MN-based thruster, such as ECRTs (Electron Cyclotron Resonance Thrusters) or HPTs (Helicon Plasma Thrusters), force transmission is based on the combination of pressure thrust F_p and magnetic thrust F_m. The pressure thrust comes from both the ion and electron pressures upon the internal walls of the thruster/source, when the magnetic one comes from the Lorentz force. Magnetic thrust is believed to be responsible for up to 80% of the total thrust, based on previous experiments[60], [61].

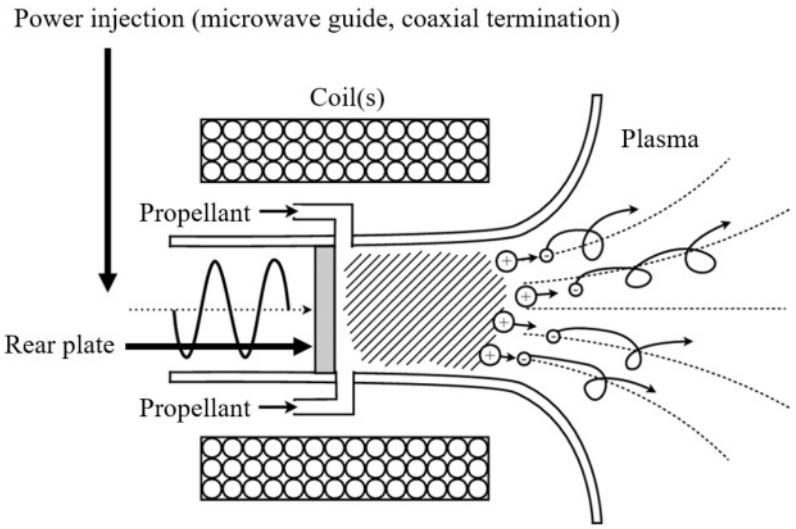

Figure 2.1: Sketch of a simple MN.

2.2 Magnetic arch

2.2.1 Working principle

The MA (Magnetic Arch) is a magnetic configuration proposed as an alternative to the magnetic nozzle for electrodeless plasma acceleration. It consists of a set of magnetic field lines forming an arched structure, typically generated by two parallel coils and/or permanent magnets with opposite polarity. Unlike a simple divergent nozzle, the arch produces a near-dipolar topology in which magnetic field lines emerge from one side of the source, bend in the plume region, and return to the opposite side.

The working principle of the MA relies on the same plasma expansion mechanisms as in a magnetic nozzle: electrons, being more mobile, tend to follow magnetic field lines more easily than ions. This differential mobility leads to the establishment of ambipolar electric fields that accelerate ions along the expanding field lines. In the case of the MA, these field lines are strongly curved and close back to the source region. The resulting geometry modifies the plasma expansion compared with the nozzle: it redirects part of the ion flow along the arch, redistributes the current density, and could enable thrust vectoring by adjusting the relative currents in the conductors.

2.2.2 Magnetic arch simulations

The clustering of two MNs with opposing polarities is been labelled in the previous chapter as a MA. Even though interest in the clustering of EP (Electric Propulsion) devices has grown significantly since the 2000s, it mainly remains aimed towards

HETs (Hall Effect Thrusters)[62]–[68]. Some conclusions can still be drawn from these experimental studies. The ion energy and density profiles change from a single thruster to a cluster. A linear superposition of the respective profiles differs from the measurements obtained from a cluster.

Merino et al.[69], [70] were the first to approach the MA with 2D simulations. It has been concluded that even when electrons are fully magnetised, ions can form a free jet piercing through the closed lines of the MF. This last point supports the feasibility of the MA topology for plasma. Furthermore, the simulations reveal that plasma detachment from the MA is influenced by the plasma beta expansion and the magnetic topology, with partial detachment occurring as the field lines open downstream. Di Fede et al.[71] realised the first 3D simulations on the clustering of HPTs. They confirmed the previously cited work conclusion on the reduction of the divergence angle by the closed-line MF topology. They also noticed a potential drop through the plasma plume, linked to the stream of electrons navigating in between the HPTs.

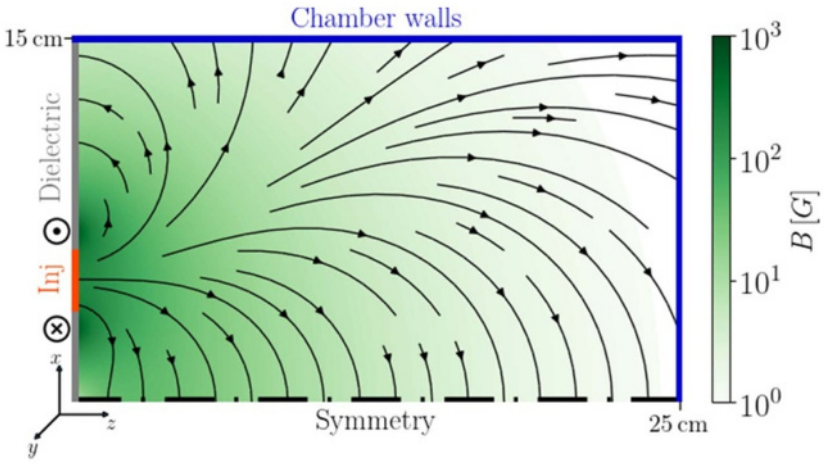

Figure 2.2: Sketch of the reference simulation domain and of the boundary conditions applied for a planar MA. The two counter-streaming current wires and the plasma source are infinite in the y direction. The green color-map and the streamlines display the intensity and direction of the MF for the reference case. Courtesy of Guaita et al.[72].

Guaita et al.[72] performed PIC (Particle-In-Cell)/Fluid simulations of the MA plasma expansion in a 2D plane. The magnetic field used in the simulations is shown in Figure 2.2. A double-peaked IVDF (Ion Velocity Distribution Function) has been observed near the symmetry plane, indicating that ions from each source retain their distinct characteristics even after merging, leading to localized heating. The Hall parameter χ impact on the plasma parameters depends on its value. For high χ, the magnetic pressure dominates over the plasma pressure. Hence, plasma properties become insensitive to further increases in the MF strength. However, for lower values of χ (i.e. $\chi \leq 10$), the plasma pressure starts to compete with

magnetic pressure and the confining effect of the MF weakens, allowing plasma to diffuse across the magnetic lines. As the magnetic pressures weaken, the magnetic thrust decreases. Moreover, the plume divergence increases as the beam becomes less collimated. The presence of magnetic drag near the symmetry plane in the region where the magnetic lines become perpendicular to the plasma flow has been observed, as in Merino et al.[70]. The presence of a background neutral population (representing the experimental vacuum chamber environment) results in increased plume divergence due to resonant CEX (Charge Exchange Collision) between the plasma ions and neutral atoms, which scatter ions and increase the lateral spread of the plume. It is important to underline that the interaction region between two beams is difficult to model. Indeed, Merino et al. fluid model[70] predicted a shock-like structure, while Guaita et al.[72] kinetic model showed a more gradual structure. Hence, the model type influences the conclusions drawn from the simulations.

2.2.3 Clustering experiments

Vereen et al.[73], [74] demonstrated experimentally the effect of clustering on two HPTs with the same polarity, as shown in Figure 2.3. However, their clustering is more akin to the merging of the exhausts of two HPTs than to a cluster of HPTs linked by a MA. Still, both the plasma density and ion exit velocity have increased, resulting in an upgrade in the thruster's performances. This work remains the only experimental study to the clustering of HPTs.

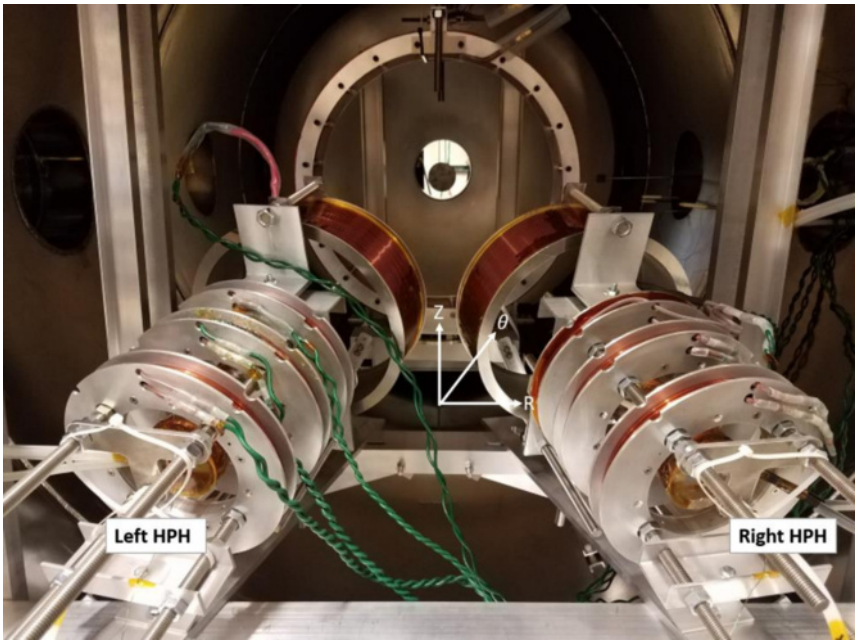

Figure 2.3: Experimental setup of the clustered HPH system—Two HPH thrusters attached to thruster chassis. Courtesy of Vereen et al.[73], [74].

Chapter 3

Characterisation of experimental apparatuses

This chapter depicts the characterisation of the elements used to build the successive prototypes ECRC1 (Electron Cyclotron Resonance Cluster 1), ECRC2 (Electron Cyclotron Resonance Cluster 2) and MAT (Magnetic Arch Thruster).

3.1 Electromagnetic coils for the MAT

3.1.1 Magnetic topology

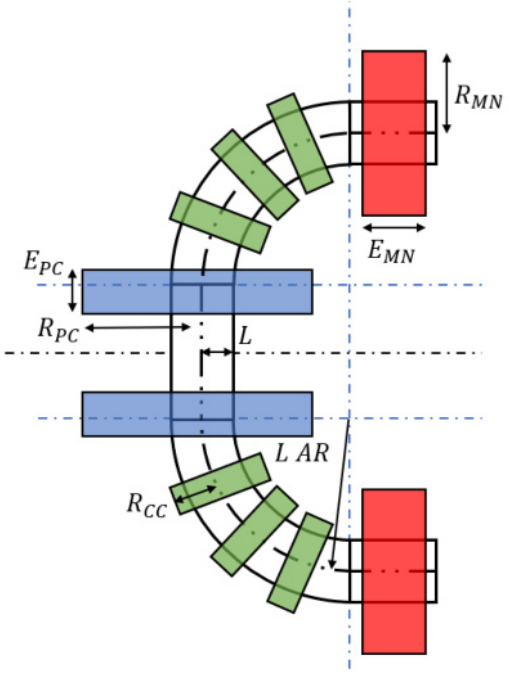

Figure 3.1: MAT configuration with the IC superposed by three types of coils: PCs in blue, CCs in green and MNs in red.

Figure 3.1 depicts the general aspect of the MAT from Merino[56]. The IC (Ionisation Chamber) is made of a single non-magnetic stainless steel (SS316L with $\mu_{r,max} = 1.01$ at 20°C) tube with an inner radius of L. The curvature is defined

by the AR (Aspect Ratio). The latter corresponds to the ratio between the radius of curvature and the inner radius of the tube L. Three sets of coils are used to confine the plasma in the stainless steel tube at best. To begin with, the PCs (Principal Coils) generate a sufficiently strong MF (Magnetic Field) to reach the ECR resonance field—875 G, associated to a MW (Micro Wave) frequency of 2.45 GHz. The CCs (Continuous Coils) bend the MFLs (Magnetic Field Lines) so that these latter remain parallel to the walls of the IC. Finally, the MNs (Magnetic Nozzles) accelerate and expand the plasma. The coil sizing, presented in Section 3.1, results from several trade-offs faced during the development of the MAT. The inner-tube surface seen by the plasma through its expansion in the IC had to be kept as low as possible. Hence, the total length of the tube remained a constraint. However, although coils have been chosen for their flexibility, they cannot generate a MF strong enough without the use of a high current. Adding more turns/layers per coil could reduce the input current to generate a given MF, but the thruster's C-shape structure limits the coils size when the total length of its IC is at stake. Therefore, these trade-offs have led to an inner radius of 15 mm and an AR of 5.

Coil reference		***CCs***	***PCs***	***MNs***
Simulations	***Nb. of turns/layer***	12	17	29
	Nb. of layers	25	25	30
	Total nb. of turns	300	425	870
Manufactured	***Nb. of turns/layer***	~ 11	~ 16	~ 27
	Nb. of layers	28	28	35
	Total nb. of turns	245	407	810

Table 3.1: Comparison of the number of turns and layers between the simulations and the manufactured coils.

The MF generated by the coils needs to be adapted and optimized for the MAT to reach a sufficient magnitude to enable ECR while keeping the MFLs parallel to the IC walls. MF simulations have been performed to determine the best possible layout, according to the coils physical limitations. Still, some differences appear between the simulations and the experimentally measured behavior of the coils, beginning with the number of turns per layer and the number of layers as shown in Table 3.1. Moreover, coils are approximated in the simulations as a series of thin loops.

The magnetic topology inside the prototype has to be optimised to maximise operation time while ensuring sufficient magnetic strength to enable the electron cyclotron resonance. A MatLab code has been developed to simulate in 3D the magnetic topology of the coils shown in Figure 3.1. In every figure in this section, the red line represents the resonance line of 875 G. The two magenta curves represent the walls of the IC. The MFLs are shown in black. The optimised configuration for each coil is the following:

– $I_{PC} = 6.3\,\text{A}$.
– $I_{CC} = 6\,\text{A}$.
– $I_{MN} = 5\,\text{A}$.

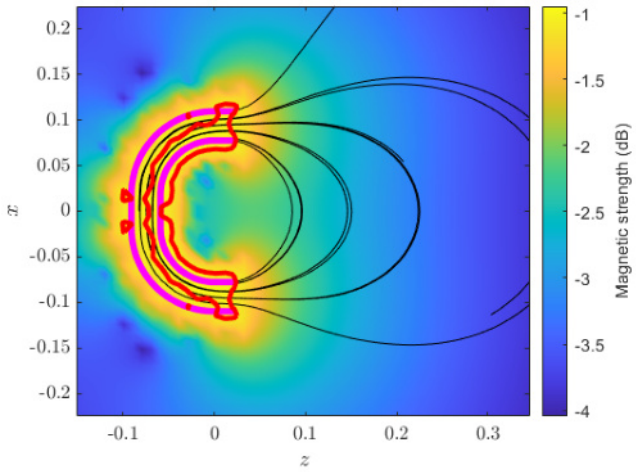

Figure 3.2: Colormap of the MAT magnetic topology with $I_{PC} = 6.3\,\text{A}$, $I_{CC} = 6\,\text{A}$ and $I_{MN} = 5\,\text{A}$.

To optimize the operation time and reduce the risks of degradation, it is better to remain with the optimized configuration shown in Figure 3.2. Still, increasing the current in the MNs would lower the divergence even more. However, it affects the topology in the thruster by removing the resonance line from the internal side of the central part and moving it to its external side. This can be seen in Figure 3.3.

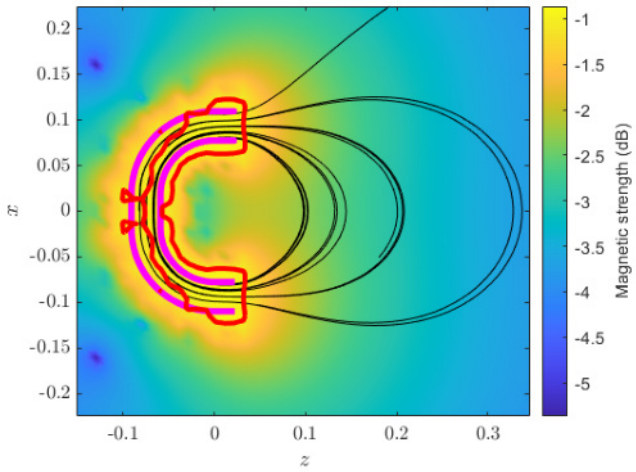

Figure 3.3: Colormap of the MAT magnetic topology with $I_{PC} = 6.3\,\text{A}$, $I_{CC} = 6\,\text{A}$ and $I_{MN} = 7\,\text{A}$.

Table 3.2 shows the differences between the simulations and the experimental measurements. They are due to the error in each coil resistance. They do not

exceed 17 W for cold conditions, and 28 W for the $T = 180°C$. The manufactured coils remain in an acceptable range regarding the simulations, as it can be seen in Table 3.2.

Config.	**Cold: T=25°C**		**Hot: T=180°C**		**Crit: T=250°C**	
	P (W)	***Diff. (W)***	***P (W)***	***Diff. (W)***	***P (W)***	***Diff. (W)***
Theor.	683.5	0	1103.3	0	1292.8	0
Manuf.	720.5	36.9	1163.0	59.7	1362.8	69.9
Multi.	718.5	35	1159.9	56.6	1359.1	66.3

Table 3.2: Differences of power between simulations and experimental measurements.

3.1.2 Magnetic field probing

Probing setup and hardware

Independent simulations of each coil were performed to compare with the experimental data. Measurements of the MF have been done thanks to the Model 460 3-Channel Gaussmeter of Lake Shore Cyrotronics. The HSE (High SEnsitivity probe) has been used along the Gaussmeter with the following parameters shown in Table 3.3.

Range	**Resolution**	
	AC, or DC with Filter Off	***DC Filter On***
±3 T	±0.0001 T	±0.00001 T
±300 mT	±0.01 mT	±0.001 mT
±30 mT	±0.001 mT	±0.0001 mT
±3 mT	±0.0001 mT	±0.00001 mT

Table 3.3: Characteristics of the Gaussmeter HSE.

The measurements have been done in the configuration shown in Figure 3.4. The hardware has been calibrated thanks to a zero Gauss chamber and the Gaussmeter calibration tool, as seen in Figure 3.5. The reference plane of each coil was set to its exit plane. In Figures 3.7, 3.8 and 3.9, the reference plane is set to 0 mm. During the tests, the coils were powered by an EA Elektro-Automatik EA-PS 2084-10B power supply.

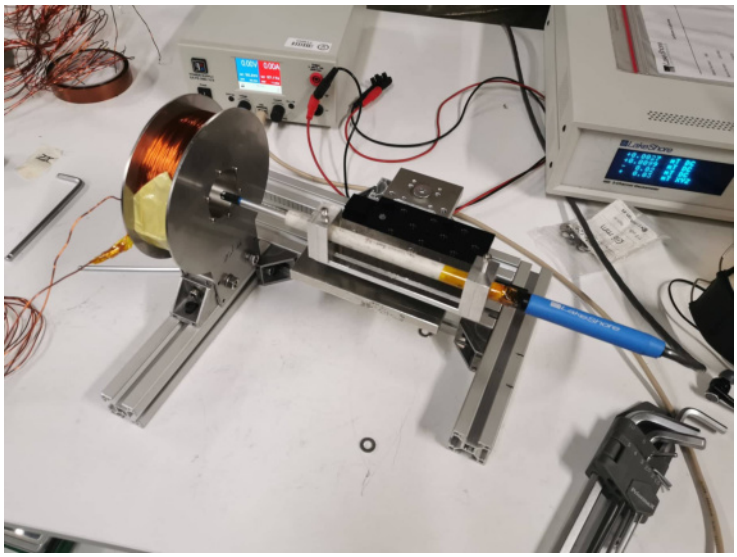

Figure 3.4: Setup of the probing of the MF of a MN.

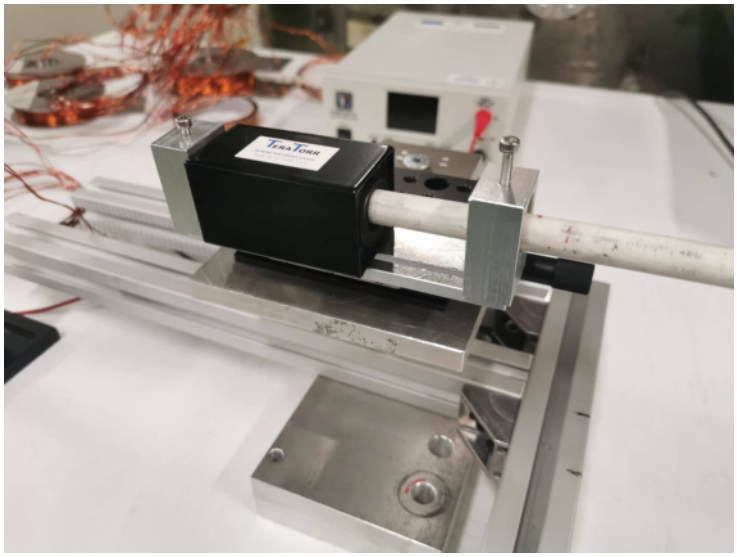

Figure 3.5: Zero Gauss chamber installed on the tip of the HSE to calibrate the Gaussmeter.

The MF probe has offsets to be corrected when probing the coils. As it can be seen in Figure 3.6, the active areas for each component of the MF have their offset (2.08 mm for the X and Y components, and 1.08 mm for the Z one).

Measurements of the magnetic field in the MAT coils

The current input in eachCC is $I_{CC} = 6.7\,\mathrm{A}$. The coil simulated in the simulations is considered perfect, without any wild winding and with perfectly aligned loops. However, it should be noted that the CCs are very similar to each other, as shown in Figure 3.7. Indeed, they produce the same profile of MF magnitude with negligible

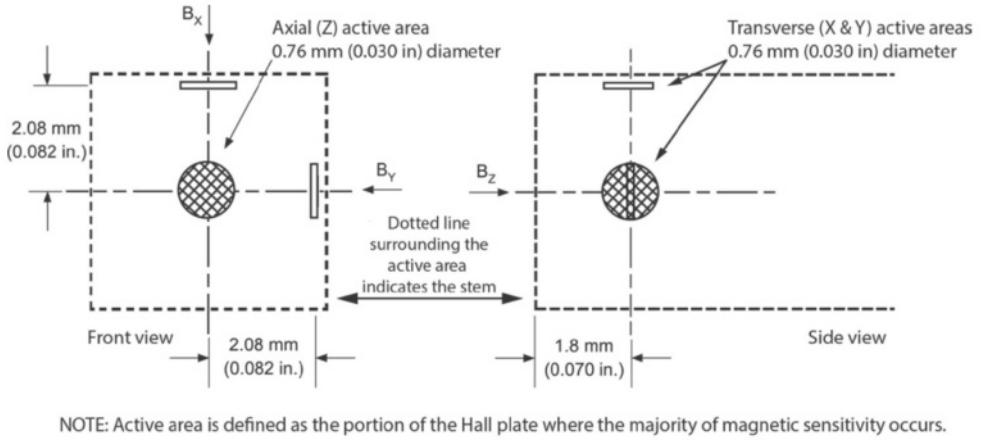

Figure 3.6: Scheme of the offsets of the HSE used to probe the MF.

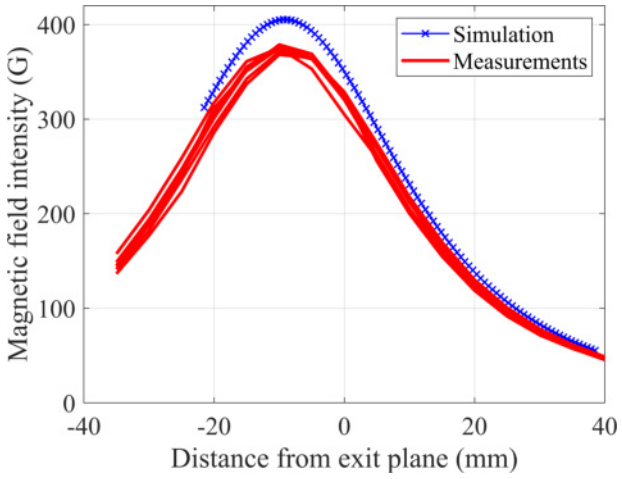

Figure 3.7: Measurements-simulation comparison for CCs.

differences. This similarity between the coils implies that correcting one coil to another is not mandatory. However, an increase in current is necessary to reach the desired magnetic magnitude in the CCs. This increase in current will be applied to every CC to have a consistent MF in the elbow parts of the thruster.

The PCs magnetic strength measurements fit the simulations perfectly. Their reduced thickness and packing factor help to achieve a meager difference with the simulated MF. Correcting the input current in these coils is unnecessary, as seen in Figure 3.8 as a difference inferior to 10 G is considered negligible.

The MNs represent the most significant gap between the magnitude of the simulated MF along the axis and the measurements. Both coils are similar, but the difference with the simulations goes up to 80 G, as seen in Figure 3.9. As for the CCs, it is necessary to apply a correction to be as close as possible to the simulations. Measurements have also been performed to determine the accuracy of the B field out of the axis, with negligible asymmetries.

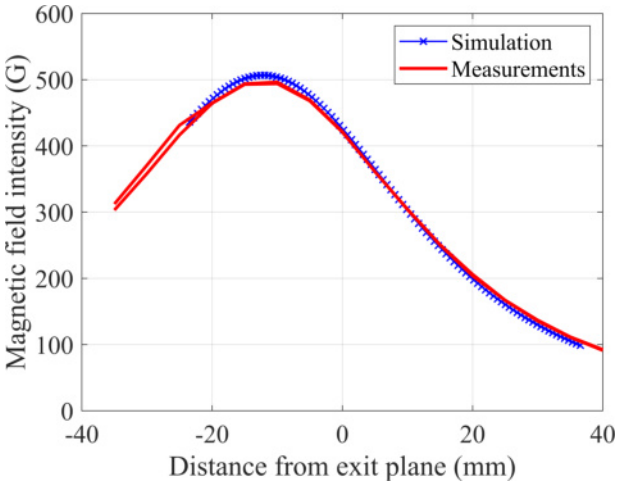

Figure 3.8: Measurements-simulation comparison for PCs.

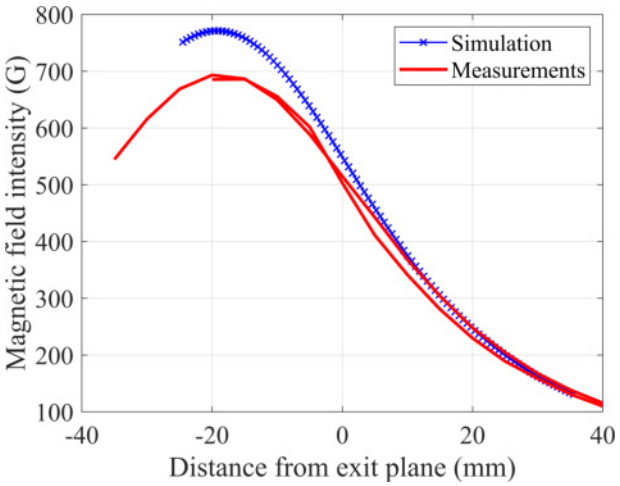

Figure 3.9: Measurements-simulation comparison for MNs.

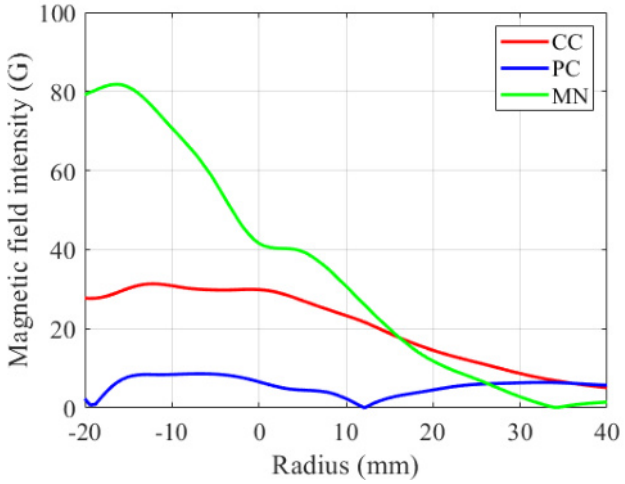

Figure 3.10: Measurements-simulation differences for each set before correction.

Current correction using first probing measurements

Coil	**CC**	**PC**	**MN**
Initial current (A)	6.7	7	5.19
Corrected current (A)	7.17	7	5.825
Initial power at 25°C (W)	50.2	86.2	105
Corrected power at 25°C (W)	54.21	104	130.05
Initial maximum MF (G)	375.16	498.12	691.25
Corrected maximum MF (G)	405.18	498.12	777.35

Table 3.4: Comparison between currents, powers and magnetic intensities before and after correction.

As mentioned in Section 3.1.2, it is necessary to apply a correction to the coils to be as close as possible to the simulations in terms of MF magnitudes. The simulations have determined a well-optimised topology enabling ECR along the thruster chamber. Even though the MW is evanescent due to the diameter and length of the IC in vacuum, the optimisation of the ECR surface continuity is still helpful to guaranty as much generation of plasma as possible. The CCs and the MNs need a current correction to reduce the differences in the simulations. Table 3.4 sums up each coil's difference in current, powers and magnetic intensities.

3.1.3 Coils resistance and heating

Using the Keithley 2100 6 1/2-Digit Resolution Digital Multimeter, the resistance of each coil has been measured before and after the thruster first ignition. The differences between the first and second measurements ($< 10\,\%$) can be explained by experimental inaccuracies. Indeed, the measurements were done in both cases without proper connectors to plug in the multimeter. Still, the coils resistance measurements throughout the measurements help to determine the degree of the coils integrity in order to maintain the optimal MF shown in Section 3.1.1.

As mentioned in previous sections, the coils are withstanding more than 7 A to produce a MF strong enough to reach the magnetic strength enabling ECR. This current input induces heating as a result of the Joule effect. It is possible to determine the order of magnitude of the heating evolution and the maximum operating time. Thus, some experimental heating measurements have also been taken to adjust for them. In order to avoid any deterioration, the thermocouples are placed on the grounded stainless steel side cover of the coils. The temperatures are regularly checked during operation to ensure that the limit temperature—180°C for the coils wire—is not exceeded. It is possible to compute the temperature from the resistivity as presented in Equation 3.1.

$$T = T_0 + \frac{1}{\alpha}\left(\frac{\rho(T)}{\rho_0} - 1\right). \tag{3.1}$$

The resistivity can be linked to the characteristics of the wire to obtain the resistance, as $\rho = R\,\frac{A_{CS}}{l}$. A_{CS} is the cross-sectional area and l the length of the copper wire. As these two parameters do not vary for a given coil, Equation 3.1 can be written as a function of resistance, as in Equation 3.2.

$$T = T_0 + \frac{1}{\alpha}\left(\frac{R(T)}{R_0} - 1\right). \tag{3.2}$$

3.1.4 Power supplies management

The main limitation of the coil setup remains the lack of high-current feedthroughs in the vacuum chamber. The number of pins available is reduced to 16 instead of 20 needed to connect all coils to independent power supplies. More than one coil can be connected in series to one power supply to reduce the number of pins needed. The coil distribution will be driven by the experiments and the different steps of the first ignition. However, a general distribution can still be made, as seen in Table 3.5.

Power supply	**Current (A)**	**Voltage (V)**	**Coil**
BK PRECISION 9117	120	80	PC1 — PC2
8A-600V	8	600	MN1 — MN2
EA-PS 2084-10 B	10	84	CC1.1 — CC2.1 CC1.2 — CC2.2 CC1.3 — CC2.3

Table 3.5: Power supplies distribution.

This configuration would allow the use of only 10 pins, as the coils are used in pairs: two MNs on the 8A-600V PS, two PCs on the BK PRECISION 9117 PS, and one pair of CCs per EA-PS 2084-10 B.

3.2 Transmission line for the MAT

The MAT TL (Transmission Line) comprises all the elements present in the MW line from the MWG (Micro Wave Generator) to the thruster. These elements comprise coaxial cables, connectors, feedthroughs, coaxial to waveguide transitions, etc... They are all made with male-female 7/16 DIN connectors. Figures 3.13, 3.19 and 3.20 represent examples of the TL used for the different prototypes.

3.2.1 Transmission line theory

Shift in reference planes

Each element of a TL is defined by its scattering matrix. This matrix relates the amplitudes (magnitude and phase) of traveling waves, both incident and reflected. Thus, the reference planes must be specified for each port of the matching network. This shift in between the original and the new reference planes changes the scattering matrix.

It is mandatory to apply this shift of reference planes in the characterization of certain element of the TL. Indeed, the TL has been characterized thanks to a VNA (Virtual Network Analyser). This characterization has been done to determine the scattering matrix of every element in the line, apart from the coaxial cables used to link the TL to the VNA (as they have already been taken into account in the calibration of the VNA). The standard use for connectors in the studied TL is 7-16 DIN. As the coaxial cables used to link the VNA and the TL are equipped with N-Type connectors, some N-Type to 7-16 DIN must be used. These connectors are considered to be near lossless, but induce a shift in the reference planes that must be taken into account to fully define the TL. It is useful to specify that the TL studied here is a cascade of two-ports elements.

$$\left[V^{-}\right] = [S]\left[V^{+}\right], \tag{3.3a}$$

$$\left[V^{'-}\right] = [S']\left[V^{'+}\right]. \tag{3.3b}$$

Adapting from Figure 3.11, Equations 3.3 link the incident and reflected port voltages. V^{-} (reflected voltage wave), S (scattering matrix) and V^{+} (incident voltage wave) are referenced to the original planes at $z_n = 0$, and $V^{'-}$, S' and $V^{'+}$ refer to the new planes at $z_n = l_n$. Given the MAT TL, $l_n = l$ is considered a constant since the adapters from N-Type to 7-16 DIN are similar and are placed on both sides of the TL. As two ports are taken into account, the n-index (position or sequence of a particular port) present in the next equations could be replaced by 1 or 2—designating the first and second ports of the VNA (the first and second ports of the TL). Using the theory of traveling waves on lossless TLs, the shifted plane voltage can be expressed as a function of the original plane voltage and the electrical length of the outward shift of the reference plane as shown in Equations 3.4.

$$V_n^{'-} = V_n^{-} e^{-j\theta_n}, \tag{3.4a}$$

$$V_n^{'+} = V_n^{+} e^{j\theta_n}. \tag{3.4b}$$

The electrical length θ_n is defined in Equation 3.5.

$$\theta_n = \beta_n l. \tag{3.5}$$

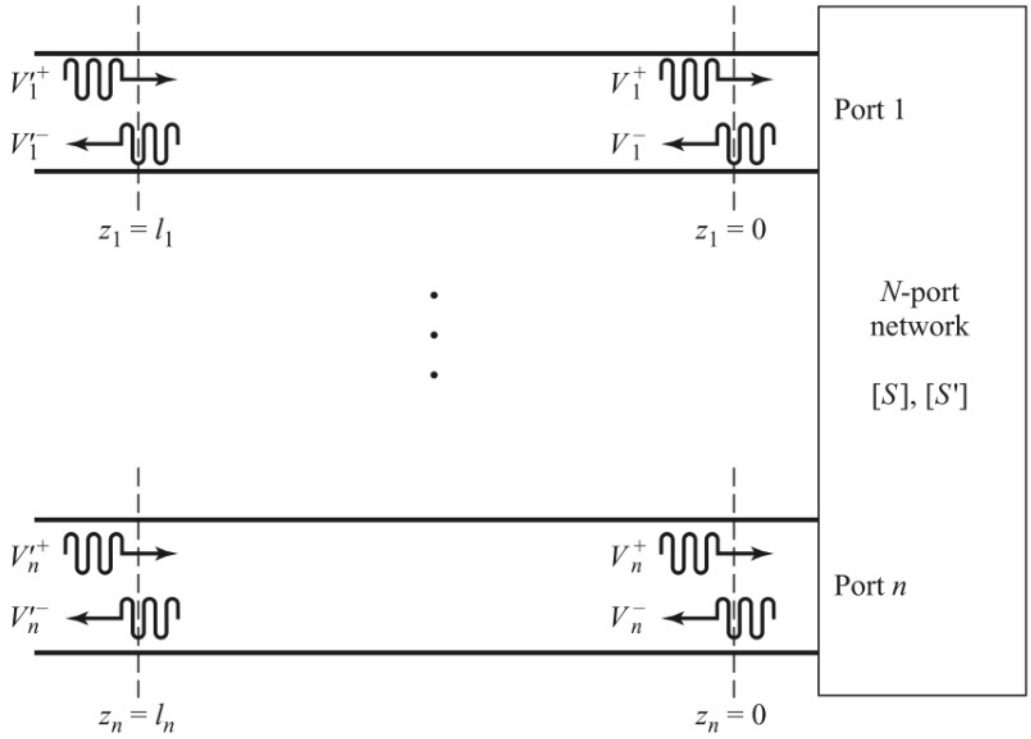

Figure 3.11: Shifting reference planes for an N-port matching network, from Pozar[75].

The total voltage of a terminated lossless TL can be expressed as a sum of the incident and reflected waves as expressed in Equation 3.6.

$$V(z) = V^+ e^{-j\beta z} + V^- e^{j\beta z}. \tag{3.6}$$

In order to match with the MAT TL, the length z corresponds to $-l$, transforming Equation 3.6 into Equation 3.7.

$$V(l) = V_n'^+ + V_n'^- = V^+ e^{j\beta z} + V^- e^{-j\beta z}. \tag{3.7}$$

As aforementioned, the length between two planes is constant as the same adapters are used on both sides of the TL. Its value is 40.5 mm, corresponding to the distance between the two sides of the N-Type to 7-16 DIN adapter. Moreover, β corresponds to the complex propagation constant, which is a function of the frequency in Equations 3.8a. It is also directly related to the wavelength and the phase velocity in Equations 3.8b and 3.8c.

$$\gamma = \alpha + j\beta = \sqrt{(R + j\omega L)(G + j\omega C)}, \tag{3.8a}$$

$$\lambda = \frac{2\pi}{\beta}, \tag{3.8b}$$

$$v_p = \frac{\omega}{\beta} = \lambda f. \tag{3.8c}$$

The wavelength can be determined by using the speed of the phase velocity and a correction factor due to the dielectric medium of the coaxial cable/adapter. In Equation 3.9, this correction factor is linked to the inverse of the square root of the dielectric constant of the material.

$$v_{p_{CC}} = \frac{v_{p_{Vacuum}}}{\sqrt{\varepsilon_{PTFE}}}. \tag{3.9}$$

Considering PTFE as the dielectric material inside the coaxial cables and the adapters (from the manufacturers documentations), it is possible to approximate the new phase velocity around $1.9678 \times 10^8\,\mathrm{m/s}$. Using Equation 3.8c, the wavelength of the MW is approximately 80.7 mm. Thus, the value of β is $51.35\,\mathrm{m}^{-1}$. Therefore, the electric length is constant with respect to the TL of interest, with a value of $\theta_n = \theta = 3.15$.

The scattering matrix of the TL purged from the changes implied by the shift of the reference planes can be obtained as a function of the original scattering matrix. Using Equations 3.4, the original incident and reflected waves voltages can be obtained:

$$V_n^- = V_n'^- e^{j\theta_n}, \tag{3.10a}$$
$$V_n^+ = V_n'^+ e^{-j\theta_n}. \tag{3.10b}$$

By replacing in Equation 3.3a, the known scattering matrix $[S]$ of the original plane can be linked to the voltages of the new shifted plane.

$$\left[V^-\right] = [S]\left[V^+\right], \tag{3.11a}$$
$$\left[V'^-\right]\begin{bmatrix} e^{j\theta_1} & 0 \\ 0 & e^{j\theta_2} \end{bmatrix} = [S]\begin{bmatrix} e^{-j\theta_1} & 0 \\ 0 & e^{-j\theta_2} \end{bmatrix}\left[V'^+\right], \tag{3.11b}$$
$$\left[V'^-\right] = \begin{bmatrix} e^{j\theta_1} & 0 \\ 0 & e^{j\theta_2} \end{bmatrix}^{-1}[S]\begin{bmatrix} e^{-j\theta_1} & 0 \\ 0 & e^{-j\theta_2} \end{bmatrix}\left[V'^+\right], \tag{3.11c}$$
$$\left[V'^-\right] = \begin{bmatrix} e^{-j\theta_1} & 0 \\ 0 & e^{-j\theta_2} \end{bmatrix}[S]\begin{bmatrix} e^{-j\theta_1} & 0 \\ 0 & e^{-j\theta_2} \end{bmatrix}\left[V'^+\right]. \tag{3.11d}$$

However, Equation 3.3b indicates that $\left[V'^-\right] = [S']\left[V'^+\right]$, therefore the scattering matrix of the TL with the shift in the reference planes can be written as a function of the scattering matrix of the original TL and the electrical length in Equation 3.12.

$$[S'] = \begin{bmatrix} e^{-j\theta_1} & 0 \\ 0 & e^{-j\theta_2} \end{bmatrix}[S]\begin{bmatrix} e^{-j\theta_1} & 0 \\ 0 & e^{-j\theta_2} \end{bmatrix} \tag{3.12}$$

The components of the new scattering matrix can be expressed as Equations

3.13.

$$S'_{11} = e^{-2j\theta_1} S_{11}, \tag{3.13a}$$
$$S'_{12} = e^{-j(\theta_1+\theta_2)} S_{12}, \tag{3.13b}$$
$$S'_{21} = e^{-j(\theta_1+\theta_2)} S_{21}, \tag{3.13c}$$
$$S'_{22} = e^{-2j\theta_2} S_{22}. \tag{3.13d}$$

As the adapters on both side of the TL are similar, θ is constant regardless of the port.

$$S'_{11} = e^{-2j\theta} S_{11}, \tag{3.14a}$$
$$S'_{12} = e^{-2j\theta} S_{12}, \tag{3.14b}$$
$$S'_{21} = e^{-2j\theta} S_{21}, \tag{3.14c}$$
$$S'_{22} = e^{-2j\theta} S_{22}. \tag{3.14d}$$

Transmission matrices of 2-ports transmission line elements

Matching networks can consist of cascade connections of two-port TL elements. During the characterization of the elements composing the TL used as power injection for the MAT, some elements could not be tested alone in the two ports of the VNA. As an example, the feedthrough of the vacuum chamber has female connectors on both sides. However, the N-Type to 7-16 DIN adapters used on both ports of the VNA also have female-female connectors. Hence, some intermediary TL elements must be used to connect the VNA and the feedthrough. The easiest way to make this connection is to use coaxial cables. These male-male coaxial cables can be characterized alone with the VNA, so their scattering matrix can be determined. The scattering matrix of the full assembly—containing the N-Type to 7-16 DIN adapters, the coaxial cables and the feedthrough—can also be characterized, as well as its scattering matrix. Knowing the scattering matrix of every element in a TL except one allows to determine the scattering matrix of the uncharacterised element.

In order to remain as general as possible, a TL composed of 3 elements is shown in Figure 3.12. The full assembly can be purged of the effect of the shift in reference planes of the N-Type to 7-16 DIN adapters. In addition to the scattering matrix, it is useful to describe the elements of a TL by their transmission matrix. Scattering matrices describes input-output wave relations, when transmission matrices describes voltage-current transformations.

The voltage and current at the entry terminal of each element can be expressed as a function of the voltage and current of the end terminal as in Equation 3.15.

$$\begin{pmatrix} V_n \\ I_n \end{pmatrix} = \begin{bmatrix} A_n & B_n \\ C_n & D_n \end{bmatrix} \begin{pmatrix} V_{n+1} \\ I_{n+1} \end{pmatrix} \tag{3.15}$$

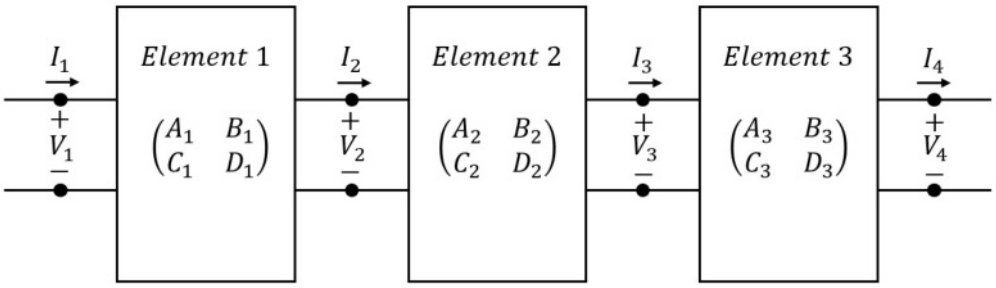

Figure 3.12: TL composed of 3 2-ports elements.

Therefore, the current and tension of the third element can be linked to the current and tension at the entry of the first element.

$$\begin{pmatrix} V_1 \\ I_1 \end{pmatrix} = \begin{bmatrix} A_1 & B_1 \\ C_1 & D_1 \end{bmatrix} \begin{bmatrix} A_2 & B_2 \\ C_2 & D_2 \end{bmatrix} \begin{bmatrix} A_3 & B_3 \\ C_3 & D_3 \end{bmatrix} \begin{pmatrix} V_4 \\ I_4 \end{pmatrix} \tag{3.16}$$

The product of the transmission matrix can be reduced to a fourth matrix to ease the understanding.

$$\begin{pmatrix} V_1 \\ I_1 \end{pmatrix} = \begin{bmatrix} A_{Total} & B_{Total} \\ C_{Total} & D_{Total} \end{bmatrix} \begin{pmatrix} V_4 \\ I_4 \end{pmatrix}, \tag{3.17}$$

$$\begin{bmatrix} A_{Total} & B_{Total} \\ C_{Total} & D_{Total} \end{bmatrix} = \begin{bmatrix} A_1 & B_1 \\ C_1 & D_1 \end{bmatrix} \begin{bmatrix} A_2 & B_2 \\ C_2 & D_2 \end{bmatrix} \begin{bmatrix} A_3 & B_3 \\ C_3 & D_3 \end{bmatrix}. \tag{3.18}$$

This new matrix characterizes the transmission of the full TL. Knowing the transmission matrix of at least two elements of the TL in addition to the one of the whole assembly enable the determination of the transmission matrix of the remaining unknown element. The uncharacterised element can be in three different positions, changing the computations to obtain its transmission matrix.

$$\begin{bmatrix} A_1 & B_1 \\ C_1 & D_1 \end{bmatrix} = \begin{bmatrix} A_{Total} & B_{Total} \\ C_{Total} & D_{Total} \end{bmatrix} \begin{bmatrix} A_3 & B_3 \\ C_3 & D_3 \end{bmatrix}^{-1} \begin{bmatrix} A_2 & B_2 \\ C_2 & D_2 \end{bmatrix}^{-1}, \tag{3.19a}$$

$$\begin{bmatrix} A_2 & B_2 \\ C_2 & D_2 \end{bmatrix} = \begin{bmatrix} A_1 & B_1 \\ C_1 & D_1 \end{bmatrix}^{-1} \begin{bmatrix} A_{Total} & B_{Total} \\ C_{Total} & D_{Total} \end{bmatrix} \begin{bmatrix} A_3 & B_3 \\ C_3 & D_3 \end{bmatrix}^{-1}, \tag{3.19b}$$

$$\begin{bmatrix} A_3 & B_3 \\ C_3 & D_3 \end{bmatrix} = \begin{bmatrix} A_2 & B_2 \\ C_2 & D_2 \end{bmatrix}^{-1} \begin{bmatrix} A_1 & B_1 \\ C_1 & D_1 \end{bmatrix}^{-1} \begin{bmatrix} A_{Total} & B_{Total} \\ C_{Total} & D_{Total} \end{bmatrix}. \tag{3.19c}$$

There are some direct correspondences between the scattering matrix parameters

and the transmission matrix parameters, as seen in Equations 3.20.

$$S_{11} = \frac{A + \frac{B}{Z_0} - CZ_0 - D}{A + \frac{B}{Z_0} + CZ_0 + D}, \tag{3.20a}$$

$$S_{12} = \frac{2\left(AD - BC\right)}{A + \frac{B}{Z_0} + CZ_0 + D}, \tag{3.20b}$$

$$S_{21} = \frac{2}{A + \frac{B}{Z_0} + CZ_0 + D}, \tag{3.20c}$$

$$S_{22} = \frac{-A + \frac{B}{Z_0} - CZ_0 + D}{A + \frac{B}{Z_0} + CZ_0 + D}. \tag{3.20d}$$

Using the previous equations, it is possible to express the parameters of the transmission matrix as a function of the parameters of the scattering one.

$$A = \frac{\left(1 + S_{11}\right)\left(1 - S_{22}\right) + S_{12}S_{21}}{2S_{21}}, \tag{3.21a}$$

$$B = Z_0\frac{\left(1 + S_{11}\right)\left(1 + S_{22}\right) - S_{12}S_{21}}{2S_{21}}, \tag{3.21b}$$

$$C = \frac{1}{Z_0}\frac{\left(1 - S_{11}\right)\left(1 - S_{22}\right) - S_{12}S_{21}}{2S_{21}}, \tag{3.21c}$$

$$D = \frac{\left(1 - S_{11}\right)\left(1 + S_{22}\right) + S_{12}S_{21}}{2S_{21}}. \tag{3.21d}$$

Thanks to these equations, it is possible to convert the known scattering matrices into transmission matrices, then to determine the transmission matrix of the uncharacterised element to convert it into a scattering one. The previous demonstration can also be adapted for a two-elements TL, as in Equations 3.22.

$$\begin{bmatrix} A_{Total} & B_{Total} \\ C_{Total} & D_{Total} \end{bmatrix} = \begin{bmatrix} A_1 & B_1 \\ C_1 & D_1 \end{bmatrix}\begin{bmatrix} A_2 & B_2 \\ C_2 & D_2 \end{bmatrix}, \tag{3.22a}$$

$$\begin{bmatrix} A_1 & B_1 \\ C_1 & D_1 \end{bmatrix} = \begin{bmatrix} A_{Total} & B_{Total} \\ C_{Total} & D_{Total} \end{bmatrix}\begin{bmatrix} A_2 & B_2 \\ C_2 & D_2 \end{bmatrix}^{-1}, \tag{3.22b}$$

$$\begin{bmatrix} A_2 & B_2 \\ C_2 & D_2 \end{bmatrix} = \begin{bmatrix} A_1 & B_1 \\ C_1 & D_1 \end{bmatrix}^{-1}\begin{bmatrix} A_{Total} & B_{Total} \\ C_{Total} & D_{Total} \end{bmatrix}. \tag{3.22c}$$

The two-elements or three-elements methods can be used not only to determine the transmission and scattering matrices of an TL element, but of a n-elements part of a TL. Nevertheless, it is mandatory to know the scattering matrix of at least one element in the n-element TL part to determine the transmission and scattering matrix of the other elements.

Insertion losses

The ILs (Insertion Losss) help to understand the extra loss produced by the introduction of an element in a TL. It can be expressed as a function of the S_{21} parameter

of its scattering matrix. The ILs can be expressed in dB or in percents, as shown in Equations 3.23. The ILs do not comprise the reflected power per se. The latter influences the ILs, as less power reaches each component of the TL through reflection at its input and output.

$$IL = 20log_{10}\left|S_{21}\right| dB, \tag{3.23a}$$

$$IL = 100\left(1 - 10^{20log_{10}|S_{21}|}\right) \%. \tag{3.23b}$$

3.2.2 Full transmission line

The TL carries the MW power from the MWG to the thruster and comprises several elements, as seen in Figure 3.13. First, RAs (Right Angle connectors) bring the TL to the vacuum chamber and make it fit in the latter. Moreover, coaxial cables of different lengths are to join the various elements/connectors. The coaxial feedthrough ensures the continuity of the TL through the vacuum chamber body. Finally, two C2Ws (Coaxial-to-Waveguide adapters) are placed one in front of the other and spaced by 1 mm, acting as a DC-block, to ensure that the shield of the TL reaching the thruster remains floating. This decoupling is necessary for the plume to remain quasi-neutral and to ensure that no net current is leaving the thruster. Finally, a panel crimp connector transfers the power to the CT (Coaxial Termination). These elements have been characterized to assess the power forwarded to the thruster.

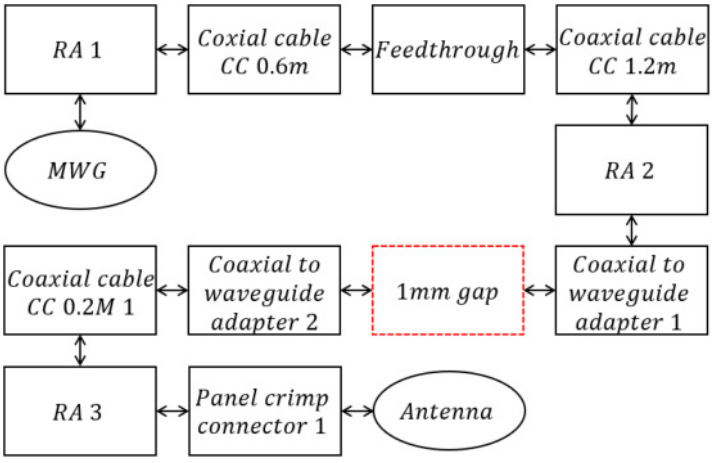

Figure 3.13: Configuration of the TL full assembly.

3.2.3 Insertion losses in the transmission line

Coaxial cables

- **Main coaxial cables**

It is mandatory to determine the ILs of each coaxial cable. As aforementioned, these coaxial cables are LMR-600-FR cables manufactured by TIMES MICROWAVES SYSTEMS. This grade of coaxial cable is designed to withstand high power (up to 0.5 kW) to the detriment of transmission quality, as shown in Table 3.6.

Freq. (MHz)	200	450	900	1500	1800	2000	**2500**	5800	8000
Att. (dB/100m)	3.9	5.6	8.2	10.9	12.1	12.8	**14.5**	23.8	29.0
Average P (kW)	1.97	1.35	0.93	0.70	0.63	0.59	**0.52**	0.32	0.26

Table 3.6: Attenuation and average power of the coaxial cables from the TIMES MICROWAVE SYSTEMS.

It is essential to determine the ILs of the coaxial cables with a VNA, as the connectors on both sides of the coaxial cables induce more losses. However, using the theoretical attenuation would help to estimate the ILs with respect to the length of the coaxial cables. The .S2P file containing the complex scattering matrix has been obtained for each coaxial cable thanks to the VNA. Using Equations 3.23, it is possible to determine their ILs in dB. The experimental ILs at 2.45 GHz can be compared with the theoretical ones obtained by the attenuation of the coaxial cable data sheet's, as seen in Table 3.7. The connectors on both sides of the coaxial cables logically add more ILs.

Coaxial cable reference	**CC1**	**CC2**	**CC3**
Length (m)	0.2	1	0.7
Theoretical losses (dB)	-0.029	-0.145	-0.1015
Experimental losses (dB)	-0.037	-0.161	-0.1184
Δ ***losses (dB)***	0.0078	0.016	0.0169

Table 3.7: Experimental and theoretical ILs of the main coaxial cables at 2.45 GHz.

- **Spare coaxial cables**

The following spare coaxial cables are considered. As the main ones, these cables are LMR-600-FR cables. They are composed of the same 7-16 male connectors at each end. It is possible to compute their theoretical ILs, as shown in Table 3.8.

Coaxial cable length	**0.2m**	**0.6m**	**1.0m**	**1.2m**
Losses (dB)	-0.029	-0.087	-0.145	-0.174

Table 3.8: Theoretical ILs of the spare coaxial cables at 2.45 GHz.

Right angle connectors

- **Main right angle connectors**

RAs are used in the TL to connect the waveguide to coaxial transitions to the thruster. Due to its 90deg angle, this component induced more losses than a simple straight adapter, such as the N-type to 7-16 DIN ones. A coaxial cable had to be used due to male-female connector issues in order to test this element with the VNA. The assembly can be schematized as in Figure 3.14.

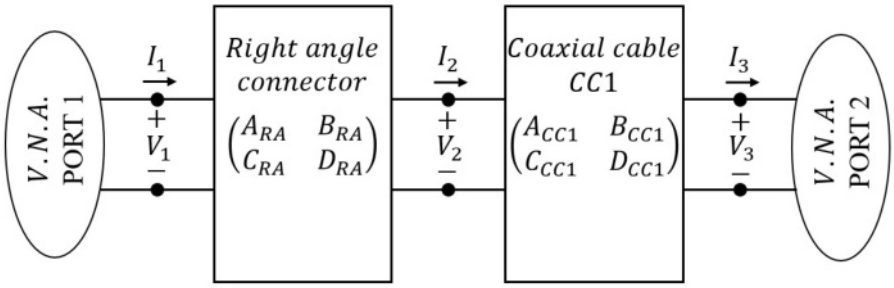

Figure 3.14: Assembly of the RA with $CC1$.

The cable $CC1$ has been used as it has the lowest ILs due to its shorter length. As for the coaxial cables, the shift in reference planes theory has been used to clean the scattering matrix from the N-type to 7-16 DIN adapters. Moreover, the scattering matrix of each RA has been obtained thanks to their transmission matrix. Thus, the ILs of each RA can be determined, as shown in Figure 3.15. Positive ILs correspond to gain in the TL. However, obtaining gain in a passive element like a RA is theoretically impossible. Thus, positive ILs between 2.42 GHz and 2.44 GHz might come from a calibration error in the VNA.

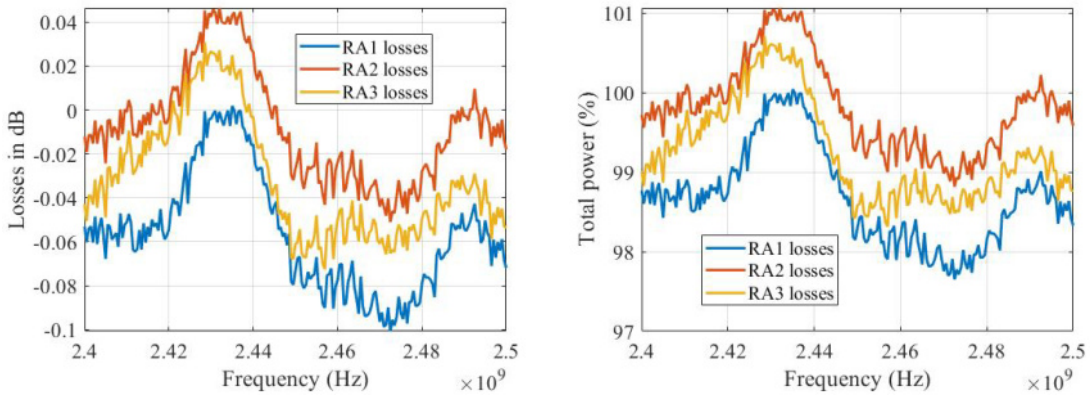

Figure 3.15: ILs in the three main RAs.

Feedthrough

It is possible to determine the ILs of the feedthrough thanks to the transmission matrices. The assembly used to test the feedthrough can be seen in Figure 3.16. The shortest coaxial cables have been used to reduce the attenuation in the TL as much as possible.

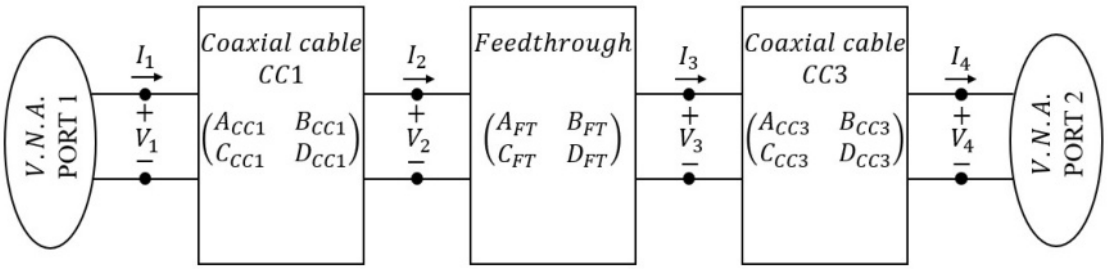

Figure 3.16: Feedthrough test assembly with $CC1$ and $CC3$.

Because of the power it can withstand in a concise length, the feedthrough has the highest ILs relative to its length. Moreover, this component is critical to the integrity of the TL and the chamber.

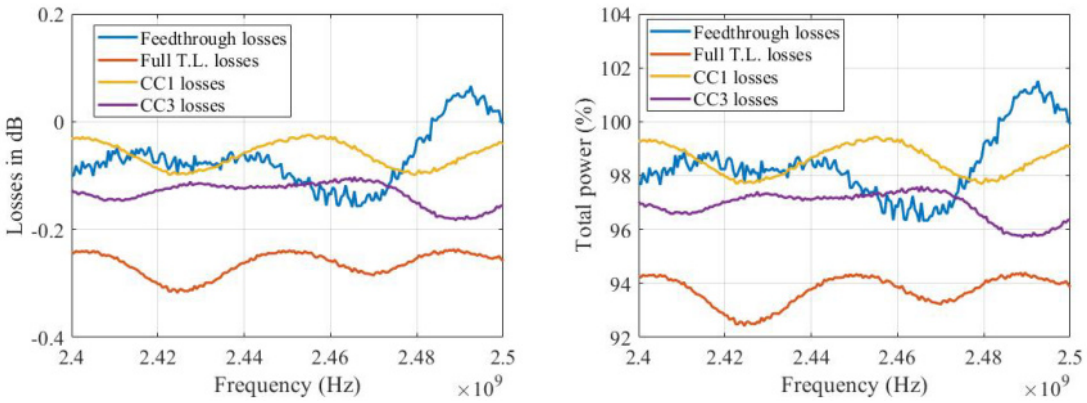

Figure 3.17: ILs in the feedthrough with $CC1$ and $CC3$.

As for the RAs, some gain appears between 2.48 GHz and 2.5 GHz as seen in Figure 3.17. This artifact would be explained for the same reasons.

Coaxial-to-waveguide adapters

Figure 3.18 shows the ILs of the coaxial waveguide adapters. Figure 3.19 shows the configuration used during the measurements. A 1 mm gap is made using ceramic washers to electrically isolate the two C2Ws. This gap can be extended to 2 mm or 3 mm. However, it is better to keep it as small as possible. Indeed, even though the two waveguides are aligned at best, a slight misalignment could induce MW

leakage. Thus, reducing the distance between the two waveguides reduces this possible leakage. However, reducing the gap also increases the possibility of a voltage breakdown. This phenomenon is unlikely to happen because the assembly will be used at very low pressure, where Paschen's curve goes up.

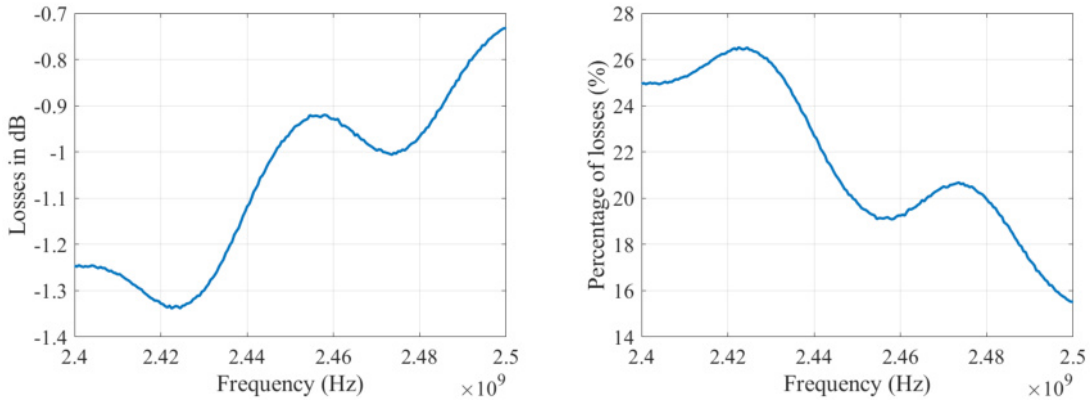

Figure 3.18: ILs in the C2Ws put one in front of the other with a 1 mm gap.

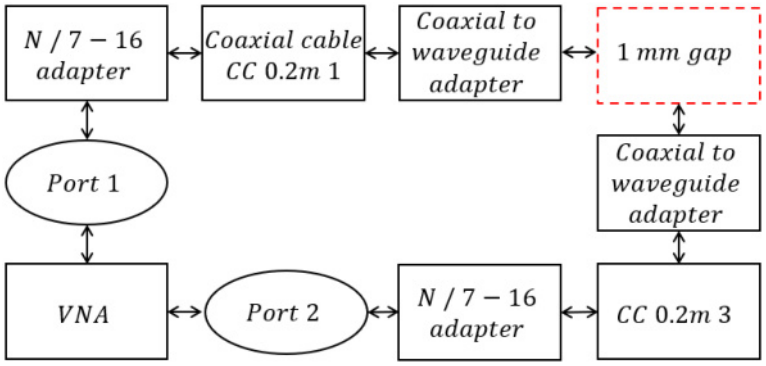

Figure 3.19: Configuration used to measure the ILs of the C2Ws.

Possible explanations of the positive losses

In Figures 3.15 and 3.17, some positive ILs appear respectively between 2.4 GHz and 2.44 GHz, and 2.48 GHz and 2.5 GHz. Some reasons have already been listed to explain these positive ILs, but an additional one could explain these issues. The VNA has been calibrated thanks to the laboratory calibration kit. However, only the S_{11} and the S_{22} parameters have been calibrated. In fact, the calibration kit has only one-port for calibration terminations. Thus, the transmission parameters S_{12} and S_{21} were not calibrated by the elements of the calibration kit. Moreover, the transmission parameters have been calibrated by an N-type male to N-type male connector, which is not meant to be used in a calibrating TL. This connector reduces the accuracy of the measurements of the TL elements with low ILs. Indeed, their ILs is within the range of errors of the aforementioned connector. It appears that

the errors implied by the connector become more and more important along with the frequency, as in the range of MHz the positive ILs are not seen.

Complete transmission line

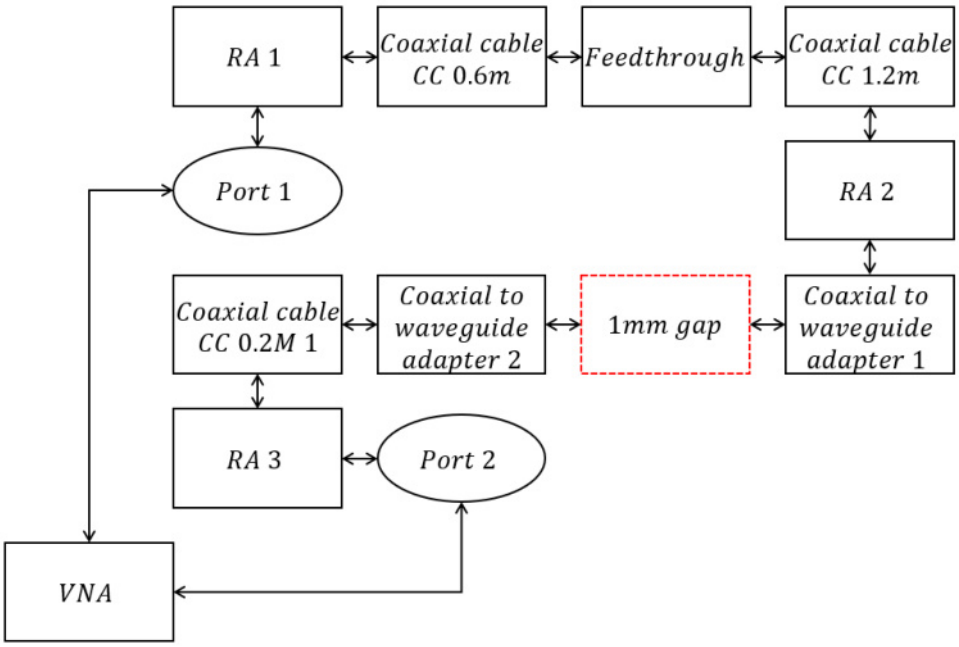

Figure 3.20: Configuration used to measure the ILs of the full TL.

The TL has been completed outside the vacuum chamber to measure the ILs from the MWG to the last RA. However, it is impossible to determine the ILs induced by the panel crimp, as its output is an M3 threaded rod linked to the CT. The configuration used during these measurements is shown in Figure 3.20. Figure 3.21 depicts the ILs measured in this configuration. At 2.45 GHz, around 28% of the power generated by the MWG is lost before reaching the thruster. Most of the TL elements are within the vacuum chamber. Hence, thermal issues might arise due to the heating induced by these losses. As no convection occurs in vacuum and the conduction is limited—especially after the C2Ws transition, TL elements are prone to heat and degrade through operation, particulary as the MW power rises.

3.2.4 Forwarded and reflected power from the microwave generator

The power has been fully transmitted for both configurations without any reflection. However, even though the MWG would displays a reflected power, the latter should be considered with caution. In fact, a complete TL would comprise at least a double-directional coupler with power meters to measure accurately the forwarded

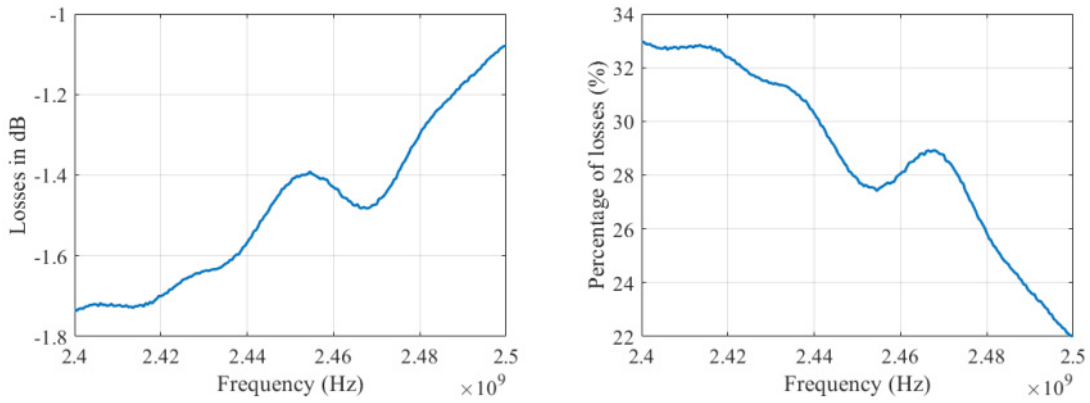

Figure 3.21: ILs in the complete TL.

and reflected power and a matching network. Without these additional elements, it is hard to conclude the real reflected power.

Chapter 4

Initial characterization of the plasma plume in an ECRT cluster

In this chapter, the feasibility of a novel MA (Magnetic Arch) topology for controlled contactless plasma beam acceleration is experimentally demonstrated using a pair of coaxial ECR (Electron Cyclotron Resonance) sources with opposing magnetic polarities, such that their respective MNs (Magnetic Nozzles) connect to form a closed-line configuration. This prototype is referred to as ECRC1 (Electron Cyclotron Resonance Cluster 1). RPA (Retarding Potential Analyser) measurements are taken for a single source and the two sources with the same and opposing polarities, as well as no applied MF (Magnetic Field), showing that the MA yields higher maximum ion current and lower plume divergence angle than other alternative configurations, albeit the most probable ion energy is lower than for a single MN, in agreement with existing models. This validation paves the way to clustering magnetic-nozzle-based plasma thrusters for space propulsion.

This chapter represents a transcription of the following journal paper (without the introduction section):

- **Boyé C.**, Navarro-Cavallé J. and Merino M., "Ion current and energy in the magnetic arch of a cluster of two ECR plasma sources". Journal of Electric Propulsion. 2025, February 25; 4,10. Doi: 10.1007/s44205-025-00100-w.

4.1 ECRT cluster architecture

This work aims to validate experimentally the MA for plasma acceleration. A setup consisting of two coaxial ECRTs (Electron Cyclotron Resonance Thrusters) firing in parallel and a RPA mounted on a rotating arm as a first approach to characterise the plasma expansion at the MA is proposed. First, the ion current density and energy measurements of a single source is used to serve as a baseline for the comparison. Then, the cluster of two sources with identical and opposing magnetic polarities and without an applied MF are characterized. The measurements demonstrate that a plasma beam can be extracted from the closed-line MA topology, with high current density and minor divergence than identical polarities, albeit with a lower ion energy.

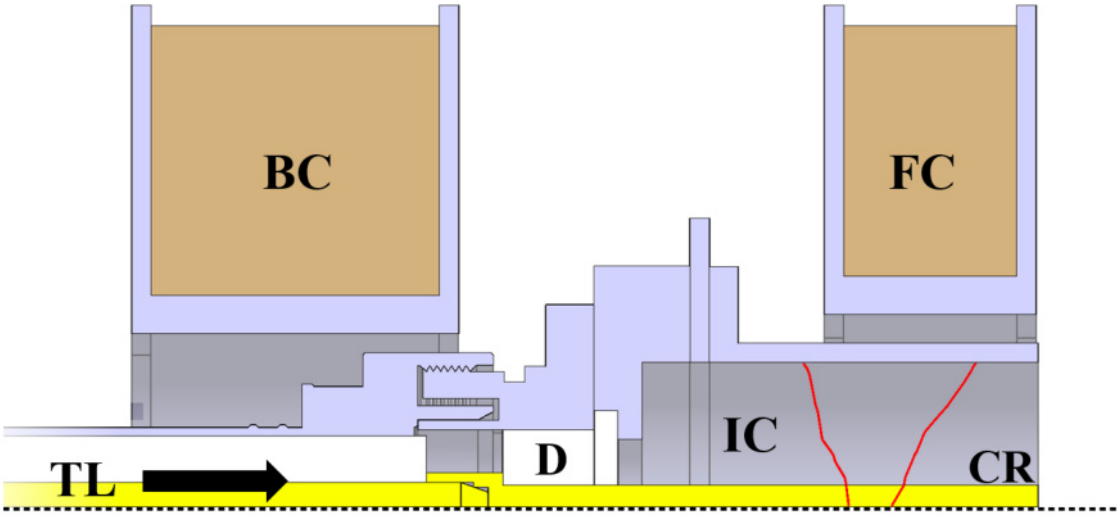

Figure 4.1: Sectional view of a single ECR source. The Ionisation Chamber (IC), the Back Coil (BC), the Front Coil (FC), the Dielectric Window (D), the Coxial Termination (CT) and the TL are shown.The locus for the 875 G resonance is displayed in red.

The cross-sectional view of one of the two identical coaxial ECRT sources used in this study is depicted in Figure 4.1. Each source comprises the following main elements: a forward and a backward magnetic coil, (FC and BC), gas injection, power injection, IC (Ionisation Chamber), and CT (Coaxial Termination). The main design and operational parameters are listed in Table 4.1. The IC and CT are made of stainless steel. The CT is threaded to an M3 core coaxial termination, connecting it to the TL (Transmission Line) thanks to a 7-16 DIN panel crimp. A pierced alumina disk sealed with ceramic paste is placed right after the panel crimp ending to protect it from the plasma at the back of the source. A dielectric holding system supports the assembly to keep it electrically floating. When the two sources are mounted in the cluster configuration, their axes of symmetry are placed parallel on a horizontal plane at a distance of 130 mm.

The two magnetic coils of each ECRT are made of 1 mm in diameter enamelled copper wire and are operated with independent power supplies. The BC is behind the IC and provides most of the applied MF. The FC, smaller, is placed near the plasma exhaust plane, allowing trimming of the MN. Both coils are used simultaneously to achieve the MF strength B_a slightly greater than the resonant field (875 G) inside the source, under the FC. This results in the ECR condition being met at two neighboring surfaces, as displayed in red in Figure 4.1. The applied wave can deposit power on the plasma electrons via collisional absorption in the whole IC, and resonantly at these locations. Indeed, the applied microwave transfers energy to electrons through both collisional absorption in the IC—set by the local collisionality—and cyclotron-resonant absorption at surfaces where $\omega = \omega_{ce}$. Given the low collisionality and the ECR surface placed near the rear plate (875 G

IC length	43.7 mm
IC internal diameter	30 mm
Coaxial termination length	46 mm
Coaxial termination length immersed in plasma	43.7 mm
Coaxial termination diameter	6 mm
Max. magnetic coil power per source	1 kW
Total number of turns per source	≈ 1200
ECR MF B_0	875 G
Maximum MF	1480 G
MW frequency	2.45 GHz
Forward MW power per source	50 W
Mass flow rate per source (Kr)	7.5 sccm

Table 4.1: Plasma source characteristics and operational parameters.

at 2.45 GHz), resonant heating is expected to contribute alongside, and often more than collisional absorption.

Figure 4.2 depicts the computed MF strength and streamlines of a single source (single MN, configuration S1) and of the two sources in a cluster configuration with different polarity (MA configuration, DA) and the same polarity (two MNs, configuration DB). inside the IC and in the near plume. Gaussmeter measurements inside of the IC and at several locations in-plane and out-of plane were used to validate this computation. Interestingly, the divergence of the outermost magnetic lines is lower in the DA configuration than in the S1 or DB configurations, at least in the plane of the figure. This suggests that a lower divergence plasma beam may be achieved with the MA topology than with a MN (or two MNs with same polarity).

Krypton has been used as propellant. Each source implements a one-hole gas injector on the upper part of the IC. The gas line is split in the cluster configuration using a Swagelok T-shape connector to feed the two ECR sources.

The TL used to carry MW (Micro Wave) power to the thruster comprises several elements linked by coaxial cables. The 7-16 DIN standard has been used for coaxial connections, as it allows greater power to be transmitted at 2.45 GHz than most of the usual coaxial connector types. MW power is generated by a MR1000D-200ML solid-state MWG (Micro Wave Generator) at 2.45 GHz $\pm$50 MHz. The MWG has a built-in circulator and dummy load, protecting it from reflected waves. Moreover, it allows us to measure the set (P_{set}), forward (P_F) and reflected (P_R) powers in the TL. In all the configurations tested in this work, P_R/P_F was below 1%; assuming that ohmic losses and radiation are small, this means that essentially all the power is delivered to the plasma. A DC-block comprises two C2Ws (Coaxial-to-Waveguide adapters) WR340 separated by a 1 mm gap maintained by ceramic washers. Such a DC block is necessary to keep the IC and CT electrically floating. Near-perfect

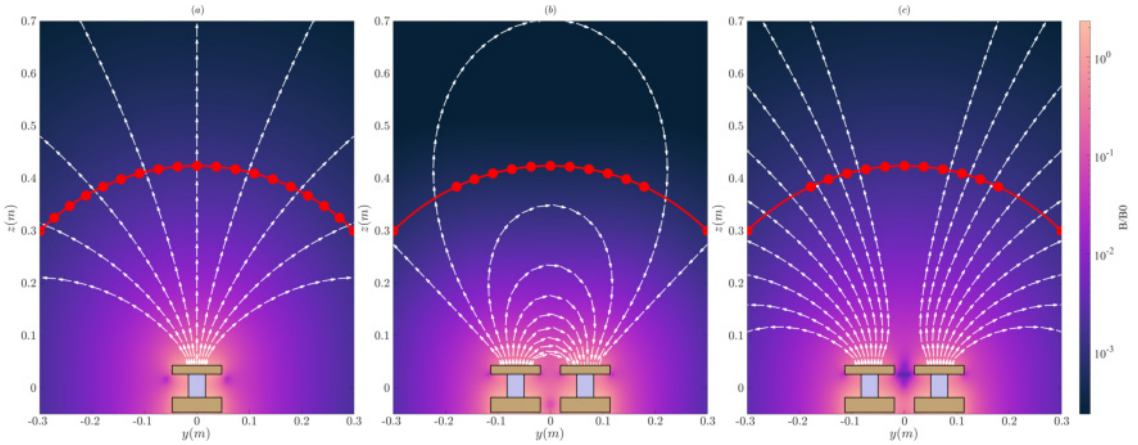

Figure 4.2: Computed MF strength and topology for the single source configuration S1 (left), the MA configuration DA (middle) and the same-polarity configuration DB (right). The axis $z = 0$ corresponds to the rear-end of the IC. MFLs are represented by white arrows, BC electromagnets and MN electromagnets in brown, and the IC in grey. The red line corresponds to the circular path of the RPA with measurement points represented by red circles. The colormap depicts the normalized MF, taking the resonance field as reference $B_0 = 875\,\mathrm{G}$.

transmission of the MW has been measured through the DC block, with leaks under 0.1% of the power. A coaxial three-way splitter divides the forward MW power equally between the two ECRT sources in the cluster configuration.

4.2 Experimental setup

The vacuum chamber at the Laboratory of Space Propulsion at Universidad Carlos III de Madrid [52], [76] is used. It consists of a stainless-steel vessel of 3.5 m in length and a 1.5 m inner diameter, assumed large enough to rule out any wall-proximity effects on the experiment. Three types of pumps are in use: a main dry pump Leyvac LV80 (capacity of $80\,\mathrm{m^3/h}$), two turbomolecular pumps Leybold MAGW2.200iP (capacity of 2000 l/s) and three cryopanels Leyvac 140 T-V (capacity of 37000 l/s for Xenon), yielding an ultimate pressure of 10^{-7} mbar and an order of magnitude for the operational pressure around 10^{-5} mbar for a total mass flow rate between 7 and 15 sccm of Krypton.

Measurements of the plasma exhaust properties have been performed with an Impedance-Semion RPA [77]. The RPA consists of a chassis and collector, preceded by four grids biased to different voltages. The chassis consists of 37 holes of $800\,\mu\mathrm{m}$ in diameter, where the grid holes, aligned with the chassis ones, have an aperture of $20\,\mu\mathrm{m}$ in diameter and a total transmission coefficient of 0.5. The voltage of the second grid is swept from 0 V to 100 V. The first grid is set at the same constant negative voltage as the collector in the $[-150\,;-270]\,\mathrm{V}$ range. The third grid, re-

sponsible for secondary electron repulsion, is set to 30 V lower than the first grid and collector.

In the RPA, the electron-repeller and collector are biased negatively solely to suppress electrons and counter secondary electron emission. The ion energy threshold is set by the second grid bias sweep. While the electron temperature in the plume is expected to be lower than 20 eV, a conservative negative bias (< -150 V) has been set to ensure robust suppression under varying operating conditions such as fast-electron tails without affecting the measured IEDFs (Ion Energy Distribution Functions). This choice is consistent with RPA practice, where the repeller is biased sufficiently negative (often several times the electron temperature) and the discriminator alone defines the cut-off. For completeness, it has been verified that reducing the repeller/collector bias—down to -50 V—does not change the IEDFs shape or the inferred most-probable energy.

The ion current density j is computed from the RPA signal at the null voltage setting using the grids aperture and transmittance. A FC (Faraday Cup)[53] has been used to validate the accuracy of this approach for the estimation of j. The uncertainty Δj is estimated as the standard deviation σ of the RPA signal in the low-voltage (i.e. ion saturation) part of the scan. The IEDF is computed from the derivative of the RPA signal with respect to its potential. The most probable ion energy E_i corresponding to the maximum of the IEDF is used in the discussion; its uncertainty ΔE_i is estimated from the standard deviation σ of the IEDF far from the peak and the second derivative κ of the IEDF curve at the peak (i.e., its curvature), $\Delta E_i = \sqrt{2\sigma/\kappa}$. The RPA has been set on a polar probing arm system to scan the central horizontal plane of the setup, aligned with the axis of symmetry of the assembly and pointing toward the origin at the exit plane of the source(s). Sweeps have been realised in the polar angle α between $\alpha = \pm 50$deg at a fixed distance of 380 mm from the centerpoint at the exit plane of the sources. Figure 4.3 depicts the electrostatic probes installed in front of the cluster exhaust plane.

Experimental characterisation has been carried out for a single source with a traditional MN (configuration S1) and for the dual-source cluster, in the MA configuration (DA) and the same-polarity configuration (DB). At the strength of the applied field B_a, electrons can be assumed to be well-magnetized in the plume region, with a Larmor radius ℓ_e much smaller than the characteristic macroscopic length, $L \simeq 10$ cm. Indeed, for an electron temperature T_e in the neighborhood of 10 eV, $\ell_e/L = O(10^{-3})$. In contrast, krypton ions are essentially unmagnetized, with a dimensionless magnetization parameter [78] $\hat{\Omega}_{i0} = eB_aL/\sqrt{T_e m_i} = O(1)$ inside the source, and $\hat{\Omega}_{i0} \ll 1$ already early in the expansion as the field strength drops. In a traditional MN, as the warm, magnetized electrons expand, they set up an electrostatic potential map that guides and accelerates the unmagnetized ions supersonically [79]; a similar behavior occurs also in in a MA [70]. For completeness, two other configurations, S0 and D0, have been tested, where one or two sources

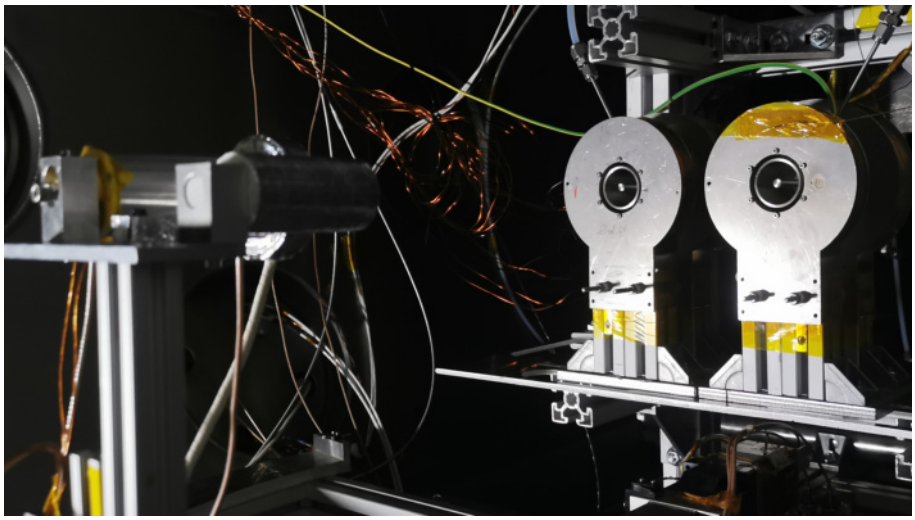

Figure 4.3: Picture of the cluster with electrostatic probes in front. The gas injection can be noticed on top of the sources' ionisation chamber.

were run without applied MF. These configurations are achieved by first igniting the sources with applied field, and then turning off the coils' power supplies, entering a stable operating mode in which plasma is maintained without a MF. Hence, the process that sustains the discharge in the S0 and D0 configurations is not the ECR. When the applied magnetic field is disabled, the discharge is best described as a microwave-sustained, non-resonant plasma. It is maintained through capacitive and collisional mechanisms, with a possible contribution from surface-wave propagation near boundaries, rather than an ECR discharge. Power deposition arises primarily from Capacitive coupling and collisional damping, with additional contributions from sheath heating. Sustenance is facilitated by electrons remaining from the ignition phase.

In all cases, the operating point has been fixed at 7.5 sccm Krypton, with 50 W forward power per source. This study focuses on the DA configuration; the other test cases, in particular S1 and DB, set relevant comparison points. We note that, although the D configurations have twice the mass flow rate than the S ones, the background pressure level remained in the order of magnitude of 10^{-5} mbar during operation in all cases. In the following, we hypothesize that background pressure effects do not distort substantially the results.

4.3 Ion most probable energy and flux

4.3.1 Single source configurations

Figure 4.4 presents the normalized IEDF plots for $\alpha > 0$ in the S1 configuration. The IEDF is single-peaked but strongly skewed, with a significant shoulder at lower

energies and especially at higher angles from the axis. A plausible explanation for this is the presence of a relatively large ionization region, and/or the presence of ionization or charge-exchange collisions outside of the source. We note that a separate low-energy, "background plasma" peak is not found in our results. Ion energies in the range 60–70 eV are compatible with the MN acceleration of an upstream plasma with electron temperature around 10–15 eV, and are comparable to earlier findings in similar devices [41]. The overall IEDF peak energy increases with α while the peak relative magnitude decreases away from the central axis.

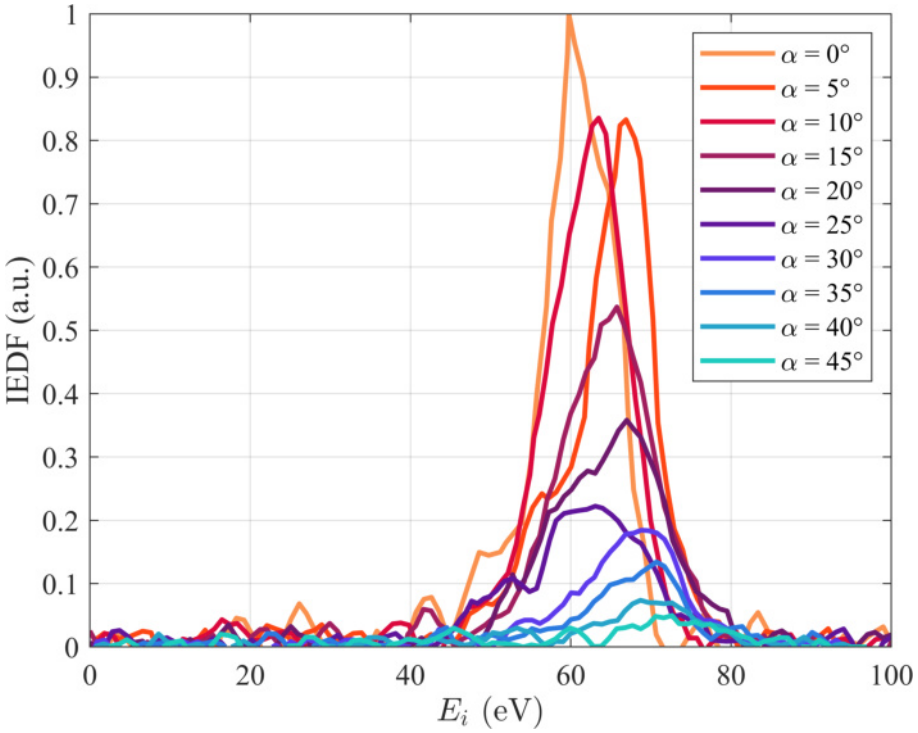

Figure 4.4: IEDFs measured by RPA as a function of the azimuthal angle evolution for the single source S1 configuration. IEDFs have been normalized with the overall maximum value. Conditions of operation: 7.5 sccm Krypton, 50 W, $I_{BC} = 11$ A and $I_{FC} = 8.5$ A. Measurements realised at 380 mm from the exit plane.

The RPA measures the component of the ion velocity normal to its grids. As α varies, the RPA normal can become better aligned with the local ion flow than on-axis, increasing the inferred energy while the local ion density decreases off-axis. In addition, a radial potential structure within the IC—with a higher potential inside the closer to the walls—may yield a larger effective potential difference for off-axis trajectories. Hence, it would reinforce the trend with the 60 eV to 70 eV levels reported for S1 while being compatible with an electron temperature around $\sim 10 - 15$ eV MN acceleration.

Figure 4.5(a) exhibits the ion flux as a function of the polar angle in the S1 configuration used for reference (also for S0). The S1 configuration shows a single-peaked ion flux profile. The single-peaked but asymmetric ion-flux profile in S1 is

attributed to intrinsic source asymmetries and the scan geometry. The single-orifice gas injection located on the upper side of the IC produces a non-uniform neutral and ionization pattern at the exit. Moreover, the RPA scans in fixed orientation toward the source origin and the small differences in the local beam angle (in addition to finite aperture and grid shadowing) modify the effective collection, reinforcing the observed asymmetry.

In the S0, in the absence of an MN to confine the plasma expansion, the ion flux profile is about five times lower and essentially flat. Even though the two configurations differ in this central aspect, the ion most probable energy E_i is comparable on the centerline (around $60 - 65\,\mathrm{eV}$), as it can be observed in Figure 4.5(b).

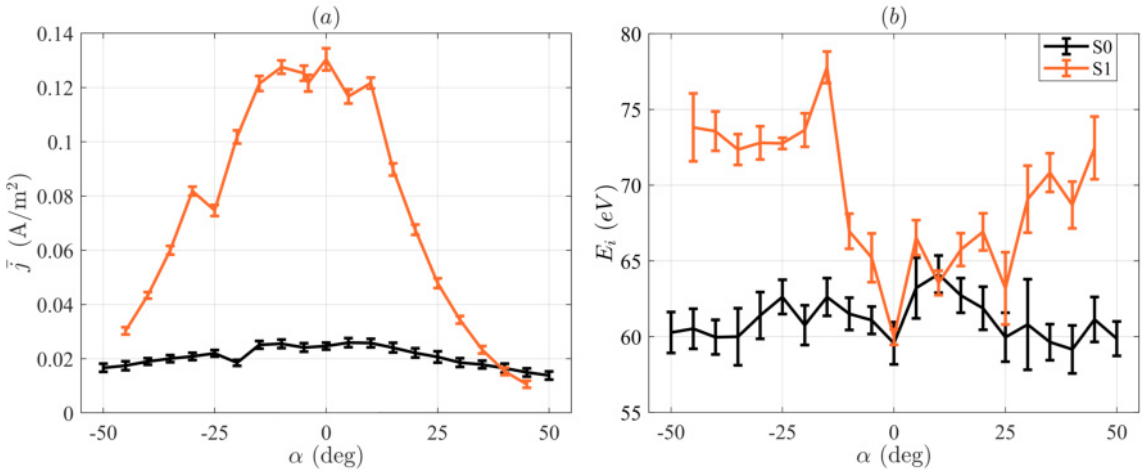

Figure 4.5: Single source (a) ion flux j and (b) most probable energy E_i measured by RPA as a function of the azimuthal angle evolution for S1 and S0. Conditions of operation: 7.5 sccm Krypton, 50 W, $I_{BC} = 11$ A and $I_{FC} = 8.5$ A. Measurements realised at 380 mm from the exit plane.

4.3.2 Cluster configurations

The characterisation of the dual-source cluster took place after that of the single source. Figure 4.6(a) displays the cluster in operation in the DA topology. A plasma arch linking the two sources can be observed. In contrast, diverging plasma beams can be seen in Figure 4.6(b) for the DB configuration.

Figure 4.7 presents the normalized IEDF curves for the the DA configuration. Same comments on the skewness of the distribution as in the S1 configuration apply, although it is apparent that the importance of the low-energy shoulder and the width of each peak are greater in the DA case, which may suggest a larger contribution from lower-energy ions, generated in the proximity of the source exits. The peak energy at all angles is lower than in the S1 case, and increases with α, while the relative magnitude of the IEDF peak plateaus for $5 \leq \alpha \leq 25$deg. Overall, we find

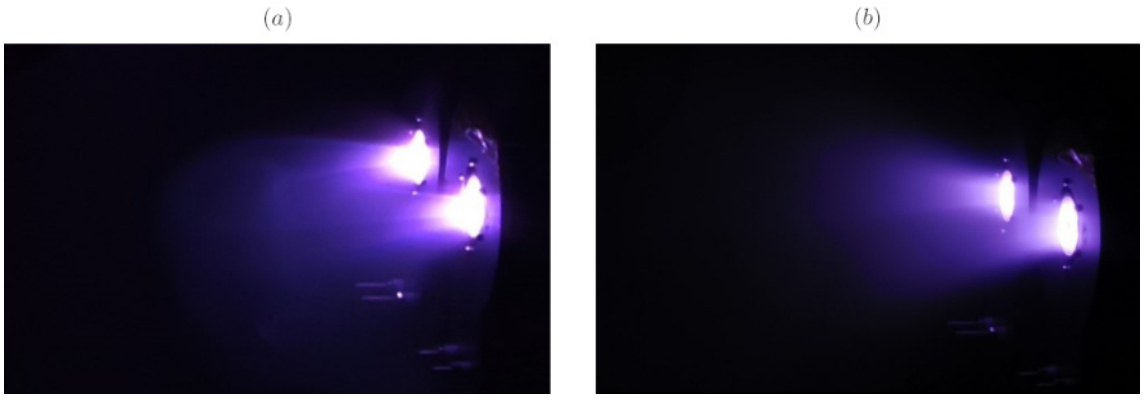

Figure 4.6: Dual-source cluster in operation featuring (a) a MA (DA configuration) and (b) two MNs with the same polarity (DB configuration). Pictures were taken from a lateral window of the vacuum chamber.

that the RPA signal to noise ratio is worse in the dual-source cases than in the single-source cases.

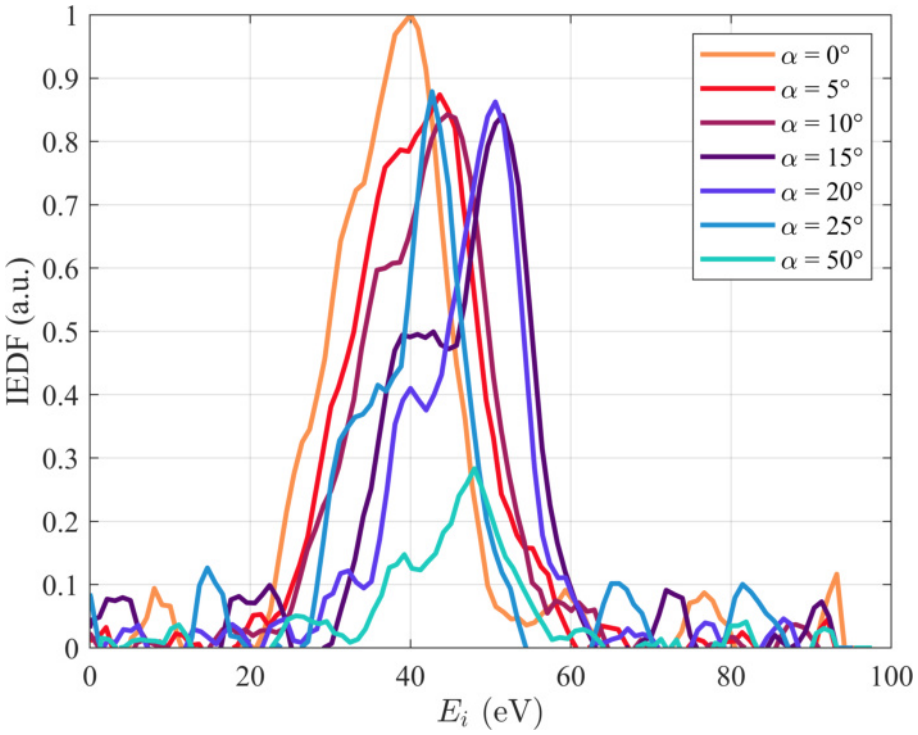

Figure 4.7: IEDFs measured by RPA as a function of the azimuthal angle evolution for the dual-source DA configuration. IEDFs have been normalized with the overall maximum value. Conditions of operation: 15 sccm Krypton in total, 100 W in total, $I_{BC} = 11$ A and $I_{FC} = 8.5$ A. Measurements realised at 380 mm from the exit plane.

Figure 4.8 presents on the other hand the normalized IEDF curves for the the DB configuration. The same comments made on the IEDF curves of the DA configuration can be made on the DB one. The main difference among these two cases

stems from DB having a larger E_i overall, and a more uniform E_i as a function of the polar angle α. The maximum E_i is found at $\alpha = 25$deg. Incidentally, the IEDF signal at the maxium is larger at $\alpha = 20 - 25$deg.

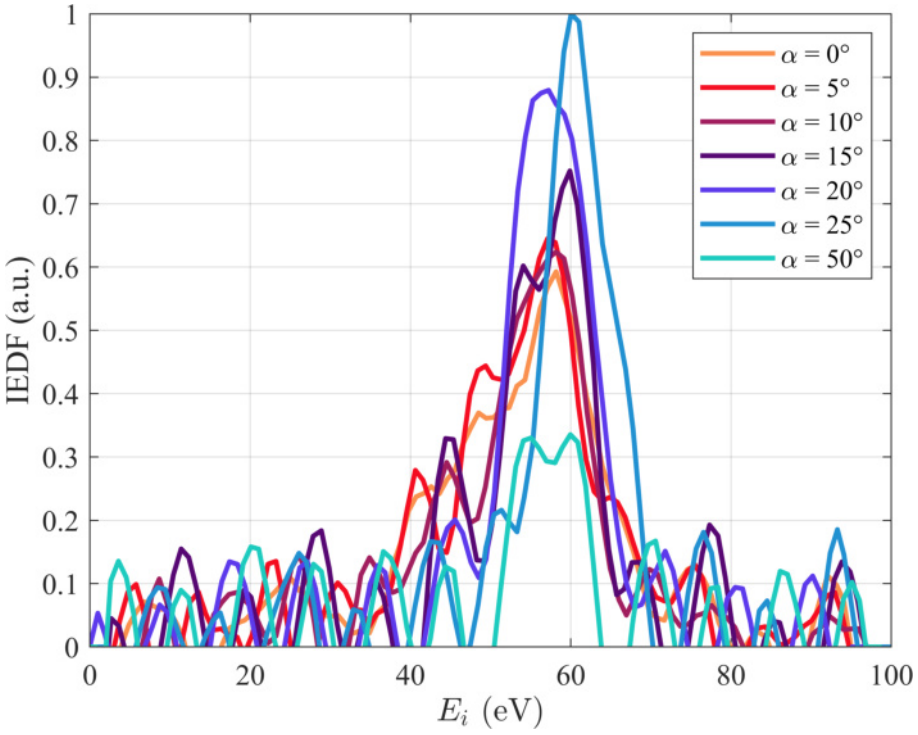

Figure 4.8: IEDFs measured by RPA as a function of the azimuthal angle evolution for the dual-source DB configuration. IEDFs have been normalized with the overall maximum value. Conditions of operation: 15 sccm Krypton in total, 100 W in total, $I_{BC} = 11$ A and $I_{FC} = 8.5$ A. Measurements realised at 380 mm from the exit plane.

Figure 4.9(a) displays the ion current in the dual-source cases. The D0 configuration shows a flat profile of low ion current, revealing the wide plume divergence that takes place in the absence of a guiding MF, as occurred in the S0 configuration of Figure 4.5(a). While a larger value of the ion current may be expected for D0 than for S0 since plasma production has doubled, our results show very similar current levels. This could be due, in part, to the relatively large separation among the sources (130 mm), which means that the two plumes do not fully overlap. It could also be due to the fact that in the two-source configurations the RPA is not aimed at any individual source, but rather, the centerpoint of the setup, meaning that ions enter the RPA at an angle with respect to its normal. Regarding the DB configuration, two minor ion current density peaks appear at ±20deg, which can be attributed to the jets emanating on the two sources and which are guided by their MNs. Interestingly, this angle is lower than that of the magnetic centerline of each MN (±25deg at the measurement location), indicating that the ion streamlines are more straight (i.e. less divergent) than the applied field lines, a hallmark of unmagnetized ion detachment in MNs [80]. Indeed, such ion separation with respect to $\boldsymbol{B}_a$ is expected in individual 3D MNs [81]. Lastly, the beam profile in the DA

configuration is single-peaked and features a larger maximum than DB. Moreover, it displays a faster drop at larger angles than the DB configuration, suggesting that in a cluster of two EPTs (Electrodeless Plasma Thrusters), the MA can offer a lower beam divergence angle than the alternative configuration. Figure 4.9(a) additionally displays the FC measurements of the ion current density in this case, showing good agreement with the RPA-computed j.

Figure 4.9(b) displays E_i for the cluster configurations. The D0 case has E_i averaging at 65.3 eV, while DB has 59.1 eV and DA 45.2 eV.

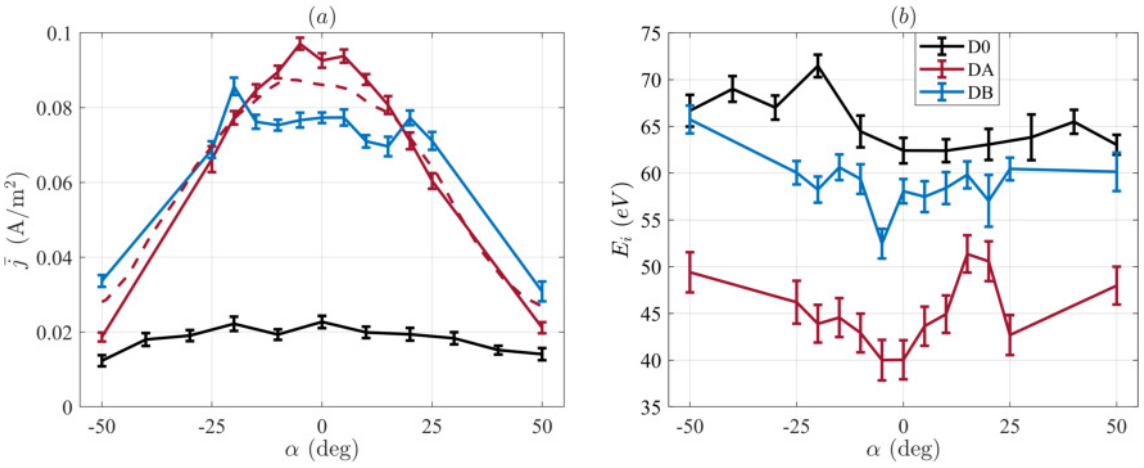

Figure 4.9: Dual-source cluster (a) ion flux j and most probable energy (b) E_i as a function of the azimuthal angle for the DA, DB, and D0 configurations. The red dashed line present in (a) depicts the FC scan for the DA configuration. Conditions of operation: 15 sccm Krypton in total, 100 W in total, $I_{BC} = 11$ A and $I_{FC} = 8.5$ A. Measurements realised at 380 mm from the exit plane.

4.4 Discussion

Both the DA and DB configurations display a lower E_i profile than the single-source, traditional MN case, S1. This could be partially attributed to the lower area expansion ratio undergone by the last magnetic tube, compared to the S1 configuration (cf. panels in Figure 4.2). Nevertheless, we also note that in DA and DB the MF configuration inside each source differs from that of S1, as the coils of one source influence the other, and viceversa, leading to a $\boldsymbol{B}_a$ field that is not axisymmetric inside each source, and is partially tilted to one side (with more B lines intersecting the walls). As a consequence of this the plasma losses to the walls are expected to increase, reducing the device efficiency. The wall temperature profiles would have given a great estimation method of the efficiency difference between the different configurations. However, thermocouples were installed on critical components of the TL, leaving the IC walls without temperature tracking.

Assuming that the most energetic electrons are lost first, this may reduce the value of the electron temperature T_e in the discharge and the plume, for the same power and mass flow rate values. As the ion energy in the plume is proportional to T_e [79], this hypothesis could also explain the lower E_i of DA and DB compared to the S1 configuration.

All in all, it is evident that the MA yields an E_i profile roughly 15 eV below that of DB. Modelling results [70] have shown that ions experience a small electrostatic drag force in the central part of the MA, where the $\boldsymbol{B}_a$ lines are essentially orthogonal to the plasma flow. This electrostatic force is set up by the magnetized electrons interacting with the applied field (whose current is slightly paramagnetic with respect to $\boldsymbol{B}_a$, rather than diamagnetic, in this region, and thus cause a small yet negative magnetic thrust), but is insufficient to completely stop the ions, which overcome the potential and form a free plume beyond. The present experiments align with this conclusion, suggesting that indeed there is a limited deceleration of the ions in the central part of the MA, which could explain the lower energy in the DA case.

The ion current density HWHM (Half Width at Half Maximum), computed in Table 4.2, can be used to estimate the divergence rate of the plasma jet in each configuration, at least in the measurement plane. Measurements are limited to a single RPA sweeping angle in one azimuthal plane at a fixed radius, yielding a 1D profile $j(\alpha)$ rather than a full 2D angular distribution. In such a non-axisymmetric geometry, a unique three-dimensional beam divergence cannot be defined from a single cut. Therefore, the HWHM of $j(\alpha)$ can be considered as a robust indicator of plume spread in the measurement plane and as a basis for comparison across configurations. Classical divergence metrics—such as current-weighted RMS angle or containment half-angles (e.g. 90% current)—require axisymmetry or a 2D angular map, which is impossible with the current setup. Divergence is significant in configurations without any guiding MF (S0, D0), which evidences one of the advantages of using a MF to guide and laterally confine expanding plasmas. Results also indicate that the MA (configuration DA) yields a substantially lower divergence than two repelling MNs (configuration DB), confirming another advantage of clustering EPTs in pairs with opposing polarities. Configuration DA features a larger HWHM value than the single MN of configuration S1. At least in part this is attributed to DA sources being 130 mm apart, comparable to the RPA distance, 380 mm. Hence, it is impossible to compare fairly the divergence angle between the single source and the double source cases at this distance.

We note that figures 4.5 and 4.9 exhibit minor asymmetries between positive and negative angles, to be expected due to the uncertainties linked to the sources manufacturing, alignment and installation, and asymmetries caused by the point gas injection. Nevertheless, the small magnitude of these asymmetries in the cluster configuration does not invalidate our conclusions. Furthermore, it suggests that the

Configuration	j HWHM (deg)
S0	> 50
S1	27 ± 3.5
D0	> 50
DA	33 ± 1.65
DB	43 ± 1.3

Table 4.2: In-plane half-width at half-maximum of the ion current density profiles j, for the single source and dual-source configurations.

distribution of gas and power between the two sources is roughly equal.

4.5 Conclusion

From these results, we conclude positively on the feasibility of the MA topology for accelerating a globally current-free plasma beam from a cluster of two EPTs with zero dipole moment and lower plume divergence than a pair of MNs with the same magnetic polarity. The presence of closed lines in the applied MF does not prevent the formation and acceleration of the plasma beam. However, ion energy drops about 25% with respect to the alternative configuration with two repelling MNs. While other factors such as possible differences in electron temperature T_e among configurations and differing magnetic tube expansion ratios can be invoked to (partially) explain this, it agrees with the ion deceleration previously reported in [70] from simulation results. This deceleration takes place in the central part of the MA where the magnetic lines of the MA are essentially perpendicular to the flow, and where electron currents are paramagnetic with respect to $\boldsymbol{B}_a$. The alternative clustering approach, configuration DB, offers a comparable ion energy to S1 near the axis, but a lower one away from it. Moreover, it features a considerably larger divergence angle and twice the magnetic dipole.

Further research must characterize the region of interaction of the plasma jets coming out of the two sources in configuration DA. Finally, different separation distances and relative tilt angles between the two sources should be investigated to identify optimal configurations for EPT clustering.

Chapter 5

Probe and Laser induced fluorescence measurements in a Magnetic Arch

5.1 ECRC2 architecture and characteristics

5.1.1 ECRC2 motivation

The current chapter—of which a first version was presented in [59]—focuses on the development of the second prototype based on a pair of coaxial electron cyclotron resonance sources with opposing magnetic polarities, labelled ECRC2 (Electron Cyclotron Resonance Cluster 2). The ECRC1 (Electron Cyclotron Resonance Cluster 1), presented in Chapter 4, presented too many limitations to be characterised deeply. Indeed, the latter could be operated for some few minutes at maximum, due to the intense heating of both coils. As it will be detailed in the next subsection, one of the major change operated from the ECRC1 to the ECRC2 lies in the use of permanent magnets to extend the operation time of the prototype.

To begin with, an electrostatic probes experimental campaign has been conducted in the University Carlos III de Madrid to characterize several operation points of the ECRC2. In addition to the latter, a LIF (Laser Induced Fluorescence) experimental campaign has been done to deepen the understanding of the MA (Magnetic Arch) on the ion dynamic. The near-infrared 2D LIF spectroscopy campaign was held in the ICARE laboratory of the CNRS of Orléans, France, during a research stay carried out by the candidate. The main goal of this non-intrusive spectroscopy analysis campaign resides in the determination of the spatially resolved 2D ion velocity vector from the exhaust plane to the far-field plume of both a cluster and a single source. Additionally, the sorting in between ion populations is studied by means of their most probable velocity. Two-dimensional plasma property maps of a cluster of ECRts have never been reported in the literature.

Experiments have been conducted with a single ECR source and a cluster comprising a set of two of the aforementioned sources, mounted in parallel with opposite magnetic polarities. The characteristics of the source can be found in Table 5.1. Their respective centerlines are spaced by 120 mm. Each source can be decomposed into different parts: a MF (Magnetic Field) part composed of permanent magnets and electromagnets, a TL (Transmission Line) transmitting MW (Micro Wave) power to the IC (Ionisation Chamber) and CT (Coaxial Termination) assembly and an independent gas injector for each source. Further sections will focus on these parts.

IC length	20 mm
IC internal diameter	30 mm
CT length immersed in plasma	20 mm
CT diameter	4.5 mm
ECR MF	875 G
Total MW power range	$50 - 200$ W
Total Xenon mass flow rate range	$2 - 20$ sccm

Table 5.1: ECR source characteristics

5.1.2 Magnetic arch topology

Figure 5.1 depicts the cross-sectional top view of the ECRC2 overlapped with the MFLs (Magnetic Field Lines) of interest:

- ***Black dotted lines:*** MFLs generated outside of the IC.
- ***Grey dashed lines:*** MFLs generated on the inner boundary of the IC.
- ***Purple dashed lines:*** MFLs generated between the inner boundary of the IC and the external boundary of the CT.
- ***Purple dashed-dotted lines:*** MFLs generated on the external boundary of the CT.

It should be noted that the ECRC2 has a more closed-line MF (Magnetic Field) distinct from that of ECRC1, since there is a MFL directly joining the external part of each source passing in front of the cluster ehxaust plane in the plasma expansion (i.e. $x = |75|$ mm). As an example, the MFL starting at the equivalent localisation on the ECRC1 passes behind the thruster exhaust plane.

N42 permanent magnets (1) are placed upstream of the source to generate a sufficiently high-intensity MF to enable the ECR phenomenon. The permanent magnets blocks consist of 9 N42 ring magnets with an inner diameter of 49 mm, an outer diameter of 75 mm and a thickness of 10 mm. Even though the N42 grade

is not adapted to thermally challenging environment, it provides a higher intrinsic coercivity than other standard permanent magnets (SmCo, Alnico and FeCrCo). The magnets blocks are decoupled thermally from the cluster assembly to reduce the thermal conduction with the latter. The MNs (Magnetic Nozzles) (2) are responsible for trimming the MF. A constant current of 2 A was used in each coil during the experimental campaigns. Thanks to the N42 permanent magnets and the MNs, the 875 G ECR resonance line is placed a few millimeters away from the ceramic rear plate to spread through the IC[38]. Positioning the resonance line close to the backplate of the source is beneficial as it aligns with regions of higher gas density resulting from the injection geometry[42]. More specifically, enhanced interaction between the plasma and the electromagnetic fields optimizes the efficiency of energy transfer to electrons, thereby increasing the local electron temperature.

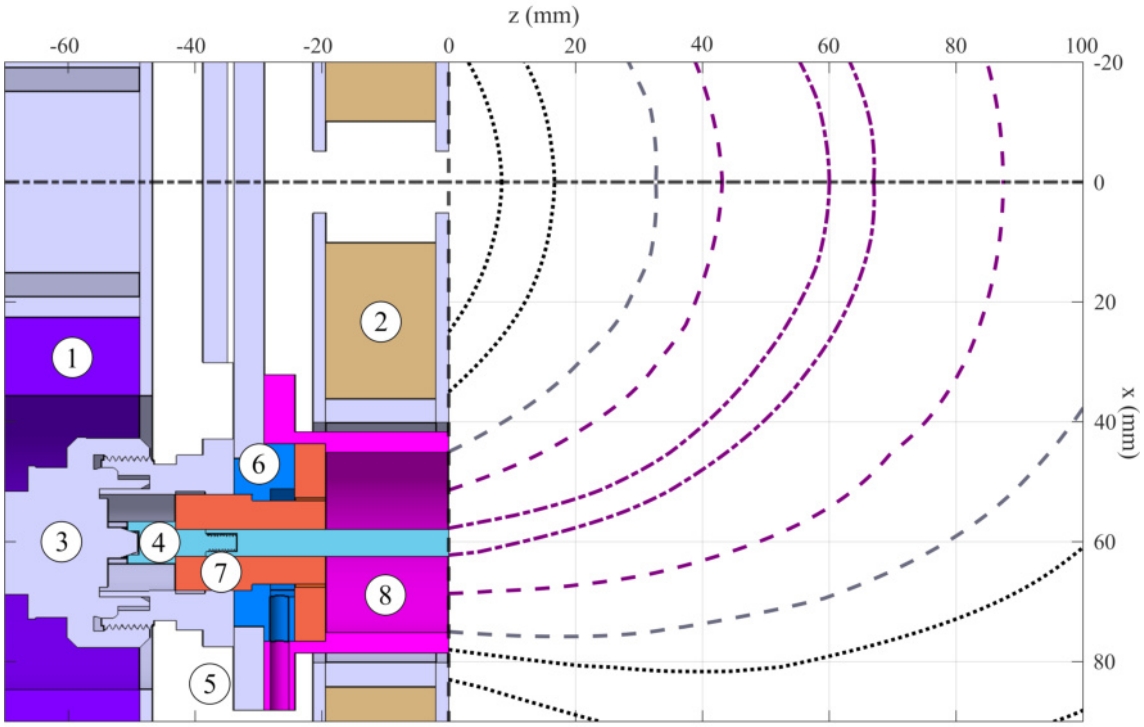

Figure 5.1: Cross-sectional top view of the ECRC2 overlapped with MFLs of interest ($I_{MN} = 2$ A) modelled with Ansys Maxwell. Relevant MFLs are displayed, linking the IC (grey at $x = [45, 75]$ mm and purple at $x = [50, 70]$ mm), the sides of the CT (purple at $x = [57.75, 62.25]$ mm) and MN (black). N42 permanent magnets (1), MN (2), 7-16 DIN receptacle panel (3), CT (4), gas injection (5), prechamber (6), ceramics (7), IC (8).

The ECRC2 replicates as much as possible the magnetic topology of the ECRC1, presented in Chapter 4 with Figure 4.2. As mentioned above, both topologies aim to generate the ECR resonance surface as uniform as possible close to the ceramic rear-plate of the sources. However, it should be noted that the separatrix that divides the MFLs converging between the sources with the arch from the others is more

distant from each source centerline in the ECRC2 than in the ECRC1, as it can be seen from the comparison between Figures 4.2 and 5.1. This difference is mainly due to the presence of permanent magnets in place of the back coil, reducing the flexibility in the magnetic topology.

The simulated MF has been corroborated with Gaussmeter measurements in-plane and out-plane. More details upon the MF measurement method can be found in Section 3.1.2. Measurements have been performed on successive layers from the horizontal plane, distant from each other by 1 cm (from $y = 3\,\text{cm}$ to $y = -10\,\text{cm}$). The Gaussmeter tip has been mounted on an azimuthal translation arm and centered on the plane of symmetry in between the sources. Measurements were taken with a maximum radius of $r = 30\,\text{cm}$ and a step varying from 1 mm close to the exhaust plane to 10 mm far from the latter, from $\theta = -60\text{deg}$ to $\theta = 60\text{deg}$. More details on the characteristics and calibration of the Gaussmeter can be found in Section 3.1.2. Measurements have shown a near-perfect symmetry between the sources, with negligible differences.

5.1.3 Transmission line

The same TL has been used for both the ECRC1 and the ECRC2. It is developed in Section 3.2.1 and shown in Figure 5.2.

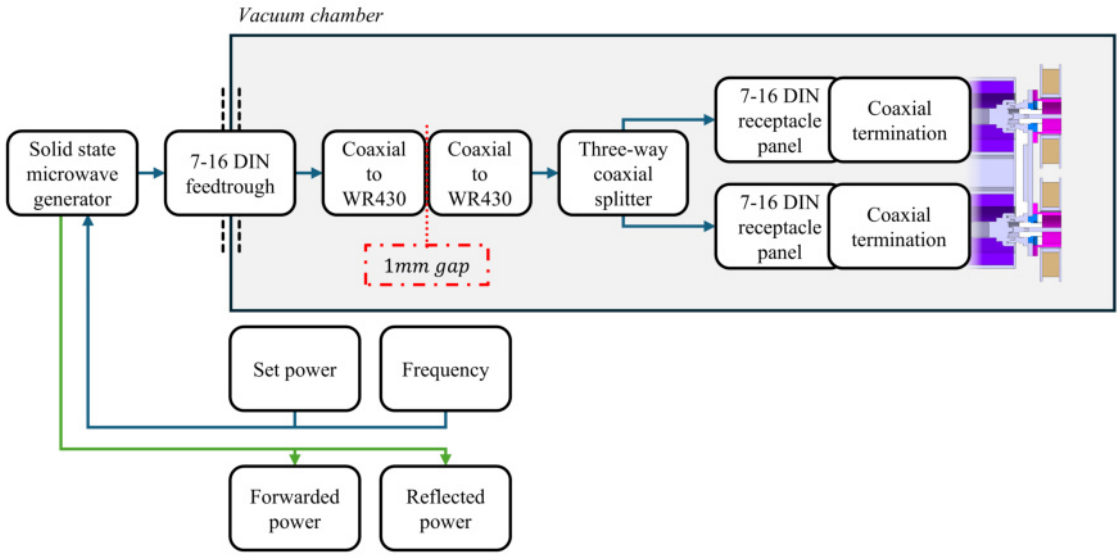

Figure 5.2: TL of the cluster.

5.1.4 Gas injection and ionization chamber

Finally, the plasma source can be decomposed into four distinct parts: gas injection (5), prechamber (6), internal and external ceramics (7), and stainless steel IC (8),

as seen in Figures 5.1 and 5.3. The gas injection (5) is made with a stainless steel pipe ending with a M3 thread to be inserted into the source. The prechamber (6) distributes the propellant equally before it reaches the IC (8) through a 1 mm slit located between the internal and external ceramics (7). The ceramic parts electrically isolate the CT from the IC. This assembly is kept electrically floating thanks to ceramic bearings and PTFE sheets. The origin of the reference frame is defined at the intersection between the ECRC2 exhaust plane ($z = 0$), its vertical symmetry plane ($x = 0$), and the horizontal plane ($y = 0$).

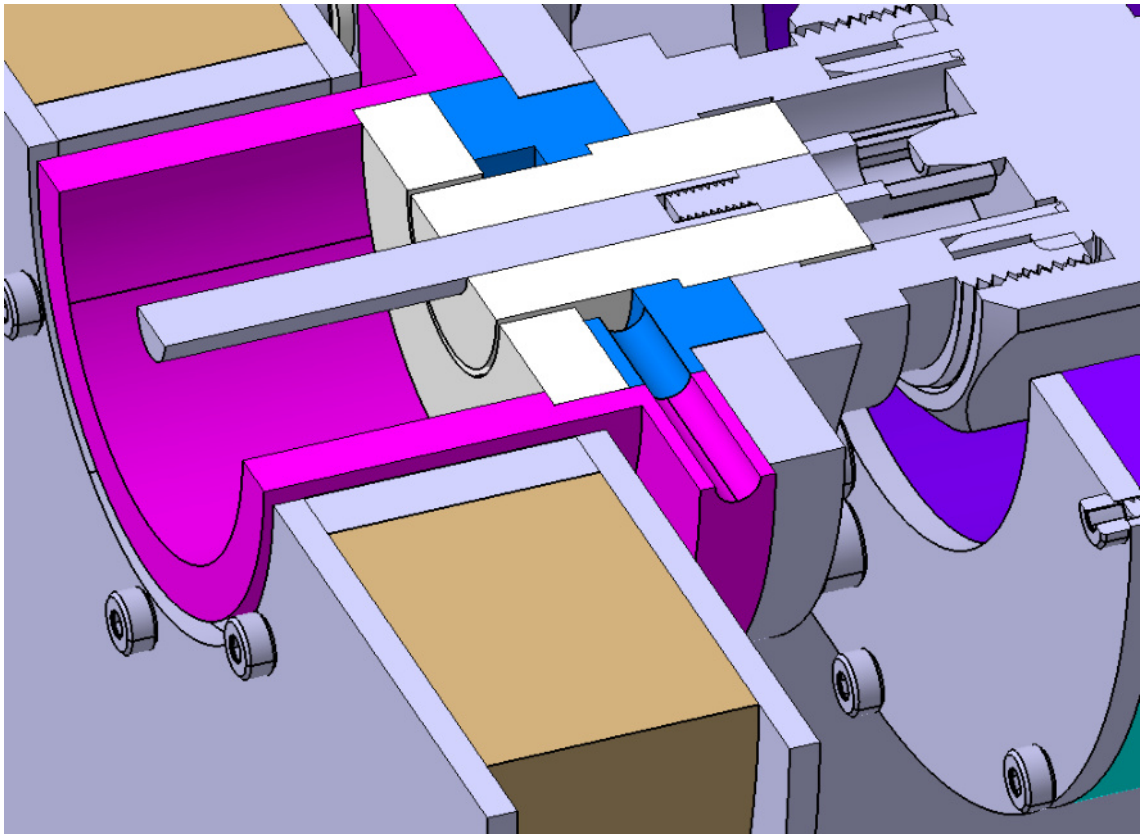

Figure 5.3: Sectional view of the CAD of one source. The IC is in pink, the blue part being an intermediary part in which the gas injection tube will be threaded.

5.1.5 ECRC2 in operation

Figure 5.4 shows the ECRC2 cluster operating in the ICARE EPIC-2 vacuum chamber. A 20 sccm Xenon mass flow rate has been set for each source. The naked-eye observation of the plume is not purely symmetric about the (xz) plane. Indeed, a small fraction of the plasma appears to deviate to the upper side (i.e. in the y direction). The visibility of the fraction seems to increase along with the mass flow rate. This unexpected feature remained unaltered regardless of attempts to correct it: sources have swapped one with another, N42 magnets have been rotated and flipped, y offset has been applied in between the permanent magnets and the

sources. This minor asymmetry is considered acceptable for the purpose of this work, and its study is left out for future works.

Figure 5.4: ECRC2 in operation in EPIC-2 vacuum chamber, ICARE Laboratory, Orléans, France. Conditions of operation: $\dot{m}_{Xe,total} = 40\,\text{sccm}$, $P_{MW,total} = 100\,\text{W}$, $I_{MN} = 2\,\text{A}$. The shift between the plasma beam and the CT on the right-side source is due to misalignment.

5.2 Plume characterisation using electrostatic probes

5.2.1 Electrostatic probes

Electrostatic probe setup

As aforementioned, electrostatic probes measurements have been conducted in the Laboratory of Space Propulsion of Universidad Carlos III de Madrid, Leganés, Spain. More details about the facility can be found in previous works [51], [58], [82]. The mass flow rate range used in the electrostatic probe measurements is 1 sccm to 10 sccm of Xenon per source. Hence, the total mass flow rate injected in the vacuum chamber lies between 2 sccm to 20 sccm. With this mass flow rate range, the vacuum

chamber pressure remains in the $[2.5 \times 10^{-6} - 2.5 \times 10^{-5}]$ mbar range. A single bottle of Xenon is linked to a Bronkhorst EL-FLOW Select Xenon calibrated mass flow controller, with an accuracy of 0.1 sccm and a maximum mass flow rate of 100 sccm. The gas feeding line is split just before the thruster by a Swagelok T gas-splitter. The accuracy of the gas distribution between the sources has not been characterised with the latter. As it will be detailed, two distinct mass flow controllers have been used in the subsequent LIF experimental campaign in order to improve the gas distribution accuracy. Finally, the distance between the ECRC2 exhaust plane and the end of the vacuum chamber measured at 2.5 m. This distance ensures a lower interaction between the plasma and the walls of the vacuum chamber. The MW power generated by the MWG (Micro Wave Generator) has been set from 50 W to 200 W.

Langmuir Probe

To begin with, the LP (Langmuir Probe) has an exposed tip of 7 mm, with a diameter of 0.25 mm[57] . IV curves are obtained by sweeping the voltage applied to the LP and measuring the collected current. Raw data is processed following Lobbia et al. [83] recommended practice. The floating potential V_f, the plasma potential ϕ, the electron temperature T_e and density n_e and the ion density n_i are computed from the IV curves. V_f is measured where the probe current corresponds to 0 A. ϕ corresponds to the bias of the maximum of the first derivative of the smoothed electron current $dI_{e,smoothed}/dV_B$. The electron temperature T_e is determined by the slope method. The natural logarithm of the electron current is plotted against the probe bias. A least squares estimate is made on the linear region between V_f and ϕ. T_e corresponds to the inverse of the least-squares estimation slope. The electron density n_e is computed with the probe radius r_p and T_e at the electron saturation current, $I_{e,sat}$, defined at ϕ. The ion density n_i is calculated with respect to r_p to Debye length λ_D ratio and refined through iterations of the ion saturation current $I_{i,sat}$ until convergence.

The plasma is sustained at 2.45 GHz, therefore GHz-range oscillations can couple capacitively/inductively into the probe circuit and distort the I–V characteristic. This coupling tends to induce an overestimation of the apparent electron current and bias the inferred ϕ and T_e. The LP is connected coaxially with with good MW shielding, so that the outer conductor screens MW pickup. Still, some active compensation systems could have been used in order to reduce the pollution of the GHz-range oscillations on the LP measurements. Some of these active compensation systems have been investigated, such as an active compensation auxiliary electrode placed close to the LP. Using a capacitor/coil network, this electrode would pick up the same noise as the LP, without the plasma current, to be subtracted to the IV curve obtained with the latter. A quarter-wave choke or a low-pass filter

would have helped preventing MW pickup from propagating into the measurement electronics. Nevertheless, none of the active compensation system aforementioned was implemented in this setup due to the time constraint and constraints of the scanning arm and in-vacuum cabling. Consequently, ϕ and T_e extracted from the LP should be regarded as indicative and used primarily to assess relative trends versus z, P_{MW}, and $\dot{m}_{Xe}$. Absolute density from electron saturation is further unreliable in a magnetized, flowing plume because electron collection is anisotropic and the probe perturbs the sheath. This is consistent with the observed n_e-n_i mismatch.

The Druyvesteyn EEDF (Electron Energy Distribution Function) method would have been a more accurate method to determine n_e. However, it requires the use of the second derivative of the electron current in the retarding region. In the current the I–V curve is too distorted and noisy, hence the second derivative becomes extremely sensitive and yields non-physical EEDFs without strong compensation. Moreover, in a magnetized expanding plume the standard planar-sheath, isotropic-electron assumptions are not well satisfied. In the simple n_e estimate itself presents inconsistencies as aforementioned—n_e-n_i. For these reasons, the LP-derived n_e has to be considered to be indicative only and other diagnostics (FC,RPA,LIF) should be considered more accurate for quantitative plume characterization.

Faraday Cup and Retarding Potential Analyser

A FC (Faraday Cup) with a single aperture with a diameter of 10 mm has been used. The current density is obtained by dividing the current collected by the collection area (i.e. 70 mm^2). The FC has been detailed in previous works, such as Wijnen[57] .

A RPA (Retarding Potential Analyser)[84], used with a control unit both from Impedans Ltd., has been used to determine the ion most probable energy at points of interest. The same RPA setup has been used in Chapter 4. The points of interest have been defined thanks to the FC data, and consist of plateaux, peaks or troughs in ion current density. The RPA has been described in Section 4.2. The ion most probable energy E_i can be derived from the IV curves. However, without measuring the local ϕ at each measurement, it is impossible to make a correct estimation of the real ion kinetic energy.

One at a time, the FC and RPA have been mounted on an azimuthal translation arm. It has been centered on the plane of symmetry in between the sources, with its origin being defined as the cluster one. It allows to move the probes from $\alpha = -90$deg to $\alpha = 90$deg with a step of 1deg. Moreover, the probes can be moved in the radial direction up to 400 mm, with a minimal step of 0.3 mm. Both probes were aligned with the arm axis. Measurements have been performed at 280 mm for the FC and 380 mm for the RPA. The LP has been mounted on the same translation azimuthal translation arm, set at $\alpha = 0$deg and swept from 50 mm to 300 mm with a step in the $25 - 50$ mm range.

5.2.2 Electrostatic probe data

Langmuir probe measurements

Three operation points have been studied with the LP: $\dot{m}_{Xe,total} = 5\,\text{sccm}$ with $P_{MW,total} = 50\,\text{W}$, $\dot{m}_{Xe,total} = 5\,\text{sccm}$ with $P_{MW,total} = 100\,\text{W}$ and $\dot{m}_{Xe,total} = 10\,\text{sccm}$ with $P_{MW,total} = 100\,\text{W}$. Measurements have been taken along the axis corresponding to the intersection between the horizontal plane and the cluster's symmetry plane—i.e. (yz) plane.

- **Plasma density**

At 50 mm, the ion density shown in Figure 5.5 is on the order of $10^{15}\,\text{m}^{-3}$ for the operation points with $\dot{m}_{Xe,total} = 5\,\text{sccm}$ and $10^{16}\,\text{m}^{-3}$ for $\dot{m}_{Xe,total} = 10\,\text{sccm}$. An increase in MW power from $P_{MW,total} = 50\,\text{W}$ to $P_{MW,total} = 100\,\text{W}$ at a fixed flow rate of $\dot{m}_{Xe,total} = 5\,\text{sccm}$ results in a slight increase in ion density for $z > 50\,\text{mm}$. Moreover, increasing the mass flow rate from $\dot{m}_{Xe,total} = 5\,\text{sccm}$ to $\dot{m}_{Xe,total} = 10\,\text{sccm}$ leads to an increase in ion density. The ion density remains low compared to similar thrusters [52], [85] . Still, it should be reminded that the measurements have been made on the cluster symmetry plane 60 mm away from both sources' centerlines.

The electron density n_e is shown in Figure 5.5. At 50 mm, it is on the order of magntitude of $10^{15}\,\text{m}^{-3}$ for all operation points and decays to $10^{14}\,\text{m}^{-3}$ in the far field. A higher density can be seen for $P_{MW,total} = 100\,\text{W}$ compared to $P_{MW,total} = 50\,\text{W}$ at $\dot{m}_{Xe,total} = 5\,\text{sccm}$. This behaviour is logical with a higher MW power. Increasing the mass flow rate from $\dot{m}_{Xe,total} = 5\,\text{sccm}$ to $\dot{m}_{Xe,total} = 10\,\text{sccm}$ results in a higher and more sustained electron density. The electron density evolution closely follows that of the ion density, even though the latter is close to one order of magnitude higher. Hence, it presents evidence of the inadequacy of the basic LP data model in the present magnetized plasma with ion flow as well as the perturbative nature of the LP. Moreover, it is in line with previous experiences in the University Carlos III de Madrid EP2 group[52].

Absolute n_e from the electron-saturation branch is highly uncertain in the microwave polluted plume. At $z = 50\,\text{mm}$, $T_e \sim 10\,\text{eV}$ and $n_e \sim 10^{15}{-}10^{16}\,\text{m}^{-3}$ give $\lambda_D \approx 0.74{-}0.24\,\text{mm}$ and $\lambda_D/r_p \approx 6{-}2$ for $r_p = 0.125\,\text{mm}$. Together with the distortion of the I–V curve and the anisotropic electron collection, this yields a factor-2 uncertainty on absolute n_e at $z = 50\,\text{mm}$. This uncertainty increases downstream, consistently with the observed n_e-n_i mismatch.

The differences between n_i and n_e increase along with the distance from the origin. Still, they follow a similar decreasing trend. As the measurements are performed on the cluster symmetry plane, the plasma density is expected to increase

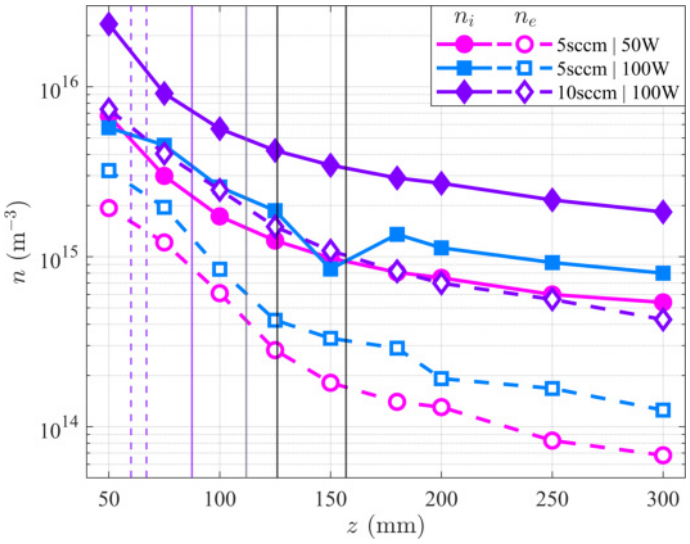

Figure 5.5: Ion density n_i (solid line) and electron density n_e (dashed line) measured with a LP along the cluster symmetry plane, $I_{MN} = 2\,\text{A}$. Vertical lines corresponds to MFLs of interest. Operating points: $\dot{m}_{Xe,total} = 5\,\text{sccm}$, $P_{MW,total} = 50\,\text{W}$; $\dot{m}_{Xe,total} = 5\,\text{sccm}$, $P_{MW,total} = 100\,\text{W}$; $\dot{m}_{Xe,total} = 10\,\text{sccm}$, $P_{MW,total} = 100\,\text{W}$.

before reaching a maximum near the inner boundary of the plasma tube before constantly decreasing. Still, the plasma density follows a decreasing trend from 50 mm. Hence, the peak in density does not correspond to the MFLs joining the sources central connectors.

- **Electron temperature**

Figure 5.6 depicts the electron temperature. A sudden drop to about 1/3 of the temperature occurs, regardless of the operation point, from 50 mm to 100 mm. Indeed, for the 5 sccm with 100 W operation point, a maximum electron temperature of nearly 15 eV drops to three times less at 5 eV. The MFL closing the external part of both sources is localised at nearly 112 mm, as shown by the grey vertical line. However, electron cooling could also take place in the cluster symmetry plane, along with losses of energy due to ionization, collision, etc. Nevertheless, electrons present temperatures in a range similar to ones found in other ECRTs (Electron Cyclotron Resonance Thrusters) [52], [85].

- **Electron cooling rate**

The polytropic coefficient[52], [85]–[92] γ is determined in Equation 5.1. Figure 5.7 shows the fitting of the polytropic coefficient for different operating points through the MA expansion. Each operation point fitting can be divided into two regions of interest, with the exception of the measurement taken at $z = 50\,\text{mm}$. Indeed, this point is too far in the plasma plume and in the closed-line magnetic

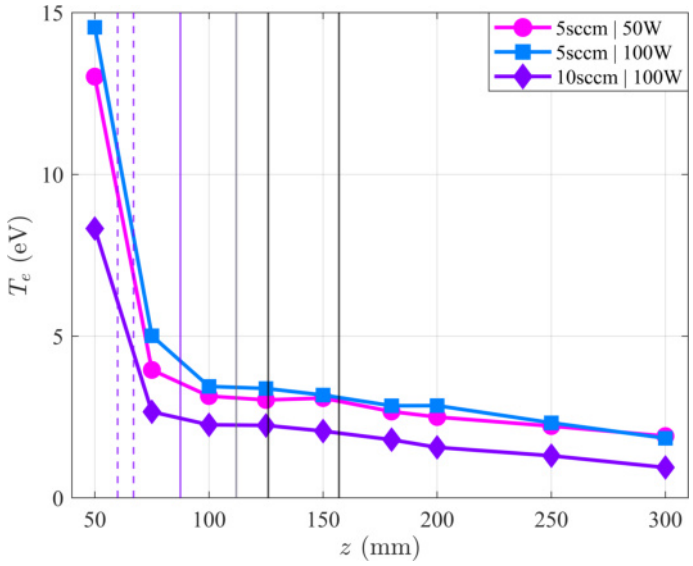

Figure 5.6: Electron temperature T_e measured with a LP along the cluster symmetry plane, $I_{MN} = 2\,\text{A}$. Vertical lines corresponds to MFLs of interest. Operating points: $\dot{m}_{Xe,total} = 5\,\text{sccm}$, $P_{MW,total} = 50\,\text{W}$; $\dot{m}_{Xe,total} = 5\,\text{sccm}$, $P_{MW,total} = 100\,\text{W}$; $\dot{m}_{Xe,total} = 10\,\text{sccm}$, $P_{MW,total} = 100\,\text{W}$.

arch to be considered in the electron cooling rate analysis. As presented in Table 5.2, a low near-isothermal γ (i.e. $\gamma \approx 1.2$) is determined for points measured in the $75\,\text{mm} \leq z \leq 150\,\text{mm}$ range (dash-dot lines) in region (1). Moreover, a high γ region is found in the $150\,\text{mm} \leq z \leq 300\,\text{mm}$ range in region (2) (dashed lines).

$$\frac{T_e}{n_e^{\gamma-1}} = \frac{T_{e0}}{n_{e0}^{\gamma-1}} = Const. \tag{5.1}$$

Region (1) sees the MFL joining the external boundary of the CT close to $z = 75\,\text{mm}$ and the MFL generated at the inner boundary of the MN at $z = 157\,\text{mm}$. In this range a polytropic coefficient of $\gamma \approx 1.2$ is present. It implies an isothermal behavior, which may reflect an equilibrium-like state along the MFLs due to magnetic confinement. Region (2) sees an average polytropic coefficient around 1.6, with a collisionless expansion where the electron dynamics become kinetic and adiabatic, consistent with an EVDF that departs from Maxwellian and a breakdown of Boltzmann equilibrium. In this range, the MFLs are past the separatrix that divides the MFLs converging between the sources with the arch from the others, and their confinement gradually worsens. Moreover, the plasma becomes less collisional.

To summarize, the variation of the polytropic coefficient depicts the transition between two distinct regions: isothermal electrons on the outer boundary of the MA, weakly collisional plasma and adiabatic behavior in the far field where MFLs progressively opens.

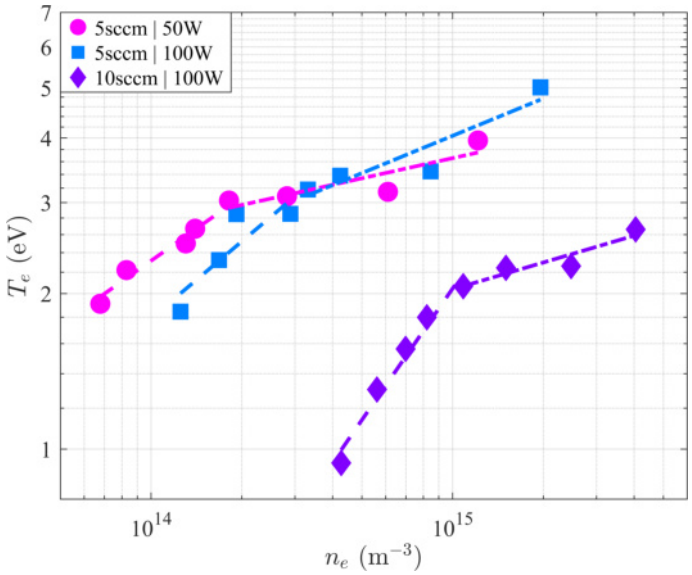

Figure 5.7: Polytropic coefficient γ fitting measured with a LP along the cluster symmetry plane, $I_{MN} = 2$ A. Operating points: $\dot{m}_{Xe,total} = 5$ sccm, $P_{MW,total} = 50$ W ; $\dot{m}_{Xe,total} = 5$ sccm, $P_{MW,total} = 100$ W ; $\dot{m}_{Xe,total} = 10$ sccm, $P_{MW,total} = 100$ W.

γ	(1) $75 \leq z \leq 150$	(2) $150 \leq z \leq 300$
5 sccm | 50 W	1.12	1.43
5 sccm | 100 W	1.24	1.5
10 sccm | 100 W	1.17	1.84

Table 5.2: Polytropic coefficient γ fitting through different regions of the MA.

- **Plasma potential**

As shown in Figure 5.8, the total potential drop is relatively low compared to previous ECRT works [52], [85], [93], with a maximum of 16 V measured for $\dot{m}_{Xe,total} = 5$ sccm with $P_{MW,total} = 100$ W. The latter presents the highest plasma potential of the three. A steep drop is observed within the 50 mm and 150 mm, suggesting the presence of a significant axial electric field that likely contributes to ion acceleration. Beyond 150 mm, the plasma potential decay slows down. It stabilizes by 200 mm, indicating that the plasma approaches an electrostatic equilibrium state.

The plasma potential is influenced by both MW power and mass flow rate. An increase in power from $P_{MW,total} = 50$ W to $P_{MW,total} = 100$ W—at $\dot{m}_{Xe,total} = 5$ sccm—results in a higher plasma potential fall. As aforementioned, this trend is expected as higher power enhances electron heating, leading to an increase in electron energy and thus a higher potential. However, the overall rate of plasma potential decay remains similar through the operation points. It could be concluded that power primarily affects the initial plasma characteristics rather than fundamentally altering the expansion dynamics. Increasing the mass flow rate from $\dot{m}_{Xe,total} = 5$ sccm

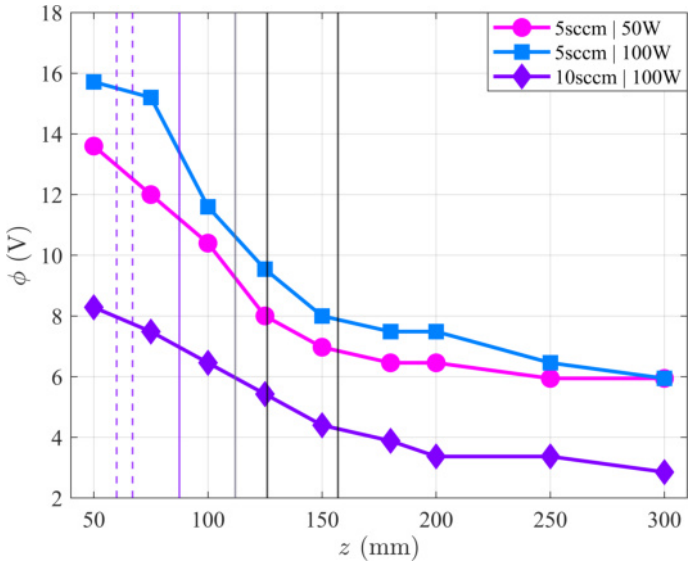

Figure 5.8: Plasma potential ϕ measured with a LP along the cluster symmetry plane, $I_{MN} = 2\,\text{A}$. Vertical lines corresponds to MFLs of interest. Operating points: $\dot{m}_{Xe,total} = 5\,\text{sccm}$, $P_{MW,total} = 50\,\text{W}$; $\dot{m}_{Xe,total} = 5\,\text{sccm}$, $P_{MW,total} = 100\,\text{W}$; $\dot{m}_{Xe,total} = 10\,\text{sccm}$, $P_{MW,total} = 100\,\text{W}$.

to $\dot{m}_{Xe,total} = 10\,\text{sccm}$ leads to a lower plasma potential. This effect can be attributed to the enhanced collisionality through the arch which reduces the electron temperature, according to Figure 5.6. Thus, it lowers the overall plasma potential. Moreover, the reduced potential gradient indicates that a higher neutral gas density leads to a more uniform charge distribution, decreasing the effective axial electric field and thus the potential for ion acceleration.

- **Floating potential**

Figure 5.9 depicts the floating potential V_f. At 50 mm, the floating potential is negative, reaching approximately $-87\,\text{V}$ for 5 sccm and 100 W. Beyond 150 mm, the floating potential stabilizes between $-10\,\text{V}$ and $-5\,\text{V}$ in all tested conditions. Increasing the power from 50 W to 100 W results in a more negative floating potential at 50 mm, a direct consequence of a higher population of energetic electrons. However, as the plasma expands, this effect diminishes because of electron cooling and increased interaction with background neutrals. Moreover, increasing the mass flow rate from 5 sccm to 10 sccm leads to a less negative floating potential, most likely due to lower electron temperature. V_f as also been computed thanks to ϕ and T_e, with a difference going up to 18 V for 100 W and 5 sccm at 50 mm. Close to the source, the largely oscillating IV curves due to the MW changing impedance of the electrons could explain the differences between V_f and ϕ.

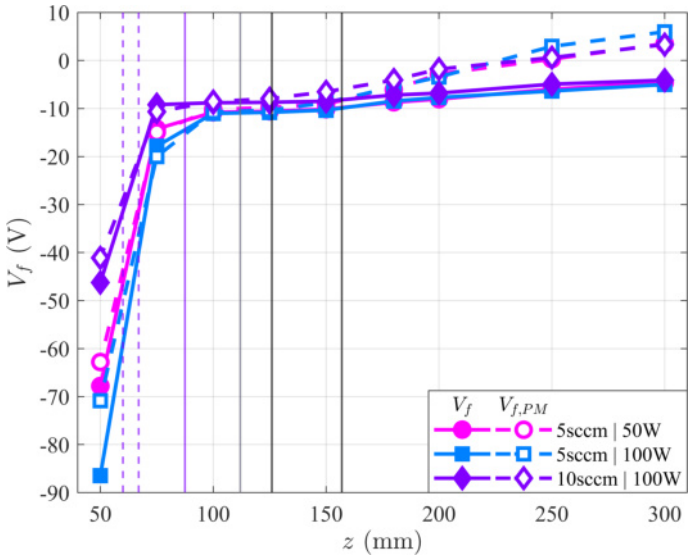

Figure 5.9: Floating potential V_f measured with a LP along the cluster symmetry plane, $I_{MN} = 2\,\text{A}$. $V_{f,PM}$ correspond to the estimation of V_f using the potential method. Vertical lines corresponds to MFLs of interest. Operating points: $\dot{m}_{Xe,total} = 5\,\text{sccm}$, $P_{MW,total} = 50\,\text{W}$; $\dot{m}_{Xe,total} = 5\,\text{sccm}$, $P_{MW,total} = 100\,\text{W}$; $\dot{m}_{Xe,total} = 10\,\text{sccm}$, $P_{MW,total} = 100\,\text{W}$.

Farady cup measurements

Figure 5.10 depicts the current density measured by the FC at multiple MW power for different mass flow rates. First, the current density increases along with the mass flow rate and the MW power. It is to be noted that the peaks on both sides of the symmetry plane are of higher amplitude than the one localised at 0deg for a mass flow rate of 5 sccm in Figure 5.10(a). Figure 5.10(b) shows the current density for a mass flow rate of 10 sccm. A peak with an amplitude close to the side peaks is present at 0deg. This effect is more noticeable in Figures 5.10(c) and 5.10(d), with respectively 15 sccm and 20 sccm of Xenon. This phenomenon is not witnessed at low mass flow rate, possibly due to a lower neutral background density associated to a higher utilisation efficiency linked with the increase of the MW power to mass flow rate ratio. Some asymmetries in terms of current density can be noticed, regardless of the operation point. Their origins could be varied: e.g. misalignment of the elements in the ionization chamber, disequilibrium in the mass flow rate distribution between the sources, mismatched TL impedance after the splitter and difference in plasma impedance in each source.

It is to be pointed out that the FC is not pointing exactly to the ion flow coming from the source. Indeed, it points out to the origin defined at the crossing point between the exhaust plane and the symmetry plane. Hence, these measurements have to be taken with consideration as some ion current might be missing as per its directionality. Moreover, the cluster cannot be approximated as an axisymmet-

ric source, hence the thrust and efficiencies estimations obtained by the current density[52] would be far from realistic.

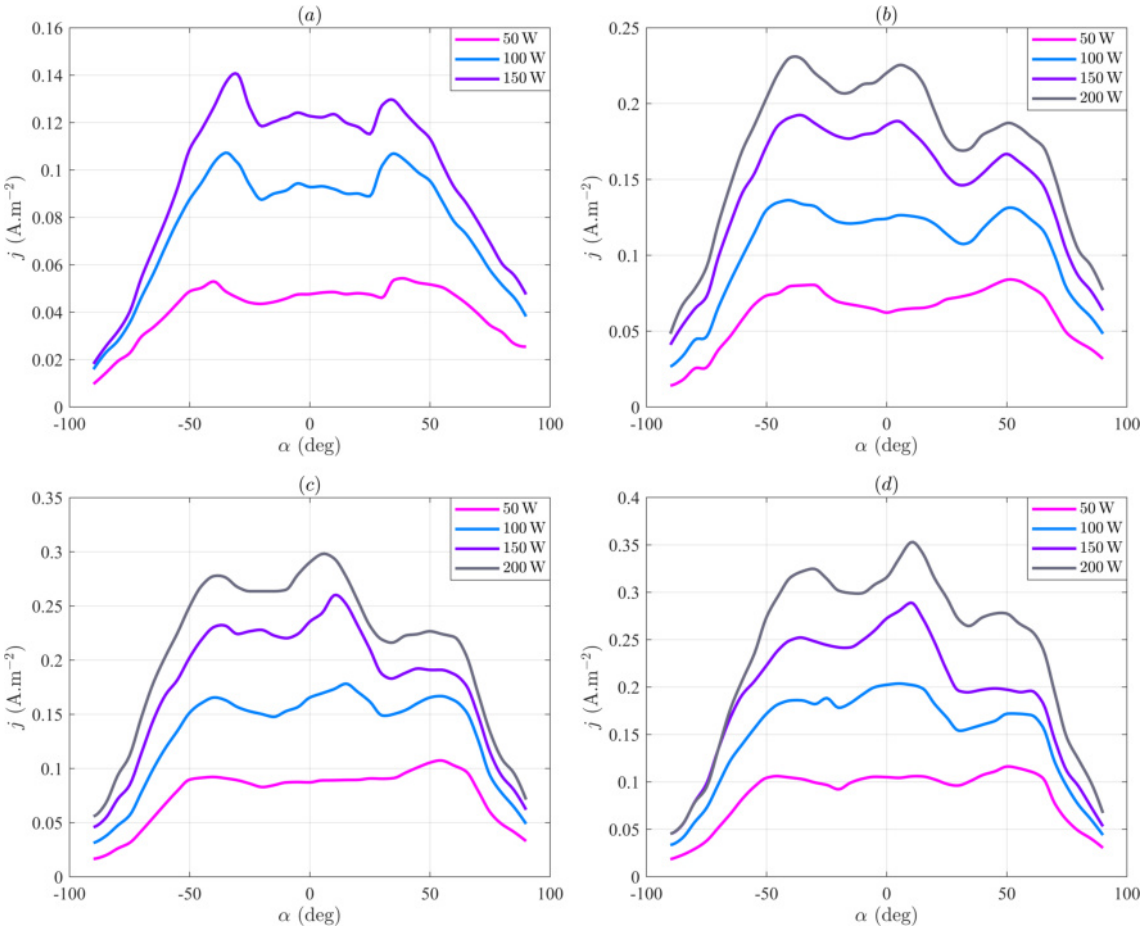

Figure 5.10: Current density j measurements done with a FC in a power range from $P_{MW,total} = 50\,\text{W}$ to $P_{MW,total} = 200\,\text{W}$. 2 A is set on each MN. Considering the accuracy of current measurements and probe aperture diameter, the error on the measurement of j is estimated to be below 2%. (a) $\dot{m}_{Xe,total} = 5\,\text{sccm}$, (b) $\dot{m}_{Xe,total} = 10\,\text{sccm}$, (c) $\dot{m}_{Xe,total} = 15\,\text{sccm}$, (d) $\dot{m}_{Xe,total} = 20\,\text{sccm}$.

Retarding potential analyser measurements

RPA measurements are presented in Figure 5.11. As detailed in Section 5.2.1, these measurements have been performed at points of interest defined thanks to FC data (such as plateaus, peaks or troughs). Mass flow rates vary from 5 sccm to 20 sccm, with a power range between 50 W to 200 W. Figure 5.11(a) focuses on a mass flow rate of 5 sccm. Most probable ion energy profiles are quite constant for each power, from an average of 27 eV for 50 W to 60 eV for 200 W. The same average energy can be found for half the power (100 W) whilst the mass flow rate has doubled (10 sccm) in Figure 5.11(b). For this mass flow rate, average ion energies appear to represent half of the ones determined for 5 sccm. This trend continues from 10 sccm

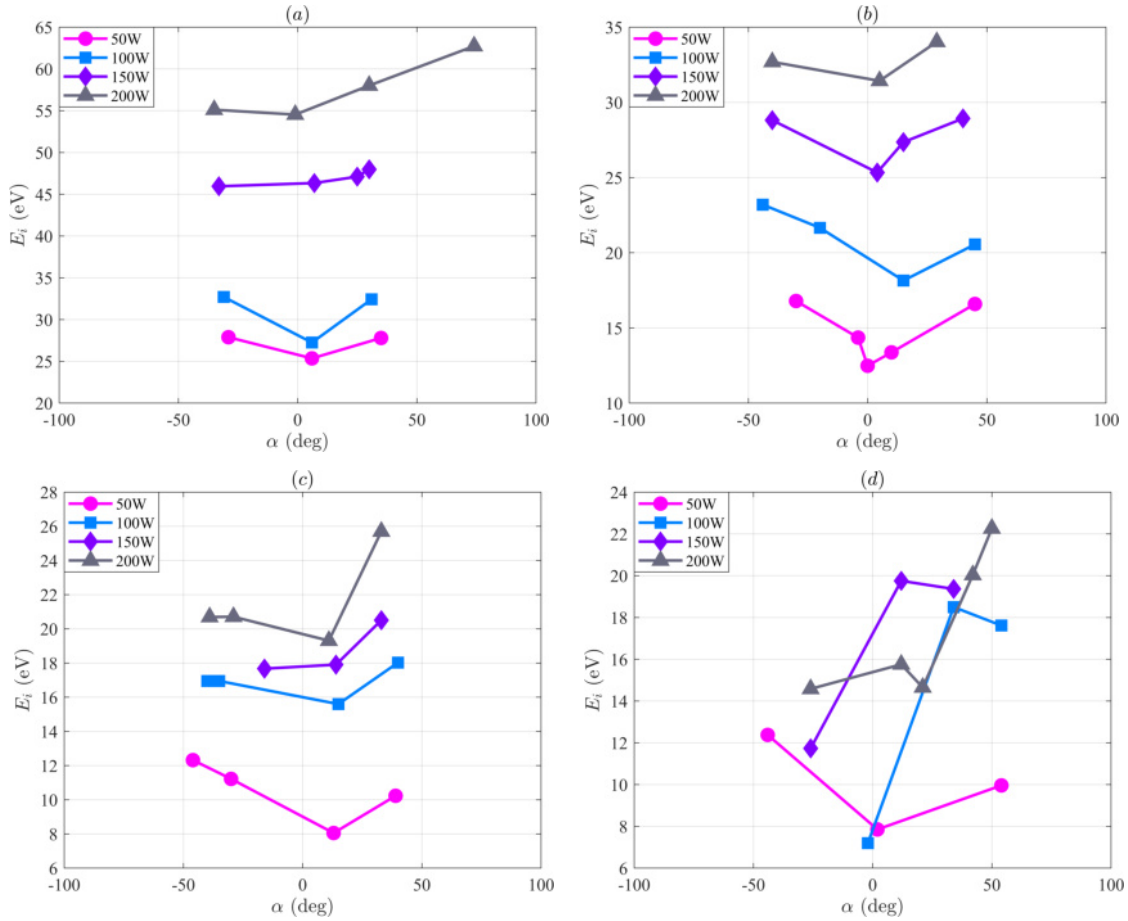

Figure 5.11: Most probable ion energy E_i measurements done with a RPA in a power range from $P_{MW,total} = 50\,\mathrm{W}$ to $P_{MW,total} = 200\,\mathrm{W}$. 2 A is set on each MN. (a) $\dot{m}_{Xe,total} = 5\,\mathrm{sccm}$, (b) $\dot{m}_{Xe,total} = 10\,\mathrm{sccm}$, (c) $\dot{m}_{Xe,total} = 15\,\mathrm{sccm}$, (d) $\dot{m}_{Xe,total} = 20\,\mathrm{sccm}$.

to 15 sccm, as seen in Figure 5.11(c). However, the average most probable energies seem to be similar for both 15sccm and 20 sccm as it can be seen in Figure 5.11(d). This last figure presents a most probable ion energy become strongly asymmetric and non-monotonic. This could be due to the same problems encountered with the ECRC1, as exposed in Section 4.4.

Figure 5.12 shows the evolution of the ion mean energy as a function of the power-to-mass flow rate ratio. In order to obtain the ion mean energy, the global average among all angles of the ion most probable energy have been used. The increase is linear (with a slope of $4/3\,\mathrm{eV.sccm.W^{-1}}$) and the measurements made with different mass flow rates overlap.

As it can be seen in Figure 5.10(a) for $\dot{m}_{Xe,total} = 5\,\mathrm{sccm}$ and $P_{MW,total} = 100\,\mathrm{W}$, two peaks are measured at $j \approx 0.11\,\mathrm{A.m^{-2}}$ and are centered at $\alpha = -35\mathrm{deg}$ and $\alpha = 35\mathrm{deg}$. Reported on the x-axis, they are comprised in the range $|[100; 215]|$ mm. A plateau is comprised at $j = 0.09\,\mathrm{A.m^{-2}}$ between $\alpha = -20\mathrm{deg}$ and $\alpha = 20\mathrm{deg}$ (i.e. $x \in [-95 : 95]$ mm). RPA measurements have been performed at both peaks center

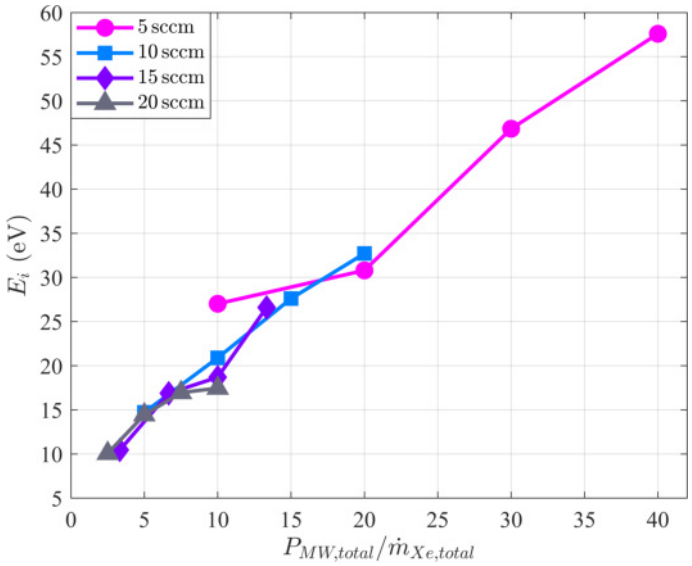

Figure 5.12: Most probable ion energy E_i measurements done with the RPA as a function of the power to mass flow rate ratio. (a) $\dot{m}_{Xe,total} = 5\,\text{sccm}$, (b) $\dot{m}_{Xe,total} = 10\,\text{sccm}$, (c) $\dot{m}_{Xe,total} = 15\,\text{sccm}$, (d) $\dot{m}_{Xe,total} = 20\,\text{sccm}$.

and in the plateau (i.e. $\alpha = [-35\,\text{deg}, 6\,\text{deg}, 35\,\text{deg}]$), as shown in Figure 5.13. The most probable ion energy is 32.7 eV at $\alpha = |35\,\text{deg}|$ and their IEDF (Ion Energy Distribution Function) spread is similar. The IEDF spread enlarges for $\alpha = 6\,\text{deg}$, with a lower most probable ion energy determined at 27.25 eV. The IEDF spread could increase closer to the cluster symmetry plane, as ions from both sources can be found in higher density.

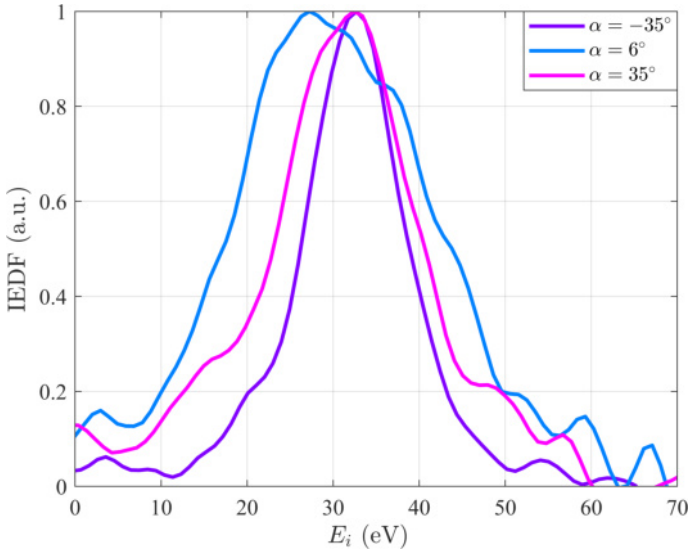

Figure 5.13: Normalized IEDFs measured through the RPA at positions of interest measured 380 mm from the origin. Conditions of operation: $\dot{m}_{Xe,total} = 5\,\text{sccm}$, $P_{MW,total} = 100\,\text{W}$, $I_{MN} = 2\,\text{A}$.

5.3 Ion velocity vector determination using LIF

5.3.1 LIF experimental setup

CNRS facility

The LIF measurements have been realised in the ICARE Laboratory of the CNRS of Orléans, France. Preliminary ignitions have been made in the EPIC-2 vacuum chamber (54 cm of diameter, 104 cm in length, Edwards GV110 main dry pump and 2 STP-iS2207 turbomolecular pumps, 10^{-4} mbar with 20 sccm of Xe). LIF measurements have been performed in the New Experiment on Electric Thrusters (NExET) vacuum chamber. With a length of 1.8 m and an internal diameter of 0.8 m, this chamber is equipped with an Edwards GV110 main dry pump and a STP-iS2207 turbomolecular pump. In addition, a cryopanel localised at the bottom centre of the chamber reaches temperatures down to 50 K. A dry pressure of 10^{-6} mbar can be reached, with an average pressure of 5×10^{-5} mbar with a total input mass flow rate of $\dot{m}_{Xe,total} = 5$ sccm. A Xenon bottle is connected to two independent Alicat 20 sccm Flow Meter mass flow controllers by a Swagelok T gas-splitter. Each controller is linked to a source. The total MW power input through the LIF measurements remains constant at $P_{MW,total} = 100$ W. Moreover, the current set at each MN is set to $I_{MN} = 2$ A.

LIF physical principle

The ion velocity can be determined by LIF along the laser beam direction by measuring the Doppler shift of absorbed photons. The isotropic fluorescence occurs when a probed ion, excited by the laser, deexcites to a lower energy state and emits a photon. The excitation from one quantum level to another happens when the photon matches the energy difference in between the two levels. As selection rules bound the energies allowed for the previously stated transitions, a specific species can be studied. Measuring the frequency at which the laser beam energy is absorbed allows the determination of ion Doppler shift, hence its velocity depending on the laser beam direction:

$$\Delta\nu = \nu - \nu_0 = \frac{1}{2\pi}\boldsymbol{k}\cdot\boldsymbol{v}, \tag{5.2}$$

$$\nu_k = c\frac{\nu - \nu_0}{\nu}. \tag{5.3}$$

where $\Delta\nu$ represents the Doppler shift, ν the laser frequency, ν_0 the studied transition unshifted frequency, $\boldsymbol{k}$ the laser beam wave vector, $\boldsymbol{v}$ the velocity vector of the studied particle, v_k its velocity parallel to $\boldsymbol{k}$ and c the speed of light. By sweeping the laser frequency, the IVDF (Ion Velocity Distribution Function) can be determined. Indeed, the fluorescence signal intensity is proportional to the density of the

particles for a given frequency. Thus, a frequency sweep associates a shift—i.e. a velocity—to a (relative) density. Table 5.3 details the Xenon ions (Xe II) population probed in the metastable level.

		Transition	λ air (nm)
Xe II	Excitation	$5s^2 5p^4\,(^3P_2)\,5d^2\,[4]_{7/2} \rightarrow 5s^2 5p^4\,(^3P_2)\,6p^2\,[3]^\circ$	834.72
	Fluorescence	$5s^2 5p^4\,(^3P_2)\,6p^2\,[3]^\circ \rightarrow 5s^2 5p^4\,(^3P_2)\,6s^2\,[2]_{3/2}$	541.91

Table 5.3: Probed optical transitions, excitation and fluorescence wavelengths in LIF[94].

Optical bench

Figure 5.14 depicts the two configurations used for LIF spectroscopy measurements. The same configurations are used with a single source. Configuration (a) focuses on measuring the ion axial velocity, whereas configuration (b) on radial velocity. Regardless of the configuration, this setup allows us to perform time-averaged LIF. First of all, a laser beam is produced by an amplified tunable single-mode external cavity laser diode (1) represented by the red path on the scheme. This diode can deliver up to 700 mW of power in the near-infrared spectral domain. The laser remains mode-hop free over a frequency tuning range of more than 20 GHz. A powermeter is juxtaposed to the diode to guarantee that the power density remains in the order of a few mW.mm^{-2} to avoid the saturation of the natural line shape. A first BS (Beam Splitter) $(2)_a$ divides the beam into two main paths. The first one aims to analyse the emitted laser beam, whilst the second brings the beam to the thruster. Focusing on the laser beam analysis, a second BS $(2)_b$ directs part of the beam to a Fabry-Pérot interferometer (with a 1 GHz free spectral range), linked to an oscilloscope. The latter is used to check both the quality and the stability of the laser mode in real time.

Mode hops can occur through the laser wavelength sweep (as the electric intensity of the diode decreases). These hops are to be avoided to obtain a smooth sweep. Moreover, they can in addition be checked on the oscilloscope. The remaining part of the laser beam encounters a third BS $(2)_c$, which splits the beam towards a photodiode and a collimator $(8)_a$. The photodiode goal is to measure the laser beam intensity at all times and to communicate it to the control computer. The collimator $(8)_a$ is linked to a high-resolution wavelength meter by an OF (Optical Fiber). The wavemeter measures the real-time laser beam wavelength and outputs the latter to the control computer. It is calibrated using a HeNe stabilised laser with a 632.9914 nm wavelength. The second main laser beam emitted towards the thruster begins by being reflected on a first mirror $(3)_a$, before passing through a first diaphragm $(4)_a$ and being reflected on a second mirror $(3)_b$. The half-wave

blade (5) and the polariser (6) guarantee that the beam is linearly polarised. The mechanical chopper (7), linked to the lock-in amplifier, has a modulation frequency of 1443Hz. After being reflected on mirrors $(3)_c$ and $(3)_d$, the beam passes through a second diaphragm $(4)_b$ to focus and is collected by a collimator $(8)_b$. It is then carried by a single mode OF, before being injected in the vacuum chamber (9) with an adapted feedthrough. When measuring the axial velocity, the injection is done in the -z-axis direction. Regarding the radial velocity measurements, the injection is performed on the x-axis direction.

A detection made out of a lens (10) of a 60 mm focal distance focuses the fluorescence light in an OF with a diameter of 200 μm. With a magnification ratio of 1, the spatial resolution of the detection remains the same as the diameter of the OF, i.e. 200μ m. In configuration (a) (axial velocity), the detection branch has an angle of 25° with respect to the injection axis. For configuration (b) (radial velocity), this angle is set to $-25°$ regarding the z-axis. Both the laser injection (9) and the detection branch (10) are mounted on two Newport linear translation stages with a 10 cm range. A 10 cm$\times$10 cm surface can be covered, with a minimum step of 10^{-3} mm. The x-axis is aligned with the sources exhaust plane, its origin being localised at the CT of the source of interest. The z-axis is aligned with the CT of the source of interest, its origin being localised at the exhaust plane of the source. The OF originating from the detection branch (10) passes through an adapted feedthrough and is linked to a monochromator. The latter isolates the fluorescence wavelength of interest from the rest of the spectrum. Finally, a photomultiplier acts as a light detector, converting the light into an electrical signal. The chopper and the photomultiplier are both connected to a lock-in amplifier, matching their frequencies to discriminate the fluorescence light from the plasma emission. The control computer receives as inputs the wavelength of the original beam, its intensity as well as data of the lock-in amplifier. It is connected with the laser controller to sweep the diode frequency. A software controls all the previously stated components.

5.3.2 LIF measurements sorting

Splitting and broadening of the recorded spectra

As found in various previous works[85], [94], [95], the Xe II IVDFs typically follow a Maxwellian distribution. However, as it as been demonstrated in previous LIF spectroscopy experiments, several factors might affect the lineshapes to the extent of making it unfit a quasi-Gaussian shape[85], [96]. The lineshape broadening and the presence of two peaks in the latter can result from the Zeeman and Pachen-Back effects.

In order to understand the causes of the splitting and broadening, a fluorescence lineshape modeling developed by Vinci[97] has been used. The model will not be de-

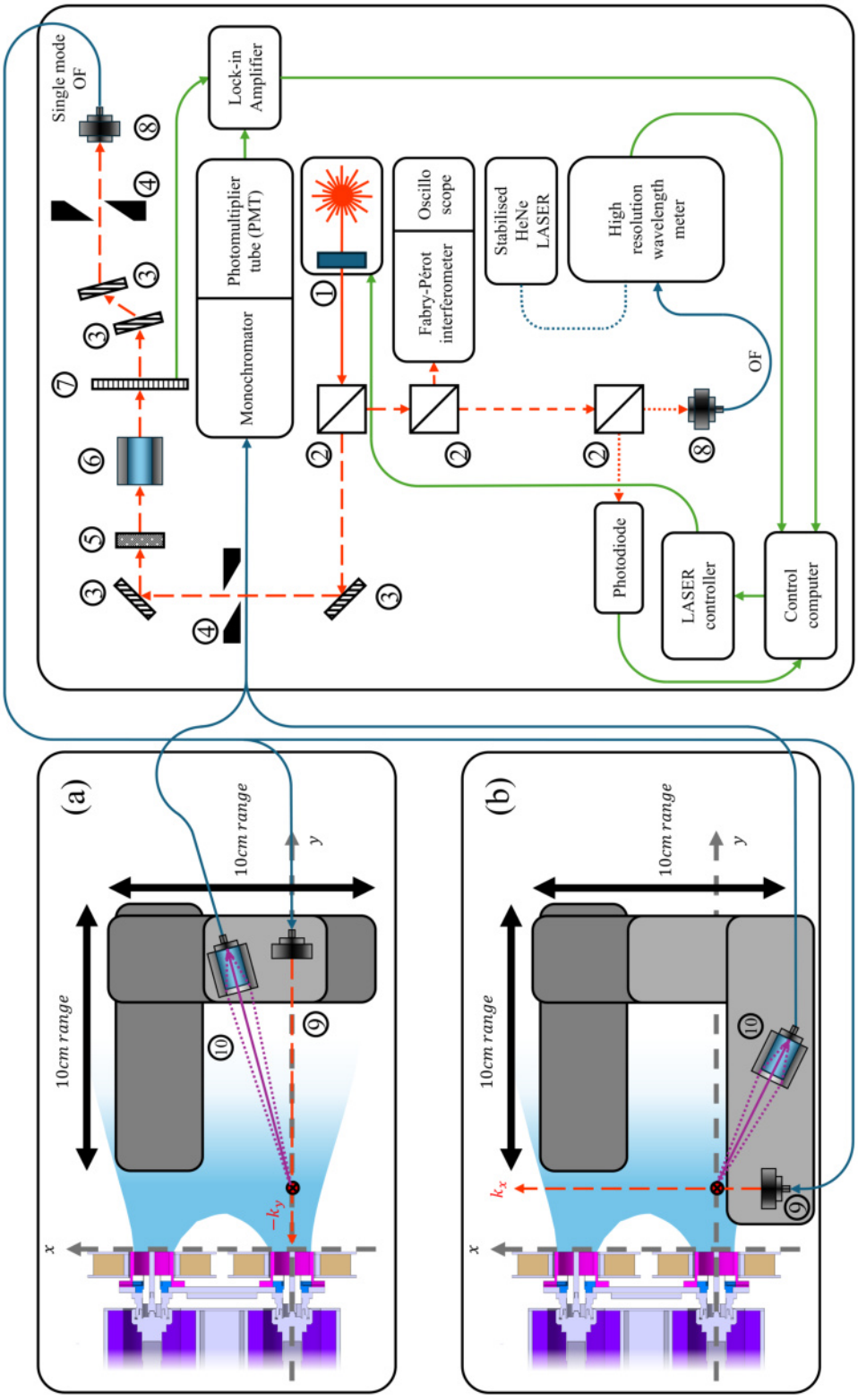

Figure 5.14: Diagram of the LIF optical bench with in-vacuum optics. (a) u_{zi} measurements and (b) u_{xi} measurements. 1. Tunable single-mode laser diode and powermeter 2. BSs 3. Mirrors 4. Diaphragms 5. Half-wave blade 6. Polariser 7. Mechanical chopper 8. Collimators 9. Laser injection 10. Detection branch.

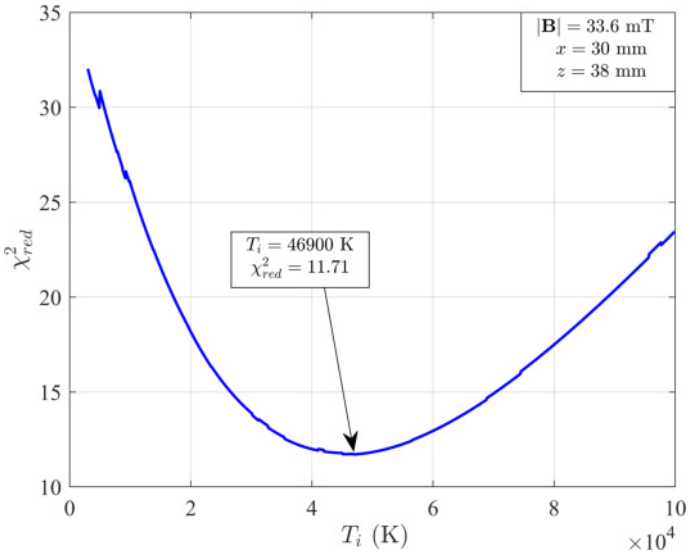

Figure 5.15: Instance of χ^2_{red} evolution with T_i. The highlighted point at $T_i = 46900\,\mathrm{K}$ identifies the value that best fits the spectrum recorded at $[x = 30\,\mathrm{mm}; z = 38\,\mathrm{mm}]$. Conditions of operation: $\dot{m}_{Xe,total} = 5\,\mathrm{sccm}$, $P_{MW,total} = 100\,\mathrm{W}$, $I_{MN} = 2\,\mathrm{A}$.

tailed in this manuscript, as it has been presented in numerous works[95], [96], [98] . To determine the optimal ion temperature, an algorithm computing the reduced chi-square χ^2_{red} has been implemented, quantifying the goodness of fit given the experimental and theoretical lineshapes. The optimal ion temperature is determined with a resolution of 100 K. Figure 5.15 depicts the evolution of χ^2_{red} as a function of T_i. The best fitting is done with an optimal ion temperature of $T_i = 46900\,\mathrm{K}$. The latter corresponds to the velocity spread in the laser direction. Still, as it can be seen in Figure 5.16, the fit is far from optimal. It appears that the Zeeman and Pachen-Back effects filtered by the lineshape modeling cannot explain the splitting observed in this measurement, as shown in Figure 5.16. Although a single example is shown here, every measurement has been treated with the modeling. Consistently, the experimental lineshapes could not be reconstructed with the algorithm.

The Zeeman and Pachen-Back effects for the Xe II transition become observable and influential around the $200 - 300\,\mathrm{G}$ threshold. Above this level, there effects are comparable to Doppler and hyperfine widths[98], [99]. Below this threshold, they remain smaller than other broadening mechanisms and have only a minor influence on the line shape[99], [100]. Still, the original signal reconstruction is impossible with the assumption of a single population, even considering the Zeeman and Pachen-Back effects—while the MF strength remains higher than the 200 G threshold for $z \leq 70\,\mathrm{mm}$. Hence, the presence of a secondary ion population generated by ionization of the neutral background through the plume expansion could represent an explanation for these effects. Figure 5.17 depicts a two-peaks distribution of u_{xi} measured in the cluster horizontal plane for $[x = 30\,\mathrm{mm}; z = 38\,\mathrm{mm}]$. Two Gaussian fittings can be used to reconstruct the raw LIF signal.

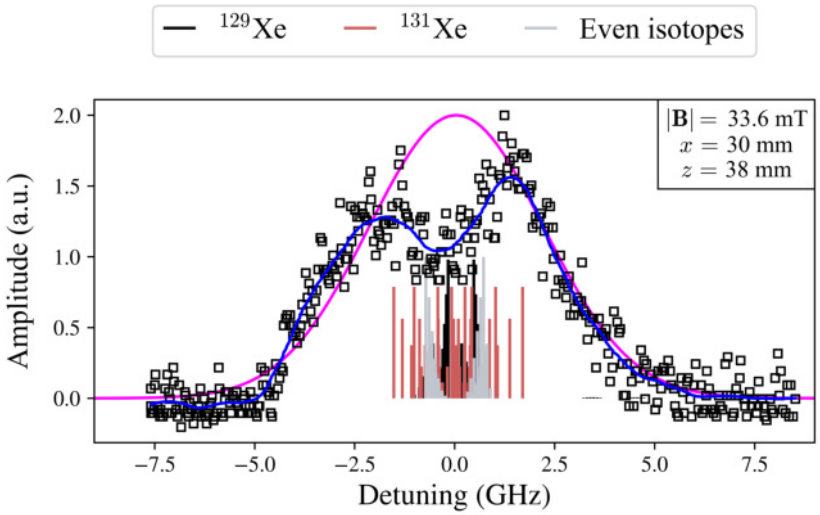

Figure 5.16: Experimental (squares) and smoothed (blue line) versus modeled (pink line) lineshape of Xe II. The experimental data points are Doppler shifted to fit the model profile. Measurement taken at $[x = 30\,\text{mm}; z = 38\,\text{mm}]$. Conditions of operation: $\dot{m}_{Xe,total} = 5\,\text{sccm}$, $P_{MW,total} = 100\,\text{W}$, $I_{MN} = 2\,\text{A}$.

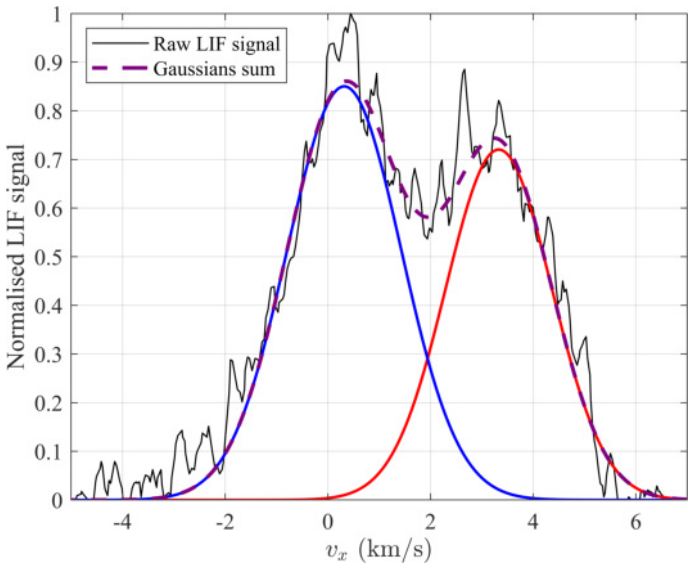

Figure 5.17: Normalized Xe II IVDFs measured by means of LIF spectroscopy in the x-direction at 834.7 nm in the ECRC2 plume. Measurement taken at $[x = 30\,\text{mm}; z = 38\,\text{mm}]$. Raw LIF signal is plotted in black, Gaussian fittings in red and blue and their sum approximating the raw LIF signal in purple dotted line. Conditions of operation: $\dot{m}_{Xe,total} = 5\,\text{sccm}$, $P_{MW,total} = 100\,\text{W}$, $I_{MN} = 2\,\text{A}$.

Development of a sorting algorithm

The Zeeman and Pachen-Back effects have been ruled out by the fluorescence line-shape modeling developed by Vinci[97] in every LIF measurements performed. The consistence presence of two peaks in the LIF measurements is thus attributed to the presence of two populations—as seen in Figure 5.17. Therefore, the development of an ion population sorting algorithm appears to be mandatory in order to determine which population is associated to which peak in every measurement. In a classic ECRT, the secondary population generated through ionization of the neutral background appears to have a lower velocity overall. In fact, the secondary population is usually believed to be slower and of lower magnitude. However, simply sorting the secondary population as the slowest and weakest in a closed-line MF would lead to unrealistic results.

The sorting algorithm has been developed to determine the best raw LIF spectra fittings with single- and dual-Gaussian approximations using least-squares. Each Gaussian fit is linked to a specific population, labelled as:

- ***MP (Main Population):*** Xe II ion generated in the ionization chamber and believed to be accelerated by the ambipolar field in the plume expansion.
- ***SP (Secondary Population):*** Xe II ion generated by ionization and CEX arising from the interaction between the electrons and the background neutral gas.

The algorithm fits in parallel the analysed spectrum with a single and a dual Gaussian approximation. Each fitting is optimised through the Gaussians parameters (amplitude, mean and width) through least-squares to determine a relative fitting error. Finally, the algorithm compares the latter between the single and the dual Gaussian approximations to determine if the spectrum presents a single population or a combination of two. It is important to mention that each spectrum is normalized regarding its maximum intensity. In order to rule out some unphysical approximations, some thresholds are applied to guide the fittings:

- The normalized amplitude A of each Gaussian is set to be greater than 0.01 but lower than 2. This condition is mainly implemented to eliminate the configurations with a flat Gaussian, as well as to get rid of Gaussian with negative amplitude: $0.1 < A < 2$.
- The width W of each Gaussian is set to be inferior to 1.5× the span of the associated velocity sweep: $0 < W < 1.5\,(\mathrm{v}_{max} - \mathrm{v}_{min})$.
- The mean value M of each Gaussian remains in the span of the associated velocity sweep: $\mathrm{v}_{min} < M < \mathrm{v}_{max}$.
- Continuity with neighbouring measurements.

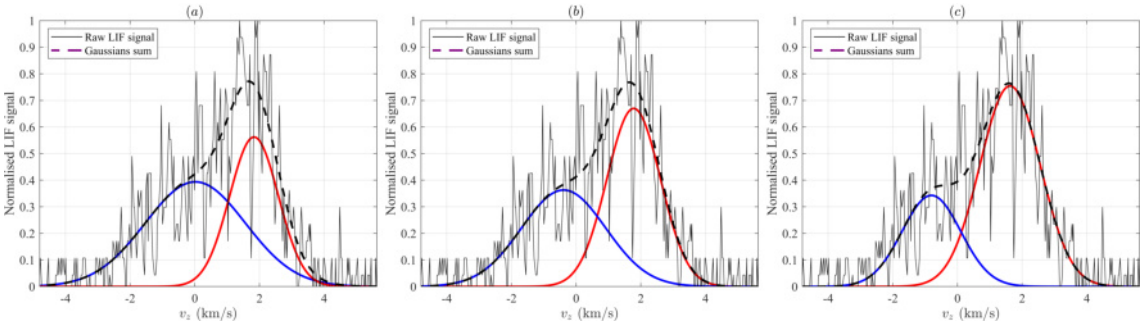

Figure 5.18: Normalized Xe II IVDFs measured by means of LIF spectroscopy in the z-direction at 834.7 nm in the ECRC2 plume. Measurement taken at $[x = 10\,\text{mm}; z = 30\,\text{mm}]$. Raw LIF signal is plotted in black, Gaussian fittings in red and blue and their sum approximating the raw LIF signal in black dashed line. (a), (b) and (c) depicts different Gaussian fittings, with (a) having the least relative fitting error. Conditions of operation: $\dot{m}_{Xe,total} = 5\,\text{sccm}$, $P_{MW,total} = 100\,\text{W}$, $I_{MN} = 2\,\text{A}$.

Still, it is impossible to state on which fitting corresponds to which population through the classification algorithm alone. It is mandatory to manually inspect each measurement and the continuity with its surroundings to determine the population classification. Two sorting conditions can be defined from the generation process of each population: $u_{zi,MP} \geq u_{zi,SP}$ and $u_{xi,MP} \leq u_{xi,SP}$. Figure 5.17 depicts a clear example where two distinct populations can be identified. However, Figures 5.18 present three fittings of the same LIF measurement made at $[x = 10\,\text{mm}; z = 30\,\text{mm}]$. Figure 5.18(a) presents the fitting with the least relative fitting error. Moreover, it presents the best continuity with surrounding measurements. Hence, this fitting is considered to be the optimal one for this measurements and is chosen to determine the characteristics of both populations.

5.3.3 Single source measurements

LIF measurements have been performed in the first place in a single source configuration, with $\dot{m}_{Xe,total} = 2.5\,\text{sccm}$ and $P_{MW,total} = 50\,\text{W}$. The current applied on the MN remains set at $I_{MN} = 2\,\text{A}$. Through this subsection, the figures will include the following elements:

- The MN is displayed in brown.
- The boundaries of the IC are represented in grey.
- The spaces between the IC boundaries and the CT are coloured in purple.
- The CT is coloured in pink.
- MFLs of interest are displayed with dotted lines at $x = [2.25, 7.5, 10, 15]\,\text{mm}$ and $z = 0\,\text{mm}$.

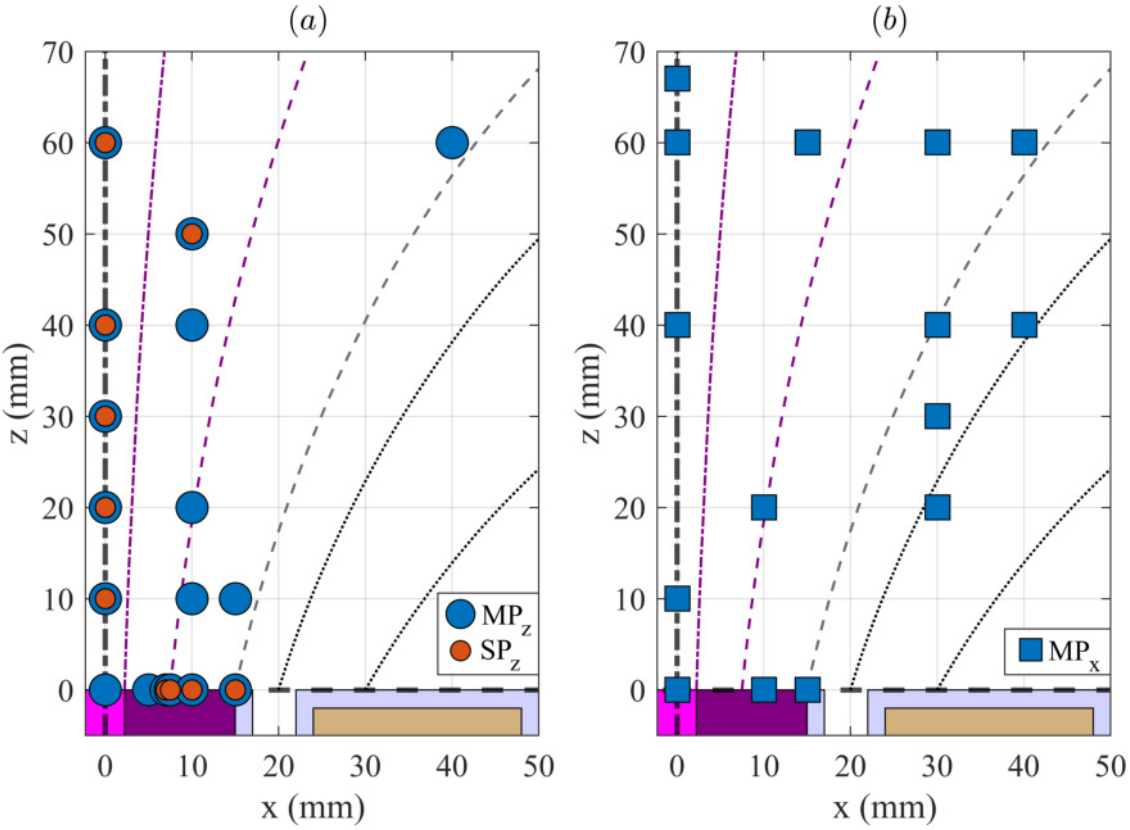

Figure 5.19: Xe II LIF measurements position for a single source in the z-direction (a) and x-direction (b), overlapped with a cross-section top view of a single source. Blue circles and squares represent respectively the z-direction and x-direction measurements where the MP can be identified. Orange circles correspond to the z-direction SP measurements.

Figure 5.19 presents the position of the LIF measurements in both the z (a) and x-directions (b) for a single source. The x-axis and z-axis are centered on the single source exhaust plane and the CT. Measurements are limited in space and resolution because of the low plasma density farther downstream—as the signal intensity is proportional to the Xe II density. Only the right part of the source concerning the z-axis has been probed. Four measurements in the x-direction were performed on the left part to test the source axisymmetry as it will be detailed further in the manuscript. Most of the measurements made for the single source present a single population distribution, associated to the MP. As aforementioned, the latter is believed to be generated in the IC. The SP could only be found in the measurements made in the z-direction. Moreover, it is observed at the source exhaust plane, where a higher neutral density could be expected.

Single source z- and x- measurements

- **Relative density**

Figure 5.20 refers to the normalized relative density of the MP based on its Gaussian approximation integral in the z-direction for a single source. The integral is based on the mean, amplitude and width of the Gaussian approximation. Normalization is made upon the sum of the Gaussian integrals for a given location.

A reference density—obtained by performing LIF measurements on a plasma of known density—is mandatory to conclude on the absolute density of the measurements. Indeed, knowing the light intensity corresponding to the density of reference for a given transition, it would have been possible to determine the absolute density of each population. Still, it remains possible to compare the density of a given population with respect to the other. The MP is predominantly present in the single source plume in the z-direction (i.e. relative density $> 50\%$).

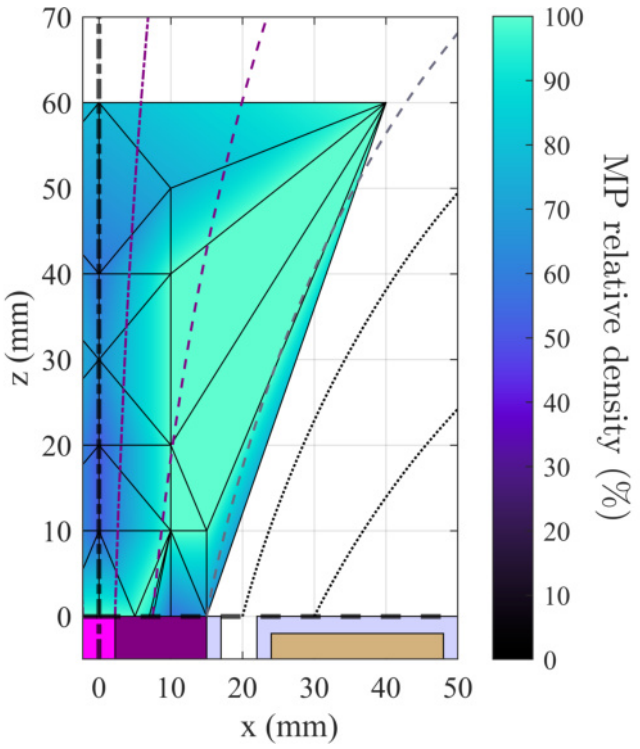

Figure 5.20: Xe II MP normalized relative density in the z-direction for a single source.

LIF measurements performed in the x-direction present a single population assimilated as the MP according to the signal quality and intensity. A second hypothesis relies on the possibility that the two populations have a similar IVDF. Figure 5.20 showed a small relative density of the SP in regard of the MP. They could be differentiate as the SP is notably slower than the MP. However, considering a low velocity in the x-direction for both populations—as it will be detailed in Fig-

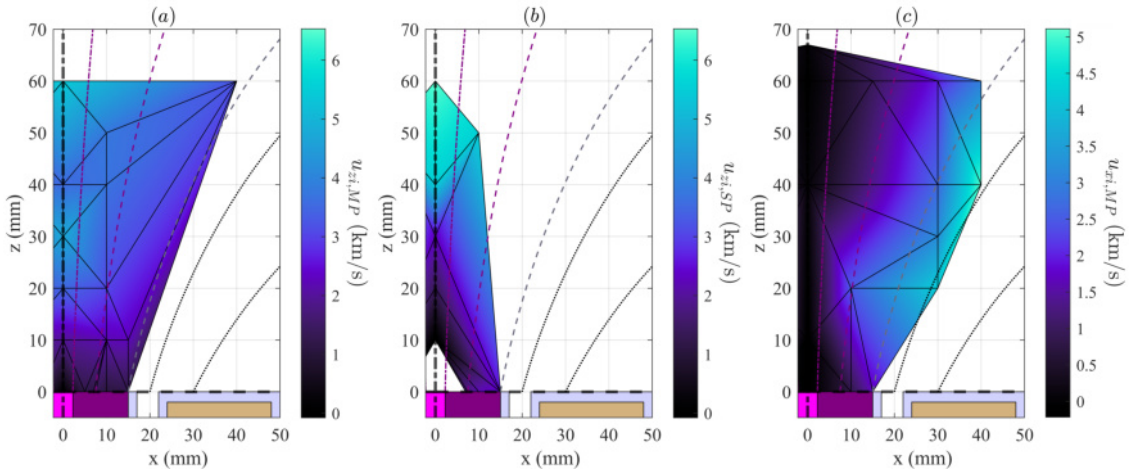

Figure 5.21: Xe II $u_{zi,MP}$ (a), $u_{zi,SP}$ (b) and $u_{xi,MP}$ (c) single source colormaps.

ure 5.21(c)—in regard of the z-direction, it is possible that the IVDF of the SP is shadowed by the one of the MP.

- **Velocity**

The mean of the Gaussian fittings defines the ion mean velocity of each population, u_{zi} in the z-direction and u_{xi} in the x-direction. Figure 5.21(a) depicts the u_{zi} of the MP and Figure 5.21(b) refers to the u_{zi} of the SP. The maximum u_{zi} is reached at $[x = 0\,\text{mm}; z = 60\,\text{mm}]$ with 6.5 km/s with the SP. The choice to associate this point with the SP is lead by the continuity in terms of amplitude within the surrounding measurements. Both populations u_{zi} constantly increase along the z-axis from the source exhaust plane to $z = 60\,\text{mm}$.

Figure 5.21(c) presents the MP ion velocity $u_{xi,MP}$ in the x-direction from the Gaussian approximation mean. The latter increases along with the distance to the central axis and the source exhaust plane. The maximum is reached at $[x = 40\,\text{mm}; z = 40\,\text{mm}]$ with 5.11 km/s, while a near-zero velocity is probed along the central axis. As for $u_{zi,MP}$, the ambipolar field is responsible for this behavior, as the MFLs diverge.

- **Temperature**

The ion temperature T_i, referring to the spread in the probed velocity component, is determined by the standard deviation σ of the Gaussian fit for each population[94] as presented in Equation 5.4.

$$T_i = \frac{m_{Xe}\,\sigma^2}{k_B}. \tag{5.4}$$

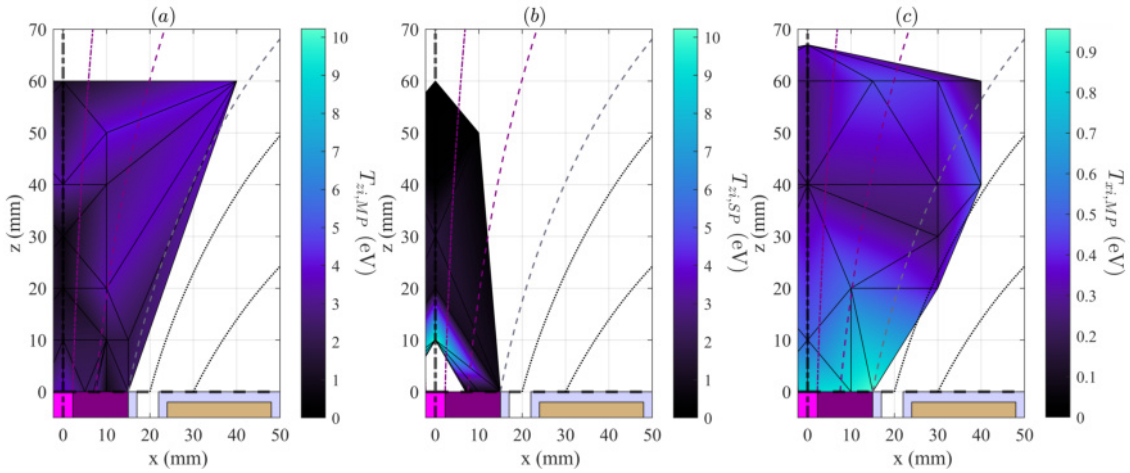

Figure 5.22: Xe II $T_{zi,MP}$ (a), $T_{zi,SP}$ (b) and $T_{xi,MP}$ (c) single source colormaps.

Figure 5.22(a) presents the $T_{zi,MP}$. It remains between $T_{zi,MP} = 0.75\,\text{eV}$ and $T_{zi,MP} = 4.1\,\text{eV}$, while increasing along the distance to the central axis. This population is mainly generated in the IC before being accelerated through the MN, so it maintains a relatively low temperature through the plume expansion. In contrast, the SP ion temperature decreases along the distance from the source exhaust plane, as shown in Figure 5.22(b). Its maximum is reached at $[x = 0\,\text{mm}; z = 10\,\text{mm}]$ with $T_{zi,MP} = 10.25\,\text{eV}$ and remains at $T_{zi,MP} < 1\,\text{eV}$ elsewhere. As the ion temperature is computed from the standard deviation of the Gaussian approximation, it relies upon the signal quality and intensity. Considering that the SP is of very low density relatively to the MP, the signal quality and intensity might lead to the very high temperature found at $[x = 0\,\text{mm}; z = 10\,\text{mm}]$.

Figure 5.22(c) represents the ion temperature $T_{xi,MP}$ of the MP in the x-direction. It decreases along the distance from the source exhaust plane from a maximum of 0.95 eV to a minimum of 0.15 eV. The higher temperature at the exhaust could result from the higher divergence localised nearby the latter.

On average, the temperature is lower in the x-direction by a factor of 4 in comparison to the z-direction. This difference is mainly due to ionization not occurring at the same value of ϕ but over a region, inducing the presence of a distribution. Near the source, the MFLs are more concentrated and aligned with the z-axis, which naturally collimates the ion beam in this direction. In contrast, the x-direction does not experience the same level of directed acceleration, as the radial electric field components are weaker or less consistent.

- **Source axisymmetry**

$u_{xi,MP}$ measurements have been performed on both sides of the z-axis to check the single source symmetry, as shown in Table 5.4. At $z = 0\,\text{mm}$, the velocity difference between $x = -7\,\text{mm}$ and $x = 7\,\text{mm}$ reaches $0.65\,\text{km/s}$. For $z = 20\,\text{mm}$,

the difference remains under 0.5 km/s between $x = -7$ mm and $x = 7$ mm, when it comes to 0.55 km/s at $z = 40$ mm. These differences could be explained by a non-perfect gas distribution in the prechamber, even though the latter has been designed to prevent such disparities. Moreover, velocities tend to be higher in magnitude by some hundreds of m/s on the right part of the z-axis for $z > 0$ mm. This slight difference can be explained by misalignment in the source assembly or between the laser injection and the source. Still, the source is considered to be axisymmetric.

x (mm) \ z (mm)	0	20	40
-7	-0.15	-0.8	-0.75
-5	N/A	-0.6	N/A
0	N/A	-0.02	-0.02
5	N/A	0.2	N/A
7	0.8	0.3	0.2

Table 5.4: u_{xi} on both sides of the z-axis (km/s).

Single source total in-plane velocity

The in-plane velocity is determined through u_{zi} and u_{xi}: $\tilde{u}_i = \sqrt{u_{zi}^2 + u_{xi}^2}$. Figure 5.23(a) presents the MP in-plane velocity colormap. The velocity magnitude increases along the z-axis. A maximum in-plane velocity of $\tilde{u}_{i,MP} = 5.45$ km/s can be found at $[x = 0\,\text{mm}; z = 60\,\text{mm}]$. Ion streamlines are seen to be detached outward from the MFLs already at the exhaust of the source. This makes sense as ions are essentially unmagnetised under the magnetic field strength used in this work. However, they essentially become straight downstream ($z > 35$ mm), as shown in Figure 5.23(b).

Based on both the z- and x-direction measurements, both the MP and the SP populations exist in the plume of a single ECR source. However, their u_{xi} might be too similar to distinguish one from the other in the x-direction. Considering this assumption, Figure 5.24(a) depicts the in-plane velocity colormap and Figure 5.24(b) the local velocity vectors and ion streamlines. The SP ions present a faster in-plane velocity further away from the exhaust, with a maximum reached as well at $[x = 0\,\text{mm}; z = 60\,\text{mm}]$ with $\tilde{u}_{i,SP} = 6.53$ km/s. However, $\tilde{u}_{i,SP}$ presents a near-zero velocity closer to the exhaust in comparison to $\tilde{u}_{i,MP}$. As the $u_{xi,MP}$ has been used to compute $\tilde{u}_{i,SP}$, it is difficult to assess the worthiness of the local velocity vectors. Moreover, the ion trajectory tends to align progressively to the MFLs. Considering that the SP is generated in the plume instead of the IC, these measurements remain coherent due to the lower velocity in the near-exhaust expansion.

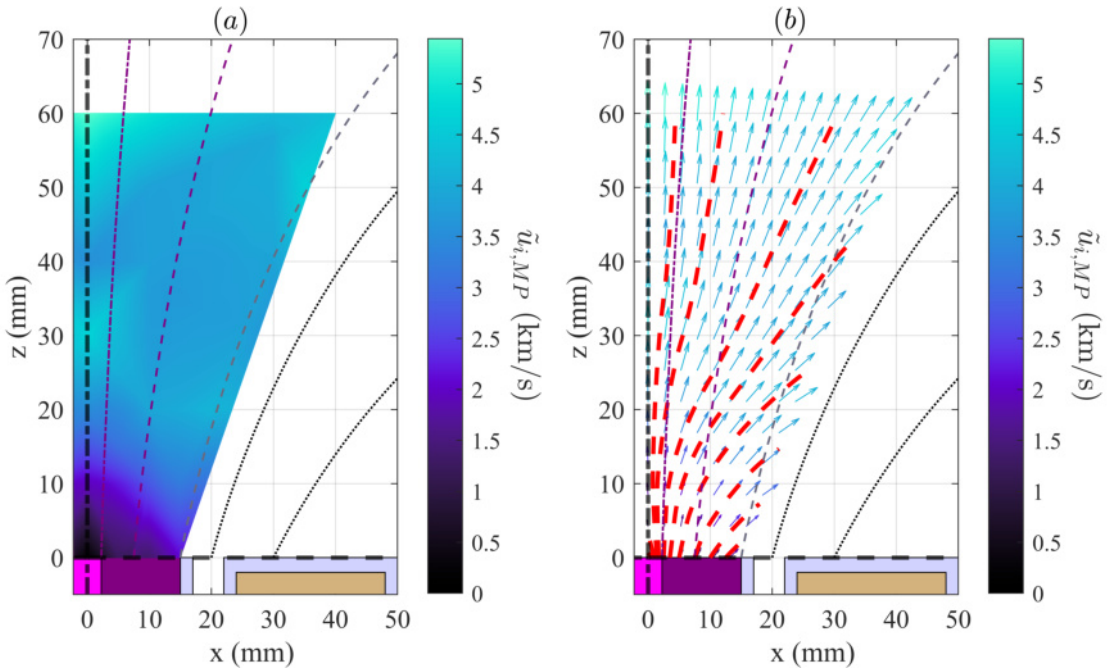

Figure 5.23: Xe II $\tilde{u}_{i,MP}$ single source local colormap (a) and velocity vectors and ion streamlines (b), displayed in red dotted lines.

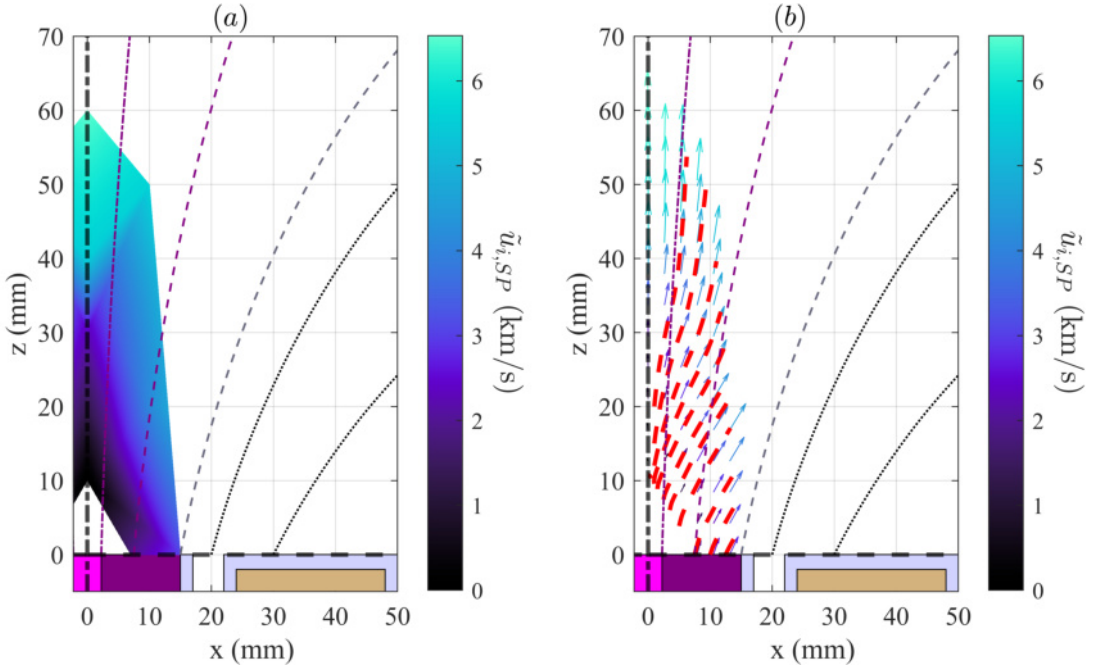

Figure 5.24: Xe II $\tilde{u}_{i,SP}$ single source local colormap (a) and velocity vectors and ion streamlines (b), displayed in red dotted lines.

5.3.4 ECRC2 measurements

LIF measurements have been performed on the ECRC2 with $\dot{m}_{Xe,total} = 5\,\text{sccm}$ and $P_{MW,total} = 100\,\text{W}$. The gas and power splittings have been detailed in Section 5.1. The current applied on the MNs remains set at $I_{MN} = 2\,\text{A}$. Through this subsection, the figures will include the following elements:

- The MN is displayed in brown.
- The boundaries of the IC are represented in grey.
- The spaces between the IC boundaries and the CT are coloured in purple.
- The CT is coloured in pink.
- MFLs of interest are displayed at $z = 0\,\text{mm}$. They are generated at the following x coordinates:
  - $x = 25\,\text{mm}$ (black, dotted line): middle of the inner part of the MN.
  - $x = 35\,\text{mm}$ (black, dotted line): end of the inner part of the MN.
  - $x = 45\,\text{mm}$ (grey, dashed line): inner boundary of the inner part of the IC.
  - $x = 51.375\,\text{mm}$ (purple, dashed line): middle of the inner part of the IC.
  - $x = 57.75\,\text{mm}$ (purple, dashed-dot line): inner boundary of the CT.
  - $x = 62.5\,\text{mm}$ (purple, dashed-dot line): outer boundary of the CT.
  - $x = 68.625\,\text{mm}$ (purple, dashed line): middle of the outer part of the IC.
  - $x = 75\,\text{mm}$ (grey, dashed line): inner boundary of the outer part of the IC.
  - $x = 78\,\text{mm}$ (black, dotted line): outer boundary of the outer part of the IC.
  - $x = 83\,\text{mm}$ (black, dotted line): beginning of the outer part of the MN.

The MP and SP presented in this section are defined similarly to the single source, as presented in Section 5.3.2. Only the right part of the cluster concerning its symmetry plane has been probed, including measurements done at $x = -10\,\text{mm}$ to test the symmetry in the ECRC2. Figure 5.25 presents the position of the LIF probed points in both the z (a) and x-directions (b) for the ECRC2. The x-axis and z-axis are centered on the single source exhaust plane and the cluster symmetry plane. As for the single source, measurements are limited in space and resolution due to the low signal intensity and quality.

ECRC2 symmetry testing

Six measurements in the z-direction were performed near the z axis to test the plume symmetry. They were made at $z = [15, 40, 50]\,\text{mm}$ for both $x = -10\,\text{mm}$

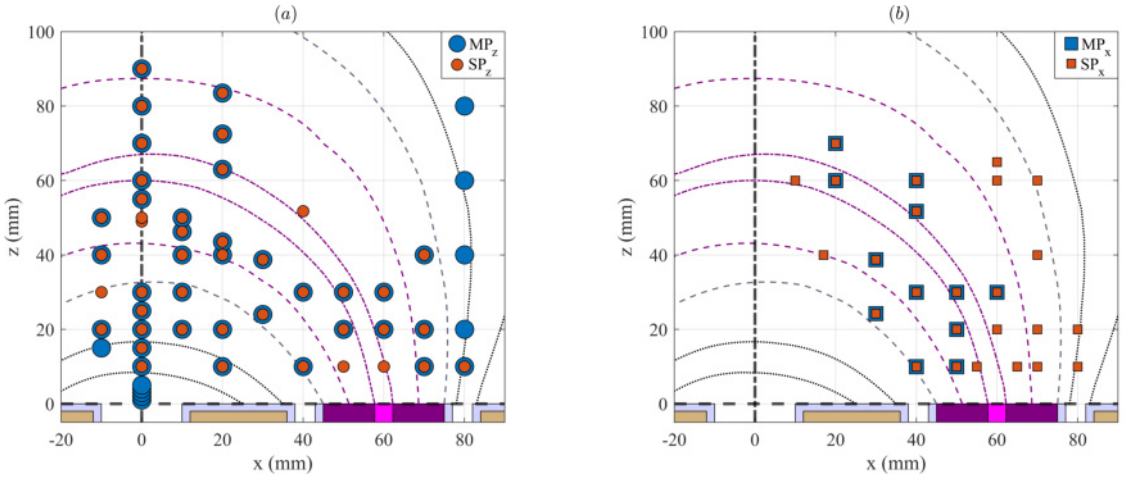

Figure 5.25: Xe II LIF measurements position for the ECRC2 in the z-direction (a) and x-direction (b), overlapped with a cross-section top view of ECRC2. Blue circles and squares represent respectively the z-direction and x-direction measurements where the MP can be identified. Orange circles and squares correspond to the z-direction and x-direction SP measurements.

and $x = 10\,\text{mm}$. Figure 5.26 depicts an example of the raw signal and the fitting at $z = 40\,\text{mm}$ and $x = 10\,\text{mm}$. The signal quality is impacted by many factors, such as the lock-in parameters—such as its sensibility—and the local ion density. The cluster symmetry could be proved in a better way by measuring the ion velocity in the x-direction. Figure 5.27 presents the Gaussian approximations of these measurements, differentiated between MP and SP.

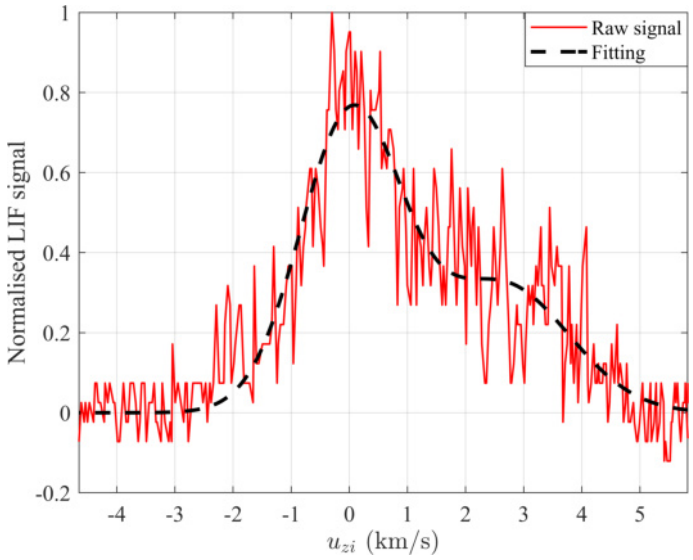

Figure 5.26: Xe II IVDFs for the ECRC2 made in the z-direction at $z = 40\,\text{mm}$ and $x = 10\,\text{mm}$.

Table 5.5 summarizes the differences in Gaussian parameters between $x = -10$ mm and $x = 10$ mm. The highest shift in the most probable velocity for the

MP is found at $z = 50\,\text{mm}$ with $|\Delta u_{zi,MP}| = 641\,\text{m/s}$. The SP presents a near-zero velocity with a constant shift around 100 m/s. The populations have a similar amplitude on both sides of the cluster symmetry plane, with a maximum difference of 7.6% at $z = 15\,\text{mm}$ for the MP. Finally, the highest ion temperature delta is found at $z = 15\,\text{mm}$ with 0.65 eV for the SP. These differences can be justified by the complex alignment in the LIF setup and possible changes in the cluster functioning through the measurements. However, the cluster is considered symmetric regarding its symmetry plane.

	$z = 15\,\text{mm}$		$z = 40\,\text{mm}$		$z = 50\,\text{mm}$	
	MP	SP	MP	SP	MP	SP
$\lvert\Delta u_{zi}\rvert$ (m/s)	N/A	106	182	106	641	109
$\lvert\Delta T_{zi}\rvert$ (eV)	N/A	0.65	0.37	0.3	0.54	0.59

Table 5.5: Gaussian parameters differences on both side of the cluster symmetry plane in the z-direction.

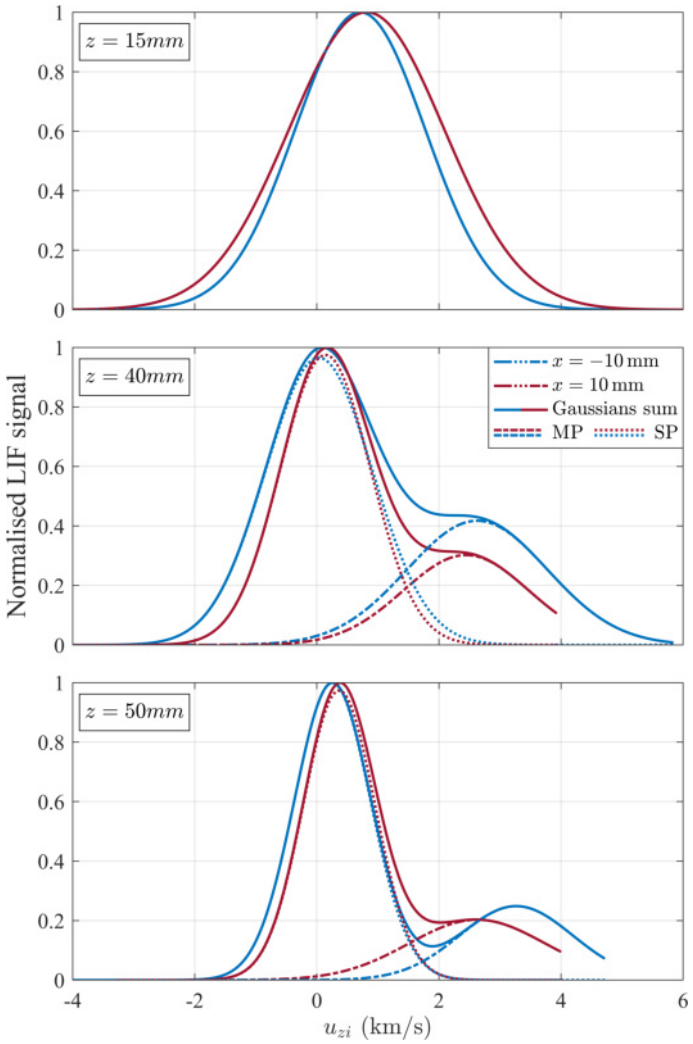

Figure 5.27: Xe II IVDFs for the ECRC2 made in the z-direction. From top to bottom, $z = 15\,\text{mm}$, $z = 40\,\text{mm}$ and $z = 50\,\text{mm}$.

ECRC2 z- and x- measurements

- **Relative density**

Figure 5.28(a) presents the normalized relative density of each population based on their Gaussian approximation integral in the z-direction for the ECRC2, accordingly to the aforementioned assumptions regarding the population sorting. The MP is predominant outside of the MA, being the only population probed above the MFL generated at $x = 75\,\text{mm}$. Moreover, this population is nearly absent (i.e. with a near-zero relative density) between the MFLs generated on both sides of the CT (i.e. $x = [57.75, 62.25]\,\text{mm}$), as well as below the MFL generated at $x = 45\,\text{mm}$. On the contrary, the SP is only probed below the MFL generated at $x = 75\,\text{mm}$.

Normalized relative density measurements have also been performed on the ECRC2 in the x-direction, as shown in Figure 5.28(b). The latter focuses in the normalized relative density of each population. Most measurements were conducted in the MA, where the SP is predominant. Moreover, considering that the relative density of the MP is lower than the SP one in the MA and a low u_{xi} for both populations, the possibility of the MP IVDF shadowed by the SP one should be taken into account.

Under the MFL generated at $x = 45\,\text{mm}$, the population sorting between the MP and the SP could present different interpretations. The plasma expansion from the sources indicates that the density in this region is weak in comparison with the region above the MFL of interest. As observed in Figure 5.28, the SP is believed to be predominant in this region. However, this interpretation based on continuity with surrounding measurements should be taken with caution.

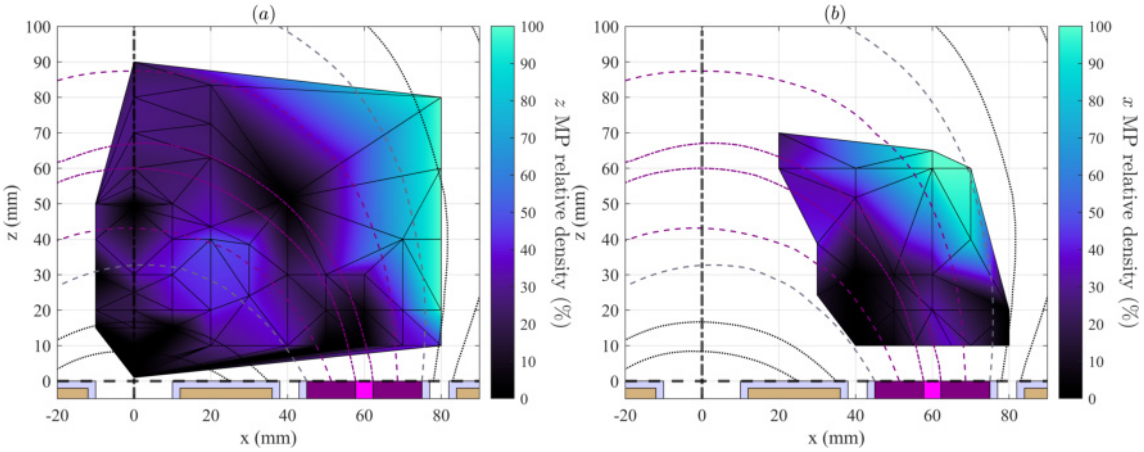

Figure 5.28: Xe II MP normalized relative density in the z-direction (a) and x-direction (b) for the ECRC2.

- **Velocity**

Figure 5.29(a) depicts $u_{zi,MP}$. An increase in $u_{zi,MP}$ can be seen from the origin to the furthest point probed ($[x = 80\,\text{mm}; z = 80\,\text{mm}]$), from $u_{zi,MP} = -2.95\,\text{km/s}$ to $u_{zi,MP} = 6.53\,\text{km/s}$. $u_{zi,MP}$ increases as a function of both the distance to the cluster exhaust plane and the distance to the symmetry plane. Negative $u_{zi,MP}$ can be found under the MFL generated at $x = 45\,\text{mm}$, close to the inner wall of the IC, with a minimum at $u_{zi,MP} = -2.95\,\text{km/s}$. This MFL acts as a separation with a null velocity. It would require only 6 eV of upstream electrostatic work on Xenon ions to reverse their z-direction motion. This is likely due to a localized axial electric field pointing upstream that develops from electron confinement on closed field lines[94]. In this region, the populations are very difficult to sort, so the conclusions drawn for the MP could be applied for the SP. The decision has been taken to attribute one peak to one population at each point based on continuity.

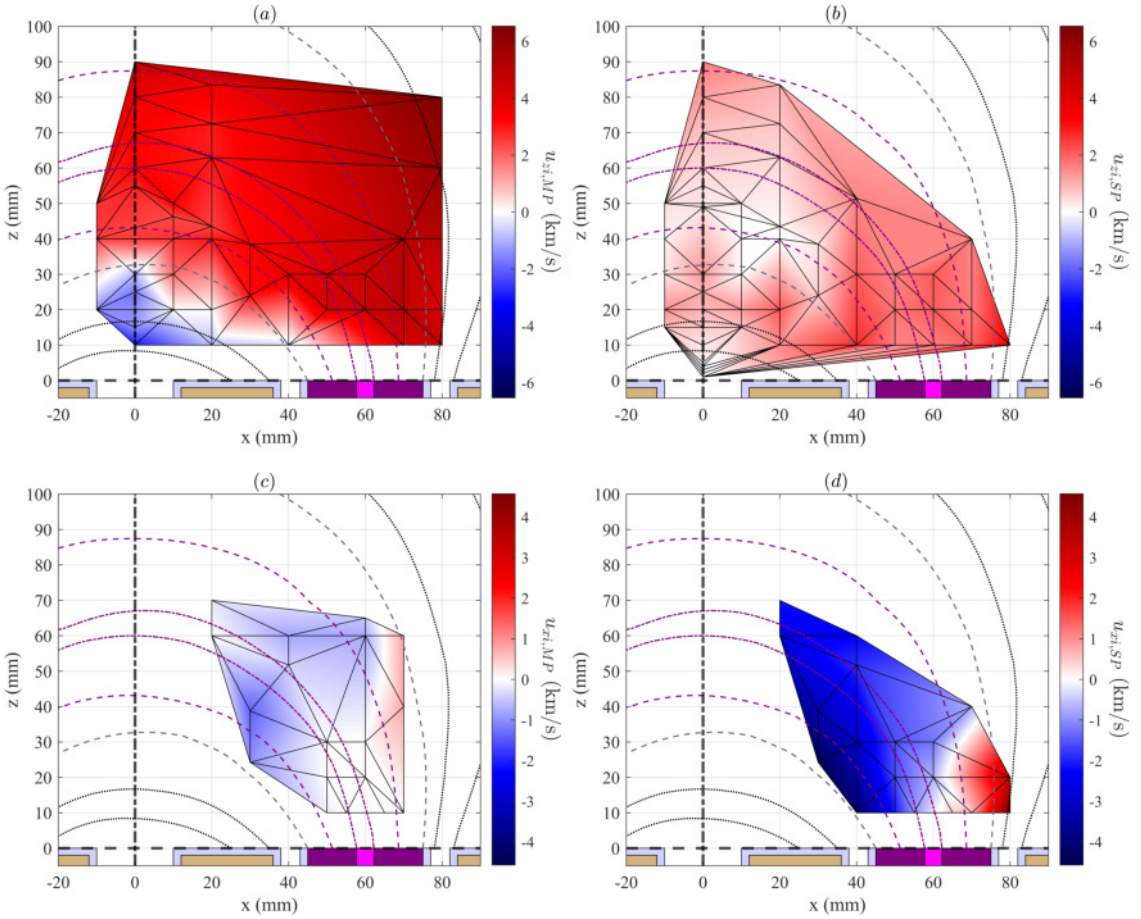

Figure 5.29: Xe II $u_{zi,MP}$ (a), $u_{zi,SP}$ (b), $u_{xi,MP}$ (c) and $u_{xi,SP}$ (d) ECRC2 colormaps.

Figure 5.29(b) focuses on $u_{zi,SP}$. It is expected for this population to have a lower most probable velocity in average due to its generation through the plume, at $\overline{u}_{zi,SP} = 0.92\,\text{km/s}$. $u_{zi,SP}$ increases along the distance from the origin. The maximum is reached at $[x = 80\,\text{mm}; z = 10\,\text{mm}]$ with 3.37 km/s. $u_{zi,SP}$ remains higher in front of the right source exhaust than close to the symmetry plane.

Figure 5.29(c) depicts $u_{xi,MP}$. It presents an average of $\overline{u}_{xi,MP} = -0.19\,\mathrm{km/s}$. A zero-velocity line is aligned with the CT. Ions on the left of this separation drift towards the cluster symmetry plane, while the ones generated on its right direct towards the external part of the ECRC2. Compared to Figure 5.29(a), it appears that $|u_{xi,MP}| \ll |u_{zi,MP}|$. This observation is coherent with the measurements made on the single source configuration.

Figure 5.29(d) focuses on $u_{xi,SP}$. $|u_{xi,SP}|$ increases along the distance from the zero velocity line. The maximum $|u_{xi,SP}|$ is found at $[x = 80\,\mathrm{mm}; z = 10\,\mathrm{mm}]$ with $4.57\,\mathrm{km/s}$. Ions populating the SP present a higher velocity in the x-direction than the MP ones. Unlike in Figure 5.29(c) for the MP, the zero-velocity line is not aligned on the CT. They drift faster towards the symmetry plane, following ϕ.

- **Temperature**

As for the single source configuration, the T_{zi} is determined for the ECRC2 for both populations. Figure 5.30(a) shows that the MP ion temperature remains near-constant in the z-direction with $\overline{T}_{zi,MP} = 1.45\,\mathrm{eV}$. A slight decrease can be observed along the distance from the symmetry plane and the exhaust plane. The lowest $T_{zi,MP}$ is found at $[x = 80\,\mathrm{mm}; z = 80\,\mathrm{mm}]$ with $T_{zi,MP} = 0.23\,\mathrm{eV}$.

$T_{zi,SP}$ in the z-direction is higher with respect to the MP one, as seen in Figure 5.30(b). From $x = -10\,\mathrm{mm}$ to $x = 10\,\mathrm{mm}$, it presents an average of $\overline{T}_{zi,SP} = 1.13\,\mathrm{eV}$. A higher temperature can be observed at $[x = -10\,\mathrm{mm}; z = 30\,\mathrm{mm}]$ with $T_{zi,SP} = 3.14\,\mathrm{eV}$ and $[x = 10\,\mathrm{mm}; z = 30\,\mathrm{mm}]$ with $T_{zi,SP} = 3.23\,\mathrm{eV}$. These points intersect with the MFL generated at $x = 45\,\mathrm{mm}$, along which some hot electrons are present. The SP generation process could explain the higher temperature in the z-direction. Indeed, electrons stuck in the MA would show a large energy distribution function. As this population is believed to be generated in the MA, it comprises a larger temperature.

The x-direction ion temperature in the ECRC2 for the MP is shown in Figure 5.30(c). In general, the ion temperature is lower in the x-direction than in the z-direction. As the MP is measured with a low relative density through the MA, it is complex to conclude upon the presence of higher temperature points—at $[x = 30\,\mathrm{mm}; z = 38.75\,\mathrm{mm}]$, $[x = 40\,\mathrm{mm}; z = 60\,\mathrm{mm}]$ and $[x = 60\,\mathrm{mm}; z = 20\,\mathrm{mm}]$ with $T_{xi,MP} \geq 1.5\,\mathrm{eV}$.

Figure 5.30(d) focuses on the ion temperature of the second population in the x-direction, $T_{xi,SP}$. The latter decreases along the distance with the symmetry plane and the exhaust plane, with a maximum reached at $T_{xi,SP} = 1.32\,\mathrm{eV}$ at $[x = 20\,\mathrm{mm}; z = 60\,\mathrm{mm}]$. This behavior is to be expected as this population is strongly impacted by potential dwells due to its relatively low velocity in the z-direction. Hence, the closer the measurement is to the symmetry plane, the higher $u_{xi,SP}$ and $T_{xi,SP}$.

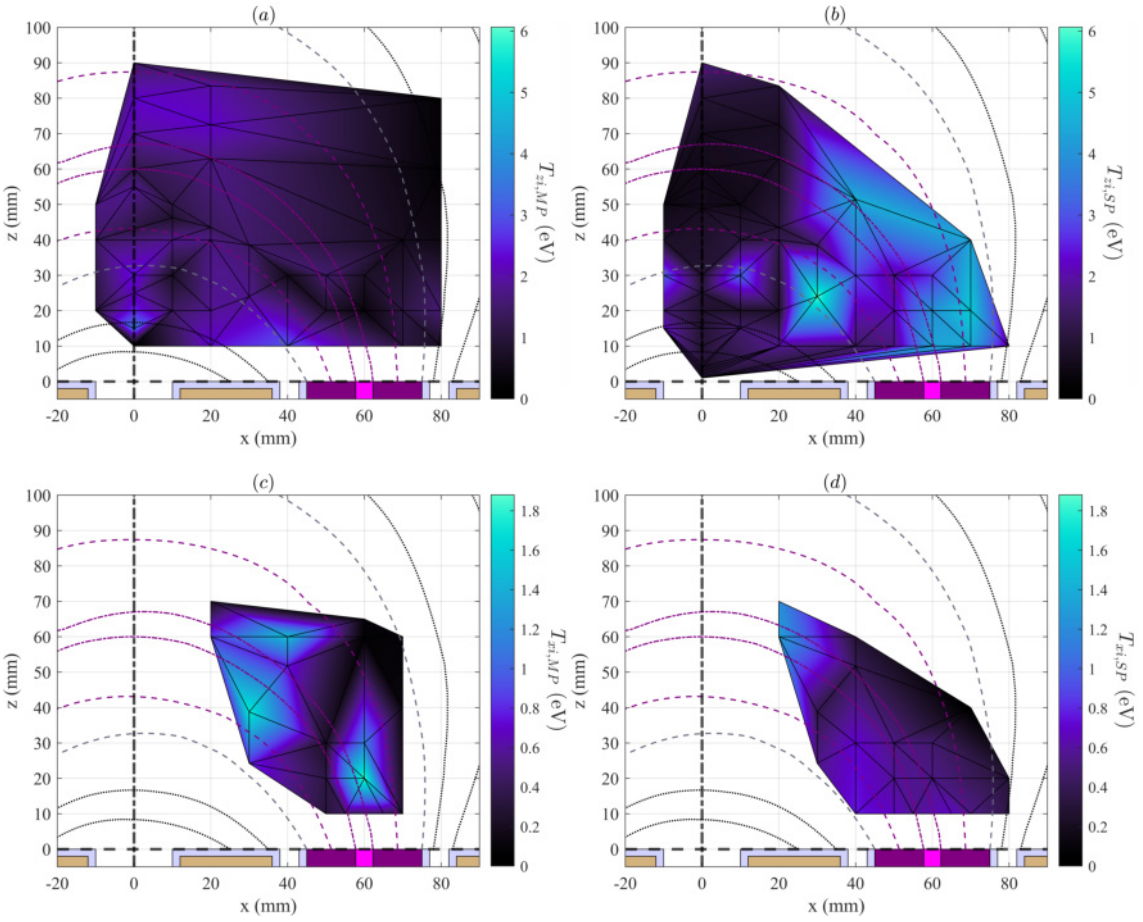

Figure 5.30: Xe II $T_{zi,MP}$ (a), $T_{zi,SP}$ (b), $T_{xi,MP}$ (c) and $T_{xi,SP}$ (d) ECRC2 colormaps.

ECRC2 total in-plane velocity

As for the single source configuration in Section 5.3.3, the in-plane velocity is determined through u_{zi} and u_{xi}: $\tilde{u}_i = \sqrt{u_{zi}^2 + u_{zi}^2}$. Figure 5.31(a) depicts the in-plane velocity of the MP. Figure 5.31(b) presents the MP local velocity vectors and ion streamlines. These latter remain straight in front of the left part of the source exhaust—i.e. $45 < x < 60\,\text{mm}$. For $x > 60\,\text{mm}$, a slight curvature can be seen towards the external part of the ECRC2. Ions probed for $x < 45\,\text{mm}$ are drifting towards the symmetry plane to straighten their trajectory in the z-direction for $z > 50\,\text{mm}$. This behavior could result from the influence of the plasma beam emanating from the opposite source. Electrons, which communicate rapidly along the closed field lines, establish a lateral potential gradient $E_x = -\partial\phi/\partial x$. On the inner side (for $x < 45\,\text{mm}$), it points toward the symmetry plane and imparts a small $u_{xi,MP}$ that tilts the paths inward. Farther out (for $x > 60\,\text{mm}$), the gradient reverses and produces the slight outward curvature seen near the external edge of the plume. The effect remains modest—as $||u_{xi,MP}|| \ll ||u_{zi,MP}||$ and the trajectories straighten once the gradient weakens downstream for $z \gtrsim 50\,\text{mm}$. A quick estimation shows that deflecting a $7{-}9\,\text{km/s}$ Xe^+ MP beam by $\delta u_x \sim 1{-}2\,\text{km/s}$

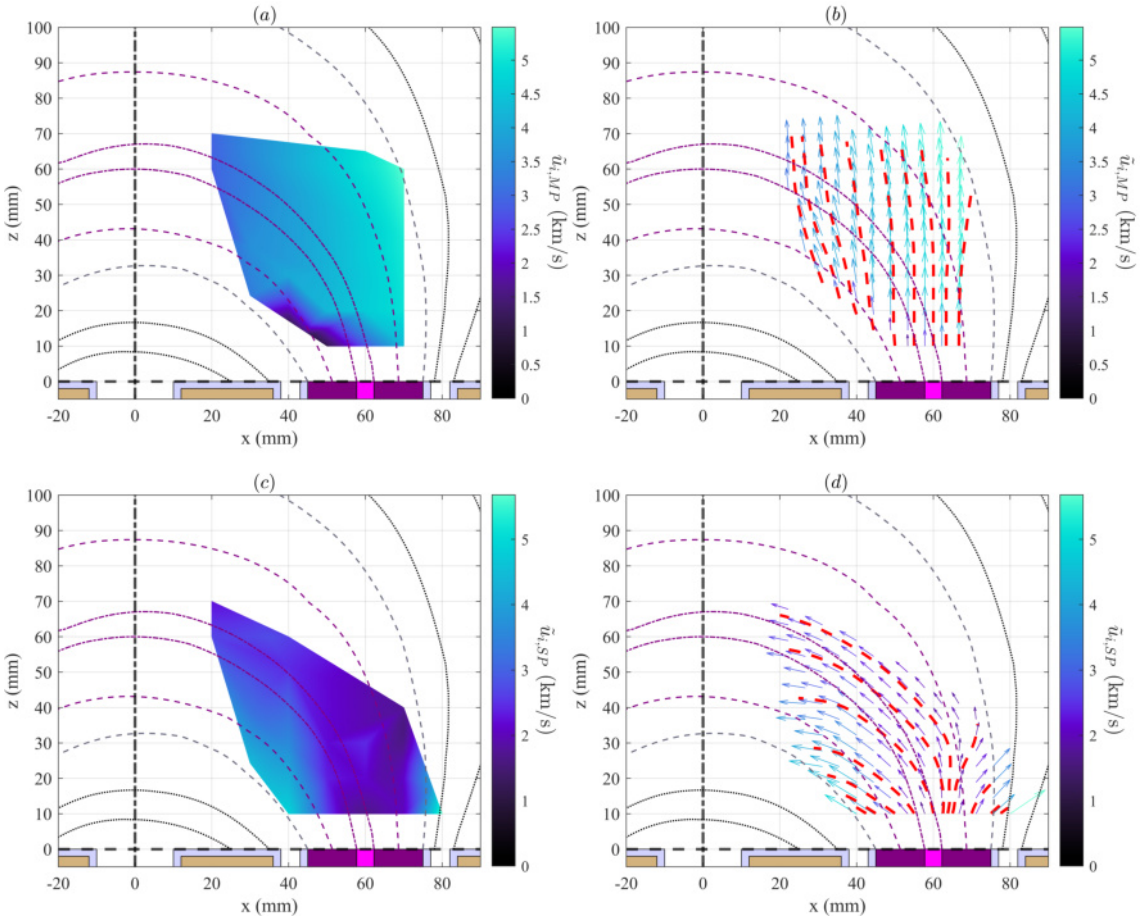

Figure 5.31: Xe II ECRC2 $\tilde{u}_{i,MP}$ colormap (a) and local velocity vectors and ion streamlines (b), $\tilde{u}_{i,SP}$ colormap (c) and local velocity vectors and ion streamlines (d).

over $L \sim 5{-}10\,\mathrm{cm}$ requires only a potential difference of $5{-}10\,\mathrm{V}$, consistent with the potential variations measured along the cluster symmetry plane. Some comparisons can be made upon the differences between the single source and the ECRC2 configurations regarding the MP ion trajectory:

- The closed-line magnetic topology seems to have a weaker impact on the ion trajectory than the classic diverging MN one.
- Ion trajectory straightening occurs much closer to the source exhaust plane in the ECRC2.
- Unlike in the single source configuration, the maximum in-plane velocity is not reached on the CT central axis in the ECRC2.

The SP in-plane velocity is presented in Figure 5.31(c). This population expansion is highly divergent, with the maximum in plane velocity found at $[x = 80\,\mathrm{mm}; z = 10\,\mathrm{mm}]$ with $\tilde{u}_{i,SP} = 5.68\,\mathrm{km/s}$. The in-plane velocity increases along the distance from the right source CT (i.e. $[x = 0\,\mathrm{mm}; z = 10\,\mathrm{mm}]$). The SP local

velocity vectors and ion streamlines are displayed in Figure 5.31(d). The ion trajectory follows the the MFLs. Even ions generated for $x > 60\,\text{mm}$ and originally directing to the external part of the ECRC2 drift in the direction of the symmetry plane. It is expected to have an analogous population of slow ions in the opposite direction near $x = 0\,\text{mm}$, coming from the other source. However, this population has not been probed near the symmetry plane because of the limited lifetime of the Xenon II in the probed metastable level.

5.4 Plasma expansions comparison between single source and ECRC2 configurations

Measurements performed on the single source configuration are coherent with expectations from a simple diverging MN. A MP is generated in the IC, to be expanded and accelerated through the plume by the ambipolar field. The SP is formed through ionization and CEX (Charge Exchange Collision) of the neutral background in the plume expansion, in particular near the MFLs originating from the CT sides. As the MF is purely divergent, the MP is predominant in the plume expansion. All ions are essentially unmagnetized and already detached from MFLs and see their trajectory straighten.

Even though the ECRC2 presents a completely different magnetic topology due to its closed-line nature, the same phenomena can be witnessed in its plume. The generation process of both populations remains the same as in the single source configuration. However, the predominancy of the SP in the MA with respect to the MP could be explained by different hypotheses. First of all, the increase in mass flow rate (with two sources in place of one) combined by the low energy efficiency of the sources could be responsible for a high neutral background density, favoring the emergence of a SP. In addition, high energy electrons might be confined in the MA, amplifying the ionization process. The MP can still be probed under the MFLs closing the sources (i.e. generated at $x = 75\,\text{mm}$), but with little relative density. This population still carries a comparable behavior in terms of velocity ($|u_{zi,MP}| \gg |u_{xi,MP}|$) as in the single source configuration. The $u_{xi,MP}$ is aligned for both configurations with the CT. However, the MP presents a less divergent ion trajectory in the closed-line MF than in the single source. Still, this behavior could be linked to both the MF and the opposite source influence. The SP ions Larmor radius increases along with the distance to the origin and is significantly higher than the diameter of the MNs ($r_{L,SP} > 4 \times r_{MN}$). Hence, they are not magnetized. Still, their low inertia in comparison to the MP makes them more responsive to the E-field. Hence, as the MA confines the electrons due to its closed-line nature, the SP ions seem to align with the MFLs through their expansion in the plume.

Unlike in the single source configuration, where the ion velocity field is relatively

homogeneous, the cluster configuration shows localized regions where ions exhibit distinct velocity patterns. These structured flow patterns suggest that the plasma potential landscape in the cluster is not a simple superposition of individual sources but rather a new, integrated field shaped by inter-source coupling. The cluster configuration can result in velocity anisotropy due to plume interaction, while the single source maintains a more isotropic expansion. Moreover, it also broadens the ion velocity distribution compared to the single source due to plume merging and CEX. This can be interpreted as cluster-induced plasma heating, which might affect thrust efficiency and divergence. The cluster configuration also increases the divergence due to plume-plume interactions, which might reduce propulsive efficiency.

Finally, the cluster configuration, while beneficial for thrust augmentation as two sources are combined, inherently introduces complex flow dynamics that can broaden velocity distributions, reduce collimation, and generate a high density SP populations. In contrast, the single source maintains a more predictable collimated plume, with fewer kinetic irregularities. Still, the cluster configuration does not form a strong dipole moment interacting with the ambient MF (like the geomagnetic field) to produce a torque on a spacecraft.

5.5 LIF/electrostatic probes measurements confrontation

The sorting algorithm used for the LIF measurements has been applied to the RPA curves shown in Figure 5.13. The single population fitting is the most probable for $\alpha = |35\text{deg}|$. Single and two populations fittings of equivalent least square errors can be found for $\alpha = 6\text{deg}$. However, the single population fitting is more probable due to the most probable energy probed at $E_i = 27.25\,\text{eV}$. The most probable energy of the MP ions aligned with $\alpha = 6\text{deg}$ is determined with the LIF measurements at 10.76 eV, nearly tens times more than the SP ones. As the RPA is placed at 380 mm from the cluster origin, the MP is considered to be the population reaching it. Hence, the single-peak measurements obtained by the RPA shows that the SP does not reach the probe in a high enough density to be measured. They could be blocked in the MA, not because they are magnetized in any way, but because of their trajectory is bent by the electric field. Their high divergence could also explain their low density in this region. A potential drop of nearly 17 V should be measured between $z = 50\,\text{mm}$ (last position where the ion MP most probable energy can be determined) and $z = 380\,\text{mm}$. Using ϕ from the LP measurements along the symmetry plane for $\dot{m}_{Xe,total} = 5\,\text{sccm}$ and $P_{MW,total} = 100\,\text{W}$, a drop of 10 V can be determined. However, the RPA measurements have been made 40 mm away from the symmetry plane. Hence, the coherence between the RPA and the LIF measurements should be taken with caution as no measurements of the potential

have been made on the $x = 40\,\text{mm}$ line. Still, the RPA measurements are considered compatible with the LIF measurements.

5.6 ECRC2 conclusion

The development and characterization of the ECRC2 prototype mark a significant step forward in the study of interconnected plumes in clustered ECRTs. Addressing the operational limitations of the ECRC1, the ECRC2 integrates permanent magnets, leading to a prolonged operational time. Through the application of 2D-LIF spectroscopy and electrostatic probe measurements, the plasma characteristics, velocity distributions and population sorting of the ions within the plume have been thoroughly investigated. The potential forming in the closed-line magnetic topology significantly influences ion trajectories, leading to distinct behaviors between the MP and the SP. The MP is generated within the ionization chamber and undergoes acceleration due to the ambipolar field, while the SP results from neutral background ionization predominantly within the closed-line MA. The observed differences in velocity between these populations demonstrate the impact of the confined MF topology, which influences ion flow patterns compared to a single source configuration.

A comparison of LIF and electrostatic probe measurements confirms the consistency of the ion energy values across different diagnostic methods, despite spatial limitations in probe accessibility. The use of a sorting algorithm to distinguish ion populations has proven to be essential in characterizing the populations. Additionally, the symmetrical nature of the ECRC2 has been validated through comparative velocity measurements on either side of the symmetry plane.

While ECRC2 demonstrates a significant advancement in clustered ECRT configurations, certain limitations persist, such as the predominance of the SP. Still, it is yet to determine if the presence of the SP is inherent to the MA, due to a low optimisation of the sources or to the lack of clustering-aimed sources design. The restricted spatial resolution of LIF measurements and the challenges posed by closed-line MF on conventional probe diagnostics remain important limitations in the MA understanding.

Chapter 6

C-shaped magnetic arch thruster testing

6.1 MAT architecture

Following the patent made by Merino[56], a MAT (Magnetic Arch Thruster) prototype has been designed, assembled and tested. The shift from two distinct ECR-sources to a C-shaped thruster is motivated by various reasons. First, the presence of a MF (Magnetic Field) parallel to the walls and the removal of the rear-wall can lead up to a decrease in plasma losses to the walls up to 50%[55]. Moreover, the MA (Magnetic Arch) present outside of the C-shaped thruster represents a continuity of the MF present in the latter.

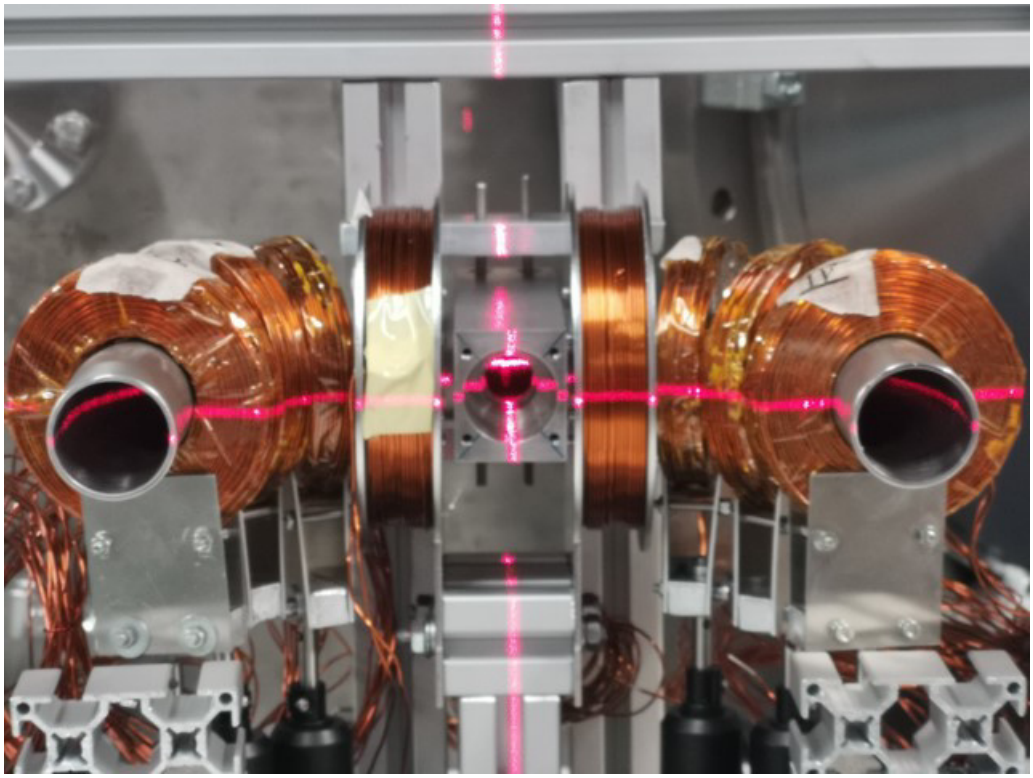

Figure 6.1: Alignment of the MAT in assembly. Only the IC, CCs and PCs are mounted.

The MAT can be described as a C-shape ECR thruster, where the plasma is generated at the center of the C-shape tube to be guided and expanded at both ends of the IC (Ionisation Chamber). Figure 3.1 depicts the general aspect of the thruster. The IC is made of a single non-magnetic stainless steel tube with an inner radius of L. The curvature is defined by the aspect ratio AR. Chapter 3 focuses on the design and the characterisation of the elements composing the MAT. The MAT can be decomposed through the coils and the IC, as shown in Figure 3.1. The IC is split into separated sections with a central connector joining two right-angle tubes. The ionization occurs in the central connector, where the PC generates the resonance MF. Moreover, the MW (Micro Wave) are injected through a CT (Coaxial Termination). The TL (Transmission Line) preceding the CT has been discussed in Section 3.2. The propellant is injected through the central connector, facing the MW injection. A picture of the MAT in assembly can be observed in Figure 6.1. The MAT have been designed, assembled and tested within the UC3M EP2 laboratory in Madrid, Spain.

6.2 MAT experimental campaign

6.2.1 First experimental campaign

The first part of the MAT experimental campaign occurred in the Laboratory of Space Propulsion of Universidad Carlos III de Madrid, Leganés, Spain. More details about the facility can be found in previous works [51], [58], [82] . The grounded and floating versions of the MAT had been tested during this campaign. The difference between these versions depends on the presence of the C2Ws (Coaxial-to-Waveguide adapters). After all the subsystems of the prototype had been checked, the thruster was assembled on its Bosch profiles frame to be set in the vacuum chamber. The floating version of the MAT was installed for the first attempts. Two operating procedures were defined for the first ignition:

- Starting procedure:
  - MWG (Micro Wave Generator) on Stand-by mode with the set power.
  - Possible MW leaks measured.
  - Mass flow rate set to the maximum: 100 sccm.
  - MWG activated.
  - Possible MW leaks measured.
  - PCs turned on.
  - Segmented coils turned on.
  - MNs turned on.
  - Possible MW leaks measured.

– Stopping procedure:
  – PCs turned off.
  – Segmented coils turned off.
  – MNs turned off.
  – MWG set on Stand-by mode.
  – Possible MW leaks measured.
  – Mass flow rate set to the 0 sccm.
  – Deactivation of the MWG Stand-by mode.
  – Possible MW leaks measured.

Coils were powered by their optimal current, taking into account the corrective factor previously determined.

– $MN1$ & $MN2$: 5.19 A.
– $PC1$ & $PC2$: 7 A.
– $CC1$ & $CC2$: 6.7 A.

Only a visual confirmation could tell if plasma is generated during the first ignition. The MW power has been increased through the ignition attempts from 10 W to 500 W. However, no ignition has been realized, regardless of the increase in the MW power. Several different mass flow rates have also been tested. The coils configuration has been changed to focus on the 875 G resonance line at the centerpart of the IC. Only the PCs were turned on with a current standing in a $8 - 9$ A band. Still, ignition had not occurred. Moreover, the pressure graph suggested that an element was emitting gas inside the vacuum chamber, as the cryogenic panels could not bring the pressure down as usual. The decision was taken to stop the experiments and open the vacuum chamber to inspect the thruster.

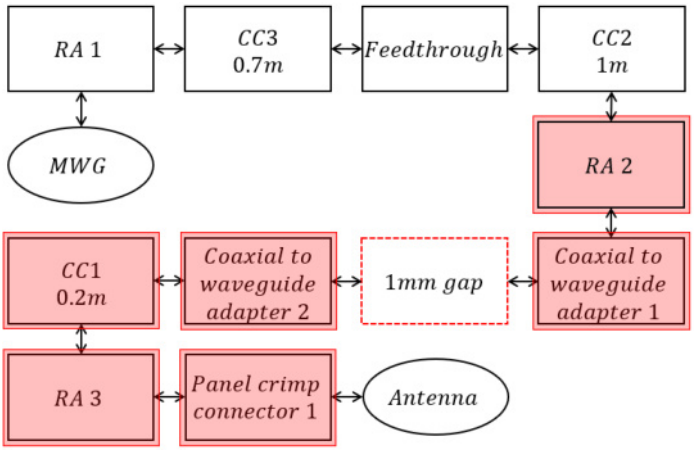

Figure 6.2: Configuration of the full TL for the floating version during the first campaign, with damaged elements highlighted in red.

After the inspection, the power appeared not to be transmitted to the CT as its physical and electrical connection with the panel crimp connector's core was ineffective. The floating TL is shown in Figure 6.2. Indeed, the connection was only made by contact and not threaded. Thus, the power was not transmitted to the IC. Hence, plasma generation was impossible. As the power was not forwarded to the CT, it was dissipated in the TL elements close to it. Thus, as shown in Figures 6.3, the dielectric element of coaxial elements separating the core from the shield has been completely burnt.

Figure 6.3: 7-16 DIN coaxial connector of the C2W 1 (left) and connector of the CC1 (right) after the experience.

Coils	**Resistance** (Ω)
$MN1$	4.4
$MN2$	4.5
$PC1$	2.3
$PC2$	2.3
$CC1.1$ & $CC1.2$ & $CC1.3$	3.3
$CC2.1$ & $CC2.2$ & $CC2.3$	3.3

Table 6.1: Resistance of the coils after the ignition attempt.

Another ignition attempt took place, with a MW power of 100 W and a mass flow rate of 100 sccm. The TL was changed from floating to grounded. Coils resistance and integrity were checked, as shown in Table 6.1. The plasma was generated in the center part of the thruster. Its reflection in the metallic tubes of the IC could be seen, evidenced by the light emission that was visible from outside the vacuum chamber—see Figure 6.4. However, no visible plume was expanding out of the exhausts. The ignition lasted for a minute before stopping by itself. The stopping procedure was then followed. After this short and only ignition, other attempts were unsuccessful

regardless of the mass flow rate and power modifications. The pressure graph began to show signs of burning whilst MW power was increasing. Thus, attempts were stopped once again to expertise the thruster. Once again, the CT had disconnected from the core of the coaxial TL. The power was again dissipated among the TL, which explains the increase in pressure.

6.2.2 Second experimental campaign

The second part of the MAT experimental campaign occurred in the same facilities as the first one. The grounded and floating versions of the MAT had been tested during this campaign. The thruster CT has been significantly modified since the first attempts. Indeed, the main issue during the first campaign was determined to be the disconnection between the CT and the core of the coaxial TL. Thus, a new CT design has been proposed, as well as a different panel crimp connector. After several attempts, the thruster reached ignition for a second time. As for the first ignition, only the reflection of the plasma-emitted light inside the two elbows of the IC could be seen. Still, there was no evidence of light being emitted directly from the plume region, as usual with plasma thrusters. Plasma was only dense in the centerpart of the IC. The MW power was increased at each successful ignition attempt. From 50 W to 200 W, the plasma reflected seemed to be equally bright with the same color. However, from 200 W to 500 W, the plasma became brighter in color and luminosity, as seen in Figure 6.4.

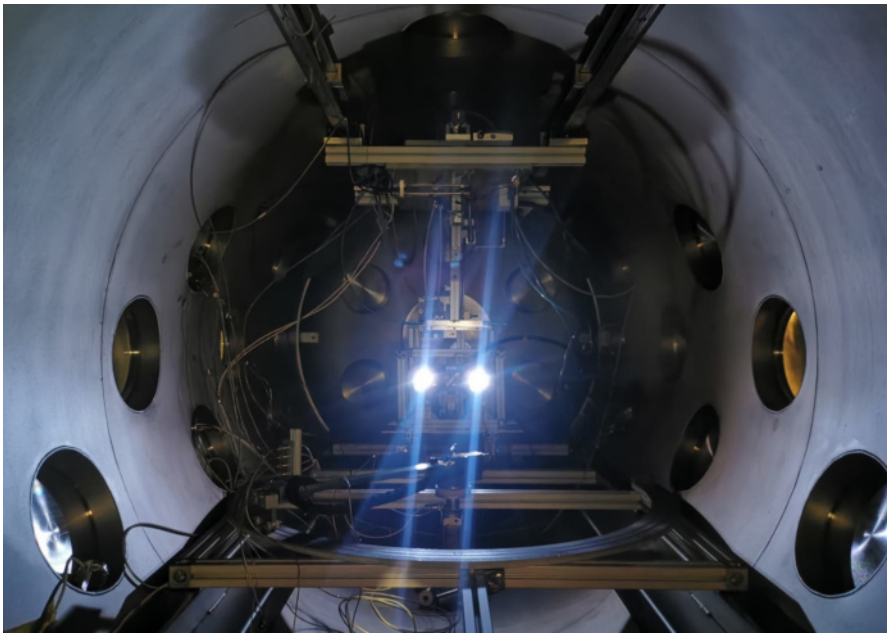

Figure 6.4: Photography of the grounded version of the MAT prototype firing.

Ignitions were also realized with the thruster in floating conditions. However, the plasma remained in the IC without forming any visible plume. When the mass

flow rate was lowered under 20 sccm, the thruster turned off itself. From 100 W to 200 W, the same brightening of the plasma was observed as for the modification from 200 W to 500 W with the grounded version. Still, there was no difference in the plasma aspect from 200 W to 500 W. However, the CT was hot enough to emit a glowing light reflecting in the IC. Several coils configurations have been tested with the grounded and the floating versions of the MAT. From these configurations, the following observations were made:

- Regardless of the modification of every parameter, no visible plasma plume came out of the thruster.
- The three sets of coils are needed to ignite the thruster.
- Coils are not necessary for the thruster to function. Indeed, coils were turned off one set at a time without stopping plasma generation. The PCs were turned off first, followed by the CCs to finish with the MNs. This indicates that the discharge can operate without the EC resonance.
- When the thruster is firing without coils, the plasma generation seems to move from the centre part to the middle of each elbow. Still, no plasma expansion could be seen.
- MNs have been turned back on when the thruster was firing without any applied MF. The resonance line was expected to move close enough to the exhausts for plasma to be generated there and to form a plume. However, even though the plasma generation area was indeed moved closer to the exits of the IC, no expansion could be observed with the naked eye, indicating that the plasma was very tenuous.

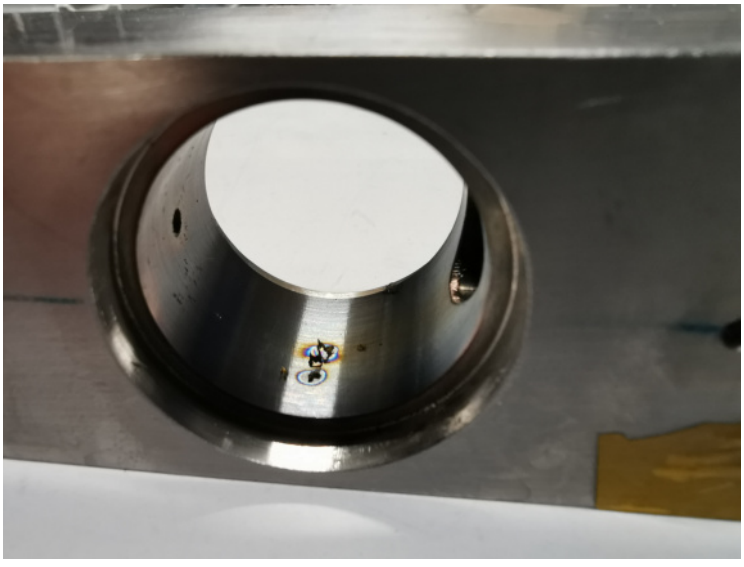

Figure 6.5: Photography of the central connector of the IC after the campaign.

Only the central part of the IC and the CT have been damaged, as seen in Figure 6.5. It appeared that the CT had reached a temperature critical for some contamination/damage to be found at the bottom of the IC.

6.3 MAT conclusion

The development of the MAT represented a challenge as the first prototype of the MA concept. Indeed, the MAT main flaw lies in the generation of ions localised at the central connector of its IC. Nevertheless, even though no visual confirmation could be done during the experiments, no probe was used to determine if some ions escaped the IC. Moreover, coils represented a great limitation in the firing time. They could only be turned on for a few minutes to prevent overheating. As no convection occurs in a vacuum chamber, only radiative and conductive processes can cool them down. In addition to this time limitation, they overweighted in the tradeoff balance with the IC dimensions. Their size directly induced a consequent increase in the IC length.

In addition, three other main hypotheses are taken into account to explain the thruster malfunction. First of all, the inner part of the C-shaped IC is made out of stainless steel. The use of a metal could have allowed the short-circuiting of the plasma current to the walls through the IC. Moreover, the low ion magnetization is believed to be responsible for a vast majority of the generated ions to impact the walls rather than being guided out. In regard of the damages seen through the TL and in the central connector of the IC, it appears that problems in the TL and power transmission may have affected the capability to generate a dense plasma.

The MAT needs to be reworked in order to assess the absence of plume expansion cause. To begin with, changing the inner material of the IC to a dielectric one could help prevent the short-circuiting of the plasma current to the walls. Before a complex C-shaped tube is realized in ceramics or quartz, a ceramic-based liquid solution covering the inside of the IC would be a first step. Moreover, the MF in the elbows of the C-shaped IC is too weak for the Xenon ions to be magnetized. An improvement of the magnetic topology in terms of intensity might be a solution to bend the ion trajectory through the curvature of the IC. In addition, the use of a lighter propellant could be a viable solution since the Larmor radius (i.e. the magnetization of the ions) depends on the ion mass. The application of these improvements is a first step in determining the viability of the MAT. However, the lack of time of this thesis made it impossible to improve the MAT or to realize electrostatic probes measurements on the latter.

Chapter 7

Conclusion

7.1 Main contributions

Implementation of the Magnetic Arch Configuration

Three prototypes (ECRC1, ECRC2 and MAT) have been designed through this thesis. They represent the first MA (Magnetic Arch) type thrusters to be developed. For every prototype, a working MW (Micro Wave) frequency of 2.45 GHz has been chosen due to the availability of commercial components, regulatory compatibility, and established experience in ECRTs (Electron Cyclotron Resonance Thrusters). At this frequency, the corresponding ECR condition requires a MF (Magnetic Field) of 875 G. The power varied through the experimental campaigns from 50 W to 500 W. The ECRC1 (Electron Cyclotron Resonance Cluster 1) represents the first attempt to characterise an external magnetic arch, with two simple ECR sources with opposed polarity using single-point gas injection and electromagnets. The ECRC2 (Electron Cyclotron Resonance Cluster 2) finds its roots in the ECRC1, with an improved IC (Ionisation Chamber) thanks to the prechamber and a longer operation time thanks to the use of permanent magnets. Finally, the MAT (Magnetic Arch Thruster) represents the most complex prototype with its C-shaped IC and the use of three sets of electromagnets to generate a MF permanently parallel to the IC walls.

RPA measurements in the ECRC1

The plume characterisation of the ECRC1 has been performed with a RPA (Retarding Potential Analyser) through different configurations of the thruster in the EP2 laboratory of the UC3M in Madrid, Spain. The main insights from this experimental work are as follows:

– The peak ion energies in the single source S1 configuration ranged between $60 - 70\,\text{eV}$, consistent with a plasma of $T_e \approx 10 - 15\,\text{eV}$ accelerated through a MN (Magnetic Nozzle). In contrast, the DB (same-polarity) and DA (MA) cluster configurations show broader IEDFs (Ion Energy Distribution Functions) with more significant low-energy contributions—especially in the DA

configuration—which points to enhanced production or retention of slow ions near the source exit.

- The ion most probable energy E_i decreased across the configurations: $60 - 70\,\text{eV}$ for S1, $\sim 59\,\text{eV}$ for DB and $\sim 45\,\text{eV}$ for DA. The drop in energy in DA is attributed to electrostatic drag along the central part of the MA, where the MFLs (Magnetic Field Lines) are nearly orthogonal to the plasma flow. The presence of paramagnetic current effects further contributes to the small negative magnetic thrust, leading to deceleration of ions prior to plume formation.

- The S1 and DB configurations exhibited structured ion flux profiles, while S0 and D0 produced flatter, lower flux distributions. This confirms that magnetic confinement substantially reduces the divergence. In the DA configuration, despite a drop in E_i, the ion current density remained higher than in the DB, reflecting better plasma interconnectivity across sources.

- In the DA and DB configurations, mutual influence between the two sources disrupted internal magnetic symmetry, leading to partially tilted fields. This likely increased wall losses and reduced electron temperature, impacting downstream ion energies. Such magnetic cross-talk must be minimized or controlled in future cluster designs to enhance energetic efficiency.

- The area expansion ratio in the final magnetic tube of the DA and DB configurations was lower than that in the S1 one, reducing the acceleration space. Thus, optimization of expansion geometry remains a crucial design parameter to recover energy performance while leveraging topological advantages of MAs.

- The signal-to-noise ratio was lower in the cluster configurations, especially the DA one. This suggests the need for improved alignment and shielding in complex topologies, or alternative diagnostic strategies when assessing weakly collimated beams or merged plumes.

Electrostatic probes and Laser induced fluorescence measurements in the ECRC2

Through two experimental campaigns, the ECRC2 has been characterized by means of electrostatic probes and LIF (Laser Induced Fluorescence) measurements. The ECRC2 is an evolution of the ECRC1 using a combination of permanent magnets and electromagnets with a improved IC. The first experimental campaign, which focuses on electrostatic probes, has been performed in the EP2 laboratory of the UC3M in Madrid, Spain. A LP (Langmuir Probe), a FC (Faraday Cup) and a RPA have been used to determine the plasma characteristics through the plume expansion. The second experimental campaign has been carried out during a research stay in

the ICARE laboratory of Orléans CRNs, France. 2D LIF measurements have been performed on both the ECRC2 and a single source composing the latter.

- LP measurements along the MA revealed a spatially dependent evolution of the polytropic index γ, indicating two distinct thermodynamic regimes. After the MFL closing the external boundaries of the ICs ($z = 75 - 150\,\mathrm{mm}$), $\gamma \approx 1.2$, consistent with a near-isothermal expansion and effective electron energy homogenization along closed field lines. In the far field ($z = 150 - 300\,\mathrm{mm}$), γ increased to $1.4 - 1.8$, marking the transition to a more collisionless, adiabatic-like expansion.

- FC scans confirmed an increase in ion current density with power and mass flow. At $\dot{m}_{Xe,total} = 10\,\mathrm{sccm}$ and $P_{MW,total} = 200\,\mathrm{W}$, j reached over $1.2\,\mathrm{mA/cm^2}$, indicating strong beam formation. RPA measurements provided a clear scaling of the most probable ion most probable energy E_i with the power to mass flow ratio, validating the expected trend $E_i \propto (P/\dot{m})^{4/3}$. Moreover, angular scans revealed a mild asymmetry in the energy distribution across the symmetry plane.

- 2D-LIF measurements allowed full reconstruction of ion velocity vector fields. After Zeeman and Paschen-Back effects were ruled out by the use of fluorescence lineshape modeling for every LIF measurements, dual-Gaussian fittings of the Xe II 834.7 nm transition revealed two distinct ion populations: a Main Population (MP) with high axial velocity and a Second Population (SP) with lower axial velocity. The MP is believed to be generated in the IC, when the SP should result from CEX and ionisation through the plume expansion—due to its predominance below the MFL closing the external boundaries of the ICs.

- The 2D LIF-derived velocity vector fields revealed a clear distinction between the MP and the SP ions in terms of trajectory and field interaction. MP ions exhibited quasi-linear, field-line-crossing trajectories, largely unaffected by the arch curvature—indicative of high inertia and dominant initial momentum from their source. In contrast, SP ions showed curved trajectories bending toward the symmetry plane, which suggests that electrostatic forces act more strongly on these lower-energy ions due to their reduced inertia. This curvature is aligned with the electric potential profile measured by LPs, supporting the view that SP ions undergo additional E×B or ambipolar-driven drift.

- The spatial mapping shows that the MA not only guides the plasma but modifies its internal structure—flattening velocity gradients and stabilizing directionality. This opens the door to using magnetic topology not just for confinement, but for plume shaping and angular momentum control, possibly enabling low-thrust vectoring.

C-shaped magnetic arch thruster testing

The MAT represents the first and only thruster combining the MA and a C-shaped IC. The MF is parallel to the walls through the IC, with gas and power injection made in the central part of the latter. The inner magnetic topology is supported by three independent coil sets. Two experimental campaigns have been realised within the EP2 laboratory of the UC3M in Madrid, Spain. The first MAT ignition campaign was unsuccessful because of a flawed CT (Coaxial Termination) connection. The second campaign incorporated a redesigned CT. Plasma ignition was achieved, but only inside the central region of the IC. No visible plume was formed outside of the IC, even at powers up to 500 W. Optical feedback showed only reflections of the glow in the chamber elbows, confirming confinement but limited expansion. The metallic nature of the IC could have allowed the short-circuiting of the plasma current to the walls. Moreover, the low ion magnetization is believed to be responsible for a vast majority of the generated ions to impact the walls rather than being guided out.

7.2 Future lines of research

This thesis has been motivated by the will to innovate within the EP (Electric Propulsion) field with a new approach for the classic ECRTs, in particular to study clustering strategies and the novel magnetic arch topology for plasma acceleration. The MA represents an alternative topology which should be investigated deeper to be improved. The plasma characterisation of the ECRC1 and the ECRC2 motivates the viability of this topology. Still, the transition from the ECRC2 to the MAT appeared to be harder than expected, as no visible plasma plume could be witnessed. Nevertheless, this thesis has contributed to pave the way for further studies on the new MA topology. Some axis of improvements are listed below:

- A study of the ECRTs optimisation could provide a first important and useful step. Indeed, this thesis aimed mainly to reach a MA without giving much consideration about the sources optimisation. Thus, better performances might be reached with optimised ECRTs in the cluster configuration than in the single source one.

- Many degrees of freedom remain to be evaluated on both a two-ECR sources like thruster or on the MAT. The impact from the sources exhaust separation and the relative tilt angles of these is still unknown. They could impact greatly on the thruster performances and behavior. Indeed, these parameters directly influence plume merging, divergence, and energy uniformity, and could lead to optimal conditions for clustered ECRTs. Moreover, a parametric analysis upon the MNs current could benefit to determine the best MF topology associated with an optimal divergence efficiency.

– The clustering of more than two ECRTs could be of interested to determine the best configuration. Indeed, only two ECRTs have been used in this thesis based on the MA concept. Still, with a reworked magnetic field adapted to the number of ECRTs involved in the cluster, it would be possible to achieve clusters with more inter-connected sources, increasing the propulsive capacity.

– The central region of the MA, where paramagnetic electron currents and perpendicular field lines induce deceleration, requires higher-resolution diagnostics. This includes localized potential mapping and optical spectroscopy to assess charge exchange, recombination, and ion thermalization phenomena. Future campaigns could explore non-intrusive diagnostics such as emission spectroscopy, filtered imaging, or even Thomson scattering, to estimate EEDF evolution, power deposition profiles, and plasma-wall interactions without perturbing the discharge.

– The LIF measurements revealed two ion populations with distinct behaviors under the same field. Even though simulations have already been performed on the MA[72], further development of kinetic or PIC models and multi-population fluid solvers, as well as hybrid codes could help resolve their origin, transport paths, and sensitivity to field gradients—especially in merged plume zones.

– While energy and current densities have been well-characterized, as well as ion trajectories, future work should target direct thrust measurement campaigns to establish a performance benchmark for the MA configuration.

– As detailed in Section 6.3, the MAT needs to be reworked and improved in order to achieve plasma expansion. The use of dielectric material in the IC, a stronger MF or lighter gases could represent starting points to determine the viability of a C-shape thruster.

Bibliography

[1] G. Sutton and O. Biblarz, *Rocket propulsion elements*. John Wiley & Sons, 2010.

[2] H. Arbit, S. Clapp, and C. Nagai, "Lithium-fluorine-hydrogen propellant investigation final report," Tech. Rep., 1970.

[3] R. Jahn, *Physics of Electric Propulsion*. Dover, 2006.

[4] D. Goebel, "Analytical discharge model for RF ion thrusters," *IEEE Transactions on Plasma Science*, vol. 36, no. 5, pp. 2111–2121, 2008.

[5] E. Choueiri, "A critical history of electric propulsion: The first 50 years (1906-1956)," *Journal of Propulsion and Power*, vol. 20, no. 2, pp. 193–203, 2004.

[6] D. M. Goebel and I. Katz, *Fundamentals of Electric Propulsion: Ion and Hall Thrusters*. JPL, 2008, p. 493.

[7] V. Kim, "Main physical features and processes determining the performance of stationary plasma thrusters," *J. Propulsion Power*, vol. 14, no. 5, pp. 736–743, 1998.

[8] A. Morozov and V. Savelyev, "Fundamentals of stationary plasma thruster theory," in *Reviews of Plasma Physics, Vol. 21*, New York: Kluwer Academic, 2000.

[9] K. Dannenmayer and S. Mazouffre, "Elementary scaling relations for Hall effect thrusters," *Journal of Propulsion and Power*, vol. 27, no. 1, 2011.

[10] S. Mazouffre, "Electric propulsion for satellites and spacecraft: Established technologies and novel approaches," *Plasma Sources Science and Technology*, vol. 25, no. 3, p. 033 002, 2016. DOI: 10.1088/0963-0252/25/3/033002.

[11] A. Bapat, P. B. Salunkhe, and A. V. Patil, "Hall-effect thrusters for deep-space missions: A review," *IEEE Transactions on Plasma Science*, vol. 50, no. 2, pp. 189–202, 2022.

[12] D. B. Miller and E. F. Gibbons, "Experiments with an electron cyclotron resonance plasma accelerator," *AIAA Journal*, vol. 2, no. 1, pp. 35–41, Jan. 1964. DOI: 10.2514/3.2210. [Online]. Available: https://doi.org/10.2514/3.2210.

[13] G. Crimi, A. Eckert, and D. Miller, "Microwave driven magnetic plasma accelerator studies (cyclops)," General Electric Company, Space Sciences Laboratory, Missile and Space Division, Tech. Rep., 1967.

[14] H. Kosmahl, D. Miller, and G. Bethke, "Plasma acceleration with microwaves near cyclotron resonance," *Journal of Applied Physics*, vol. 38, no. 12, pp. 4576–4582, 1967.

[15] D. Kaufman and D. Goodwin, "Plume characteristics of an ecr plasma thruster," in *27th International Electric Propulsion Conference*, 1993.

[16] J. Sercel, "An experimental and theoretical study of the ECR plasma engine," Ph.D. dissertation, California Institute of Technology, 1993.

[17] M. Nagatomo, "Plasma acceleration by high frequency electromagnetic wave in staticmagnetic field gradient," in *6th Electric Propulsion and Plasmadynamics Conference*, American Institute of Aeronautics and Astronautics, Sep. 1967, p. 660. DOI: 10.2514/6.1967-660. [Online]. Available: https://doi.org/10.2514/6.1967-660.

[18] E. B. Hooper, M. A. Fergusson, M. A. Makowski, B. W. Stallard, and J. L. Power, "Analysis and experiments of a whistler-wave plasma thruster," in *International Electric Propulsion Conference*, ser. IEPC-93-038, Seattle, Washington (US), 1993.

[19] E. Bickford Hooper, B. W. Stallard, and M. A. Makowski, "Whistler wave driven plasma thruster," in *AIP Conference Proceedings*, ser. 271, AIP, AIP Publishing LLC, 1993, pp. 1419–1424. DOI: 10.1063/1.43245. [Online]. Available: https://doi.org/10.1063/1.43245.

[20] B. W. Stallard, E. B. Hooper, and J. L. Power, "Whistler-driven electron-cyclotron-resoncance-heated thruster: Experimental status," *Journal of Propulsion and Power*, vol. 12, no. 4, pp. 814–816, 1996.

[21] T. Kammash and M. J. Lee, "Gasdynamic fusion propulsion system for space exploration," *Journal of Propulsion and Power*, vol. 11, no. 3, pp. 443–440, 1995.

[22] R. Tang, "Study of the gasdynamic mirror (gdm) propulsion system," Ph.D. dissertation, Michigan State University, 2011.

[23] R. Tang, A. D. Gallimore, and T. Kammash, "Design and results of a microwave-driven gasdynamic mirror experiment," *Journal of Propulsion and Power*, vol. 29, no. 3, pp. 507–519, 2013.

[24] J. J. Brainerd and A. Reisz, "Electron-cyclotron resonance propulsion," in *46th AIAA/ASME/SAE/ASEE Joint Propulsion Conference, Nashville, TN*, ser. AIAA 2010-6597, 2010.

[25] W. Ohmichi and H. Kuninaka, "Performance degradation of a spacecraft electron cyclotron resonance neutralizer and its mitigation," *Journal of Propulsion and Power*, vol. 30, no. 5, pp. 1368–1372, 2014.

[26] T. Morishita, R. Tsukizaki, K. Nishiyama, and H. Kuninaka, "Plasma parameters measured inside and outside a microwave-discharge-based plasma cathode using laser-induced fluorescence spectroscopy," *Journal of Applied Physics*, vol. 131, no. 1, 2022.

[27] H. Kuninaka and S. Satori, "Development and demonstration of a cathodeless electron cyclotron resonance ion thruster," *Journal of Propulsion and Power*, vol. 14, no. 6, pp. 1022–1026, 1998.

[28] K. Toki, H. Kuninaka, K. Nishiyama, Y. Shimizu, and I. Funaki, "Technological readiness of microwave ion engine system for muses-c mission," in *27th International Electric Propulsion Conference, IEPC-01-174*, 2001.

[29] H. Kuninaka, K. Nishiyama, I. Funaki, T. Yamada, Y. Shimizu, and J. Kawaguchi, "Powered flight of electron cyclotron resonance ion engines on hayabusa explorer," *Journal of Propulsion and Power*, vol. 23, no. 3, pp. 544–551, 2007.

[30] K. Nishiyama, S. Hosoda, R. Tsukizaki, and H. Kuninaka, "In-flight operation of the hayabusa2 ion engine system on its way to rendezvous with asteroid 162173 ryugu," *Acta Astronautica*, vol. 166, pp. 69–77, 2020.

[31] H. Kuninaka, K. Nishiyama, Y. Shimizu, I. Funaki, and K. H., "Hayabusa asteroid explorer powered by ion engines on the way to earth," in *31th International Electric Propulsion Conference*, ser. IEPC-2009-267, Ann Arbor, MI, USA, 2009.

[32] G. D. Emsellem and S. Larigaldie, "Development of the electrodeless plasma thruster at high power: Investigations on the microwave-plasma coupling," in *Proc. 30th Int. Electric Propulsion Conf.(Florence, Italy)*, 2007.

[33] S. Larigaldie, *Propulseur plasmique et procédé de génération d'une poussée propulsive plasmique*, Brevet INPI, 2011.

[34] S. Larigaldie, *Plasma thruster and methode for generating a plasma propulsion thrust*, US 2015/0020502 A1, 2012.

[35] J. Jarrige, D. Packan, and P. Elias, "Développement et caractérisation d'un propulseur plasma ecra," in *ONERA Rapport Final n°RF 1120439 DMPH*, 2013.

[36] J. Jarrige, P. Elias, F. Cannat, and D. Packan, "Characterization of a coaxial ecr plasma thruster," in *44th AIAA Plasmadynamics and Lasers Conference, San Diego*, 2013.

[37] J. Jarrige, P.-Q. Elias, and D. Packan, "Measurement of ion acceleration in the magnetic nozzle of an ecr plasma thruster," in *Space Propulsion 2014*, 2014.

[38] T. Vialis, "Développement d'un propulseur plasma à résonance cyclotron électronique pour les satellites," Ph.D. dissertation, SORBONNE UNIVERSITE, 2018.

[39] F. Cannat, J. Jarrige, P. Elias, and D. Packan, "Experimental investigation of magnetic gradient influence in a coaxial ECR plasma thruster," in *Space Propulsion Conference, Cologne, Germany*, 2014.

[40] F. Cannat, J. Jarrige, T. Lafleur, P. Elias, and D. Packan, "Experimental geometry investigation of a coaxial ECR plasma thruster," in *Proc. of the 34th Int. Electric Propulsion Conf.(Kobe-Hyogo, Japan)*, 2015, pp. 2015–242.

[41] F. Cannat, T. Lafleur, J. Jarrige, P. Chabert, P. Elias, and D. Packan, "Optimization of a coaxial electron cyclotron resonance plasma thruster with an analytical model," *Physics of Plasmas*, vol. 22, no. 5, p. 053 503, 2015.

[42] F. Cannat, "Caractérisation et modélisation d'un propulseur plasma à résonance cyclotronique des électrons," Theses, Ecole doctorale de l'Ecole Polytechnique, Nov. 2015. [Online]. Available: https://pastel.archives-ouvertes.fr/tel-01271986.

[43] S. Peterschmitt and D. Packan, "Impact of the microwave coupling structure on an electron-cyclotron resonance thruster," *Journal of Propulsion and Power*, vol. 37, no. 6, pp. 806–815, 2021.

[44] V. Désangles *et al.*, "ECRA thruster advances: 30w and 200w prototypes latest performances," *Journal of Electric Propulsion*, vol. 2, no. 1, p. 10, 2023. DOI: 10.1007/s44205-023-00046-x.

[45] B. Wachs and B. Jorns, "Background pressure effects on ion dynamics in a low-power magnetic nozzle thruster," *Plasma Sources Science and Technology*, vol. 29, no. 4, p. 045 002, 2020.

[46] B. Wachs and B. Jorns, "Optimization of an ecr thruster using two frequency and pulsed waveforms," in *AIAA Propulsion and Energy 2021 Forum*, 2021, p. 3382.

[47] A. Sheppard and J. Little, "Scaling laws for electrodeless plasma propulsion with water vapor propellant," *Plasma Sources Science and Technology*, vol. 29, p. 045 007, 2020.

[48] A. Sheppard and J. Little, "Performance analysis of an electron cyclotron resonance thruster with various propellants," in *AIAA Propulsion and Energy 2021 Forum*, 2021, p. 3375.

[49] A. J. Sheppard and J. M. Little, "Performance analysis of an electron cyclotron resonance thruster with various propellants," *Journal of Propulsion and Power*, vol. 38, pp. 1–11, 2022. DOI: 10.2514/1.B38698.

[50] M. Inchingolo, J. Navarro-Cavallé, and M. Merino, "Design and plume characterization of a low-power circular waveguide coupled ecr thruster," in *5th International Workshop on Micropropulsion and CubeSats*, Toulouse (online), 2021.

[51] M. Inchingolo, J. Navarro-Cavallé, and M. Merino, "Direct thrust measurements of a circular waveguide electron cyclotron resonance thruster," in 37th *International Electric Propulsion Conference*, Boston, MA, June 19-23: Electric Rocket Propulsion Society, 2022.

[52] M. R. Inchingolo, M. Merino, and J. Navarro-Cavallé, "Plume characterization of a waveguide ecr thruster," *Journal of Applied Physics*, vol. 133, no. 11, p. 113 304, 2023. DOI: 10.1063/5.0138780.

[53] M. R. Inchingolo, M. Merino, M. Wijnen, and J. Navarro-Cavallé, "Thrust measurements of a waveguide electron cyclotron resonance thruster," *Journal of Applied Physics*, vol. 135, no. 9, Mar. 2024. DOI: 10.1063/5.0186778. [Online]. Available: https://doi.org/10.1063/5.0186778.

[54] M. Inchingolo, "Design, development, and characterization of a microwave electrodeless plasma thruster," Ph.D. dissertation, Universidad Carlos III de Madrid, Leganés, Spain, 2024.

[55] D. Berisford, R. D. Bengtson, and L. L. Raja, "Power balance and wall erosion measurements in a helicon plasma," *Physics of Plasmas*, vol. 17, no. 3, p. 033 503, 2010.

[56] M. Merino, *Motor espacial de plasma sin electrodos con geometría en U*, pat., PCT patent, Spanish Patent Office, Patent no. ES2733773, 2019.

[57] M. Wijnen, "Diagnostic methods for the characterization of a helicon plasma thruster," Ph.D. dissertation, Universidad Carlos III de Madrid, Leganés, Spain, 2022.

[58] C. Boyé, J. Navarro-Cavallé, and M. Merino, "Ion current and energy in the magnetic arch of a cluster of two ECR plasma sources," *Journal of Electric Propulsion*, vol. 4, no. 1, p. 10, Feb. 2025. DOI: 10.1007/s44205-025-00100-w. (visited on 02/26/2025).

[59] C. Boyé, J. Navarro-Cavallé, M. Merino, A. Lecervoisier, and S. Mazouffre, "Determining ion velocity in the interconnected plume of a cluster of two ecrts using 2d lif," in 38th *International Electric Propulsion Conference*, Toulouse, France, June 23-28: Electric Rocket Propulsion Society, 2024.

[60] K. Takahashi, T. Lafleur, C. Charles, P. Alexander, and R. Boswell, "Electron diamagnetic effect on axial force in an expanding plasma: Experiments and theory," *Physical Review Letters*, vol. 107, no. 23, p. 235 001, 2011. DOI: 10.1103/PhysRevLett.107.235001.

[61] T. Vialis, J. Jarrige, and D. Packan, "Separate measurements of magnetic and pressure thrust contributions in a magnetic nozzle electron cyclotron resonance plasma thruster," in *Space Propulsion Conference*, ser. 499, Seville, Spain, May 2018.

[62] B. Beal, A. Gallimore, and W. Hargus, "Preliminary plume characterization of a low-power Hall thruster cluster," in *Proc. 38th Joint Propulsion Conference, Indianapolis, IN*, ser. AIAA-2002-4251, 2002.

[63] W. Hargus Jr and G. Reed, "The air force clustered Hall thruster program," Tech. Rep., 2002.

[64] B. Beal, A. Gallimore, W. Hargus, and J. Haas, "Plasma properties in the plume of a Hall thruster cluster," *Journal of Propulsion and Power*, vol. 20, no. 6, pp. 985–991, 2004.

[65] R. Lobbia and A. Gallimore, "Evaluation and active control of clustered Hall thruster discharge oscillations," in *41st AIAA Joint Propulsion Conference and Exhibit, Tucson, Arizona, 2005. AIAA-2005*, vol. 3679, 2005.

[66] R. Lobbia and A. Gallimore, "Dynamic electromagnetic field measurements of clustered Hall thrusters," *42nd AIAA/ASME/SAE/ASEE Joint Propulsion Conference & Exhibit*, 2006.

[67] M. Walker and A. Gallimore, "Performance characteristics of a cluster of 5-kW laboratory Hall thrusters," *Journal of Propulsion and Power*, vol. 23, no. 1, pp. 35–43, 2007.

[68] M. Walker and A. Gallimore, "Hall thruster cluster operation with a shared cathode," *Journal of Propulsion and Power*, vol. 23, no. 3, pp. 528–536, 2007.

[69] M. Merino, D. García-Lahuerta, C. Boyé, J. Navarro-Cavallé, and E. Ahedo, "Preliminary model of the plasma expansion in a magnetic arch thruster (and overview of the first prototype)," in 37^{th} *International Electric Propulsion Conference*, Boston, MA, June 19-23: Electric Rocket Propulsion Society, 2022.

[70] M. Merino, D. García-Lahuerta, and E. Ahedo, "Plasma acceleration in a magnetic arch," *Plasma Sources Science and Technology*, vol. 32, no. 6, p. 065 005, Jun. 2023. DOI: 10.1088/1361-6595/acd476. [Online]. Available: https://dx.doi.org/10.1088/1361-6595/acd476.

[71] S. Di Fede, M. Manente, P. J. Comunian, and M. Magarotto, "Magnetic nozzle performance in a cluster of helicon plasma thrusters," *Plasma Sources Science and Technology*, vol. 32, no. 6, p. 065 013, 2023.

[72] M. Guaita, E. Ahedo, and M. Merino, "Pic/fluid simulations of the plasma expansion in a planar magnetic arch," *Plasma Sources Science and Technology*, vol. 34, no. 1, p. 015 007, Jan. 2025. DOI: 10.1088/1361-6595/adab8e.

[73] K. Vereen, A. Kimber, J. Correy, D. Olson, H. Martin, and R. Winglee, "Characterization of a cluster of high power helicon thrusters," in *AIAA Propulsion and Energy 2021 Forum*, ser. AIAA 2017-4628, 2017.

[74] K. Vereen *et al.*, "Recent advances in the clustering of high power helicon thrusters," in *AIAA Propulsion and Energy 2019 Forum*, ser. AIAA 2019-3902, 2019.

[75] D. M. Pozar, *Microwave engineering*. John wiley & sons, 2011.

[76] J. Navarro-Cavallé, M. Wijnen, P. Fajardo, and E. Ahedo, "Experimental characterization of a 1 kW helicon plasma thruster," *Vacuum*, vol. 149, pp. 69–73, 2018. DOI: 10.1016/j.vacuum.2017.11.036.

[77] F. Cichocki, J. Navarro-Cavallé, A. Modesti, and G. Ramírez Vázquez, "Magnetic nozzle and rpa simulations vs. experiments for a helicon plasma thruster plume," *Frontiers in Physics*, vol. 10, 2022. DOI: 10.3389/fphy.2022.876684.

[78] E. Ahedo and M. Merino, "Two-dimensional supersonic plasma acceleration in a magnetic nozzle," *Physics of Plasmas*, vol. 17, no. 7, p. 073 501, 2010. DOI: 10.1063/1.3442736.

[79] E. Ahedo, "Plasmas for space propulsion," *Plasma Physics and Controlled Fusion*, vol. 53, no. 12, p. 124 037, 2011. [Online]. Available: http://stacks.iop.org/0741-3335/53/i=12/a=124037.

[80] M. Merino and E. Ahedo, "Plasma detachment in a propulsive magnetic nozzle via ion demagnetization," *Plasma Sources Science and Technology*, vol. 23, no. 3, p. 032 001, 2014. DOI: 10.1088/0963-0252/23/3/032001.

[81] M. Merino and E. Ahedo, "Contactless steering of a plasma jet with a 3D magnetic nozzle," *Plasma Sources Science and Technology*, vol. 26, no. 9, p. 095 001, 2017. DOI: 10.1088/1361-6595/aa8061.

[82] C. Boyé, J. Navarro-Cavallé, and M. Merino-Martinez, "Preliminary analysis of the magnetic arch plasma expansion in a cluster of two ECR plasma thrusters," in *10th EUCASS Conference*, Lausanne, Switzerland, July 9–13, 2023.

[83] R. B. Lobbia and B. E. Beal, "Recommended practice for use of langmuir probes in electric propulsion testing," *Journal of Propulsion and Power*, vol. 33, no. 3, pp. 566–581, 2017. DOI: 10.2514/1.B35531.

[84] S. T. Lai and C. Miller, "Retarding potential analyzer: Principles, designs, and space applications," *AIP Advances*, vol. 10, no. 9, p. 095 324, 2020.

[85] S. Correyero, J. Jarrige, D. Packan, and E. Ahedo, "Plasma beam characterization along the magnetic nozzle of an ECR thruster," *Plasma Sources Science and Technology*, vol. 28, no. 9, p. 095 004, 2019. DOI: 10.1088/1361-6595/ab38e1.

[86] M. Merino and E. Ahedo, "Influence of electron and ion thermodynamics on the magnetic nozzle plasma expansion," in 33^{rd} *International Electric Propulsion Conference*, Electric Rocket Propulsion Society, 2013.

[87] E. Ahedo, S. Correyero, J. Navarro, and M. Merino, "Macroscopic and parametric study of a kinetic plasma expansion in a paraxial magnetic nozzle," *Plasma Sources Science and Technology*, vol. 29, no. 4, p. 045 017, 2020. DOI: 10.1088/1361-6595/ab7855.

[88] J. Little and E. Choueiri, "Electron cooling in a magnetically expanding plasma," *Physical Review Letters*, vol. 117, no. 22, p. 225 003, 2016.

[89] M. Merino, J. Nuez, and E. Ahedo, "Fluid-kinetic model of a propulsive magnetic nozzle," *Plasma Sources Science and Technology*, vol. 30, no. 11, p. 115 006, 2021. DOI: 10.1088/1361-6595/ac2a0b.

[90] A. Vinci, Q. Delavière-Delion, and S. Mazouffre, "Electron thermodynamics along magnetic nozzle lines in a helicon plasma," *Journal of Electric Propulsion*, vol. 1, no. 4, 2022.

[91] K. Takahashi, C. Charles, R. W. Boswell, and A. Ando, "Thermodynamic analogy for electrons interacting with a magnetic nozzle," *Physical review letters*, vol. 125, no. 16, p. 165 001, 2020.

[92] J. Y. Kim, K.-J. Chung, K. Takahashi, M. Merino, and E. Ahedo, "Kinetic electron cooling in magnetic nozzles: Experiments and modeling," *Plasma Sources Science and Technology*, vol. 32, no. 7, p. 073 001, 2023. DOI: 10.1088/1361-6595/acd71c.

[93] Á. Sánchez-Villar *et al.*, "Comparison of a hybrid model and experimental measurements for a dielectric-coated coaxial ECR thruster," *Plasma Sources Science and Technology*, vol. 32, no. 1, p. 014 002, 2023. DOI: 10.1088/1361-6595/acb00c.

[94] S. Mazouffre, "Laser-induced fluorescence diagnostics of the cross-field discharge of Hall thrusters," *Plasma Sources Science and Technology*, vol. 22, no. 1, p. 013 001, Nov. 2012. DOI: 10.1088/0963-0252/22/1/013001. [Online]. Available: https://doi.org/10.1088/0963-0252/22/1/013001.

[95] A. E. Vinci, M. R. Inchingolo, S. Mazouffre, and J. Navarro-Cavallé, "Ion dynamics in the magnetic nozzle of a waveguide ecr thruster via laser-induced fluorescence spectroscopy," *Journal of Physics D: Applied Physics*, vol. 56, no. 2, p. 025 204, 2022.

[96] A. Vinci, S. Mazouffre, M. R. Inchingolo, V. Gómez, P. Fajardo, and J. Navarro-Cavallé, "Probing xenon atoms and ions velocity in the magnetic nozzle of a helicon plasma thruster," in *37th International Electric Propulsion Conference*, 2022.

[97] A. E. Vinci, "Physics of magnetic nozzles and helicon plasma discharges," Ph.D. dissertation, Université d'Orléans, 2022.

[98] A. E. Vinci, S. Mazouffre, V. Gómez, P. Fajardo, and J. Navarro-Cavallé, "Laser-induced fluorescence spectroscopy on xenon atoms and ions in the magnetic nozzle of a helicon plasma thruster," *Plasma Sources Science and Technology*, vol. 31, no. 9, p. 095 007, 2022.

[99] D. Gawron, S. Mazouffre, and C. Boniface, "A fabry–pérot spectroscopy study on ion flow features in a Hall effect thruster," *Plasma Sources Science and Technology*, vol. 15, p. 757, 2006.

[100] R. Cedolin, W. Hargus, P. Storm, R. Hanson, and M. Cappelli, "Laser-induced fluorescence study of a xenon hall thruster," *Applied Physics B*, vol. 65, pp. 459–469, 1997.